2-27-2018 2:40 PM

Experimental and Numerical Investigation of Emulative Connections in Precast Concrete Walls

Mohamed Gamal Elsayed
The University of Western Ontario

Supervisor
Nehdi, Moncef L.
The University of Western Ontario

Graduate Program in Civil and Environmental Engineering
A thesis submitted in partial fulfillment of the requirements for the degree in Doctor of Philosophy
© Mohamed Gamal Elsayed 2018

Follow this and additional works at: https://ir.lib.uwo.ca/etd

Part of the Civil Engineering Commons, and the Structural Engineering Commons

Abstract

Grouted connections are widely used in the precast concrete construction. For instance, in precast concrete walls, they are used to connect assemblies of vertically stacked panels. The connection is comprised of a grout cylinder bound by a corrugated metallic duct, which is used to house a large diameter reinforcing bar bridging the horizontal gap of stacked panels. The connection is used to provide vertical continuity to the assembly, and to help resist tensile demands from in-plane bending. Current design guidelines consider such connections through a bar-in-concrete treatment, disregarding its composite nature and the confinement effect of the duct. This has resulted in excessively long connections that could induce planes of reduced stiffness in precast wall panels.

In this thesis, a research program was tailored to investigate the disparity between the real behaviour of grouted connections and their current design code idealization to offer alternative more realistic design provisions. The experimental program was divided into three phases. First, an exploratory study of the bond behaviour of grouted connections under monotonic loads was conducted. Second, the behaviour of grouted connections was compared to bar-in-concrete specimens under monotonic loading. Third, the cyclic behaviour of the connections at various embedment lengths was examined under quasi-static loading. Knowledge gained in the experimental program was used in analytical treatments to develop a novel model that can accurately depict the behaviour of these connections.

Results from the various experimental phases reveal that the bond failures developed in grouted connections are not characterized by brittle tensile splitting modes, irrespective of the level of bond stress along the assembly at different embedded lengths. It was observed that the presence of the corrugated duct offers a continuous restraining field against radial expansion of the grout, causing the bars to be mobilized in much shorter anchored lengths than those suggested by current standards. A numerical model was developed to reproduce the behaviour of grouted connections with reasonable accuracy. Its accuracy and computational efficiency should allow modelling full-scale precast wall assemblies.

Keywords

Co-Authorship Statement

This thesis was prepared per the integrated-article layout designated by the Faculty of Graduate Studies at Western University, London, Ontario, Canada. All the work stated in this thesis including experimental testing, data analysis, numerical modelling, and writing draft manuscripts for publication was carried out by the candidate under the supervision and guidance of Dr. Moncef L. Nehdi. Any other co-author (if applicable) assisted in conducting the experimental program and/or revision of the initial draft of the manuscript. The following publications have been either accepted or submitted to peer-reviewed technical journals and conference proceedings:

1. **M. Elsayed,** M.L. Nehdi, "Experimental and Analytical Study on Grouted Duct Connections in Precast Concrete Construction" *Materials and Structures*. 2017, 50, 198.

2. **M. Elsayed,** M.L. Nehdi, D.J. Provost-Smith and O. Eissa, "Exploratory Investigation of Grouted Bar-In-Duct Connections under Direct Tensile Load" *Construction and Building Materials,* In review, Jul 2017.

3. **M. Elsayed**, F. Ghrib and M.L. Nehdi, "Experimental and Analytical Study on Grouted Dowel Connections under Quasi-Static Loading" *Construction and Building Materials,* In Press, Dec 2017.

4. **M. Elsayed**, F. Ghrib and M.L. Nehdi, "Finite Element Model of Grouted Connections Using Interfacial Cohesive Elements", *Computers and Structures,* Submitted, Jan 2018.

5. **M. Elsayed,** M.L. Nehdi, D.J. Provost-Smith and O. Eissa "Bond Behaviour of Grouted Connections Under Monotonic Tensile Loads", *Resilient Infrastructure, Proceedings of the 5th International Conference of the Canadian Society for Civil Engineering, London, ON, Canada, 1-4 June 2016.*

Dedication

To: *My Father: Gamal Mohamed Elsayed*

My Mother: Asmaa Abdel Azim

My Siblings: Dina and Amira

My Wife: Eman El Shazly

My Children: Moussa, Maria and Lina

My Mother and Father in-law: Hoda Fahmy & Fathy El Shazly

Acknowledgments

Foremost, I express my deepest thanks and acknowledgments to Allah the most merciful, most gracious, who has given me the strength and tenacity to complete this work and inspired me to persevere through it. May this effort please him and grant me his guidance and mercy.

My deepest thanks and appreciation go out to all the people who supported me during my journey. I cannot fully capture the extent of my gratitude towards many of you. To all of you I owe an incalculable debt.

It goes without saying that I devote the next few lines for thanking my advisor Dr. Moncef L. Nehdi for his support and guidance. But I wish to make a clear distinction here; no matter how hard I try, I can never fully thank him enough for what he did to me. Dr. Nehdi was more than a phenomenal advisor and an excellent teacher. He was a good friend and an avid listener. He believed in me and encouraged me every time I met with him. He taught me a life lesson in wisdom and humility, for which I am very grateful.

I would like to thank my family for their continued prayers and support during my journey, especially my beloved wife, Eman, not only for her love and encouragement during my darkest moments, but also for working hard to support our little family financially. I would like to acknowledge my mother, Asmaa, my father, Gamal, and my sisters, Dina and Amira, whom used to pray for me whenever I was stuck. Also, my mother in law, Hoda, for spending an entire three years of her life watching my kids while I was away, and my father in law, Fathy, who was infallible in supporting her presence with us.

I also would like to thank people who have significantly contributed to this work. Dr. Osama Eissa, who is more than just a mentor and a close friend, who has attended to 100% of my calls for help. I wish to thank Doug Provost-Smith for helping me in the lab and for countless discussions and debates about bond research. I am grateful to the now retired laboratory supervisor, Wilbert Logan, for tremendously helping me during my experimental work. I acknowledge Dr. Faouzi Ghrib for his contributions to the last two chapters of this work, and the University of Windsor's laboratory technologist, Matt St. Louis, who is one of the smartest

TABLE OF CONTENTS

LIST OF TABLES

LIST OF FIGURES

LIST OF SYMBOLS

f_c' Concrete/grout compressive strength (MPa)

R_r Relative rib area of bar

d_b Diameter-of-bar (mm)

τ Bond Stress (MPa)

σ_s Bar stress (MPa)

μ_s Perimeter of the bar (mm)

l_{tr} Embedded length (mm or d_b)

$\bar{\tau}$ Average bond stresses (MPa)

T Pulling force (kN)

L_d Development length (mm or d_b)

f_y Steel yield strength (MPa)

ψ_l Reinforcement location factor

ψ_e Reinforcement coating factor

ψ_s Reinforcement size factor

c_b Cover dimension (mm)

k_{tr} Transverse reinforcement index (mm)

U_{av} Average bond stress (MPa)

d	Nominal diameter of the bar (mm)
F	Tensile load (kN)
$U_{av\ max}$	Peak average bond stress (MPa)
F_{max}	Peak tensile load (kN)
ϵ_{max}	Peak strain in bar
ϵ	Strain in bar
f_{max}	Peak bar stress (MPa)
SF_{maxU}	Free end slip corresponding to peak average bond stress (mm)
SL_{maxU}	Loaded end slip corresponding to peak average bond stress (mm)
ϵ_{maxU}	Strain corresponding to peak average bond stress
U_{res}	Residual bond stress (MPa)
U_{maxBPE}	Peak bond stress from BPE model (MPa)
α	BPE model fitting parameter
P	mBPE model fitting parameter
E	Elastic modulus of bar (MPa)
s	Slip of bar (mm)
τ_{max}	Maximum bond stress (MPa)
s_{max}	Slip corresponding to maximum bond stress (mm)
s_1	Slip at onset of maximum bond stress plateau (mm)
s_2	Slip at outset of maximum bond stress plateau (mm)

s_3	Slip corresponding to residual bond stress (mm)
A_τ	Area under ascending branch of bond stress vs slip (J.m^{-3})
d_{duct}	Diameter of duct (mm)
β	Modification factor for duct material
$f_{s,cr}$	Critical level of stress in reinforcement (MPa)
$f_{cg}{}'$	Grout compressive strength (MPa)
γ	Modification factor to account for group effect
D_{max}	Displacement at the loaded end (mm)
ks	Kolmogorov-Smirnov statistic
γ_s	Modification factor to account for bar stress variations
ϕ	Safety factor to account for variation in materials taken as 1.2
R_d	Ductility ratio
ε_{ult}	Coupon strain at failure
f_{bond}	Bond stress of frictional model (MPa)
μ	Coefficient of friction
f_{con}	Confinement stress (MPa)
$f_{adhesion}$	Adhesion stresses (MPa)
f_{sleeve}	Confinement effect of the duct (MPa)
$f_{stirrup}$	Confinement effect of the stirrup (MPa)
f_{cover}	Confinement effect of concrete strength (MPa)

t_s	Duct thickness (mm)
E_s	Duct modulus of elasticity (MPa)
ε_s	Duct hoop strain
A_{st}	Cross-sectional area of the stirrups (mm^2)
f_{st}	Yield stress of the stirrups (MPa)
s	Stirrup spacing (mm)
$f_{t'}$	Concrete/grout tensile strength (MPa)
c	Cover thickness (mm)
s_a	Slip at onset of maximum bond stress (mm)
s_b	Slip at outset of maximum bond stress (mm)
s_r	Slip corresponding to the rigid body displacement of one rib (mm)
τ_f	Frictional component of bond stress (MPa)
$\tau_2{}^*$	Modified bond stress in the tangential direction (MPa)
τ_2	Bond stress in the tangential direction 2 (MPa)
s_2	Slip in the tangential direction 2 (mm)
m_n	Modifier to account for concrete splitting
m_s	Modifier to account for strain penetrations
$\tau_2{}^*$	Effective bond stress (MPa)
ε_s	Strain in bar
ε_y	Yield strain

ε_u	Ultimate strain
σ_1	Normal stress (MPa)
s_1	Slip due to normal stress (mm)
k_1	Penalty stiffness factor in the normal direction 1
k_3	Penalty stiffness factor in the tangential direction 3
s_3	Slip due to tangential stress 3 (mm)
τ_3	Bond stress in the tangential direction 3 (MPa)
σ_c	Compressive stress of concrete (MPa)
σ_c	Compressive stress of concrete (MPa)
ε_{co}	Compressive strain at the onset of hardening
w_c	Crack width (mm)
w_l	Crack opening at the partial release of stress (mm)
w_c	Crack opening at the complete release of stress (mm)
G_F	Fracture toughness (J.m^{-3})
α_0	Aggregate surface parameter
d_a	Nominal maximum aggregate size (mm)
$\dfrac{w}{c}$	Water to cement ratio
λ	Dimensionless separation parameter
δ_{II}^F and δ_I^F	Peak separation in tangential and normal directions, respectively (mm)
G_{II}^c and G_I^c	Fracture toughness in tangential and normal directions, respectively (J.m^{-3})

$A^{°}$ Area under normalized bond-slip law

S and T Peak traction in tangential and normal directions, respectively (MPa)

V Validation metric

λ Dimensionless separation parameter

Chapter 1

1   INTRODUCTION

This chapter provides introductory information to the dissertation as follows: i) General; ii) Problem Statement; iii) Research Significance; iv) Specific Research Objectives; and v) Thesis outline.

1.1   GENERAL

Precast concrete construction is on its way to become a preferred method of construction, owing to its cost effectiveness, superior production plant quality control, and speed of installation. Its design flexibility, structural efficiency, and aesthetics are amongst the reasons for its growing popularity. According to recently published statistics, precast concrete annual sales increased by 6.5% between 2013 and 2018 (The Freedonia Group 2015). In fully precast buildings, precast concrete bearing and shear walls are often used conjointly with hollow core slabs. Total precast buildings enjoy the benefits of fast-paced erection schemes, with the quality and superiority of shop-manufactured concrete products. To ensure its economic advantage, precast concrete walls are dissected into smaller more manageable elements that are easier to transport, lift and erect. These elements are then connected together in the field using a variety of connections and hardware. Due to this modular nature, the behaviour of such wall assemblies is largely dependent on the behaviour of their connections or ties.

Precast concrete wall systems are designed to emulate cast-in-situ concrete structures. Since cast-in-situ walls are continuous, they resist lateral loads as a single unit. Conversely, precast wall construction consists of panels connected with horizontal and vertical joints. According to Fintel (1995), damage is highly concentrated in the joint regions, where planes of reduced stiffness can be induced, creating discontinuities in the structural framework of large panel precast construction. Thus, to achieve comparable performance

to that of conventional reinforced concrete, continuity across all joints is required. In horizontal joints, this is achieved by the placement of a vertical reinforcement bar.

One of the most commonly used ties in precast wall construction is a grouted reinforcing bar connection, or simply a grouted connection. The connection has an array of applications in connecting various precast elements, primarily due to its ease of application, low cost, and forgiving tolerances. Grouted connections are comprised of a large diameter reinforcing bar grouted and bound by a corrugated metallic duct, typically embedded in one of the connected members as illustrated in **Figure 1.1**. In the context of a typical precast wall assembly, two vertical wall panels are connected by a grouted connection, bridging the horizontal joint between the vertically stacked panels, as pictorially shown in **Figure 1.2**.
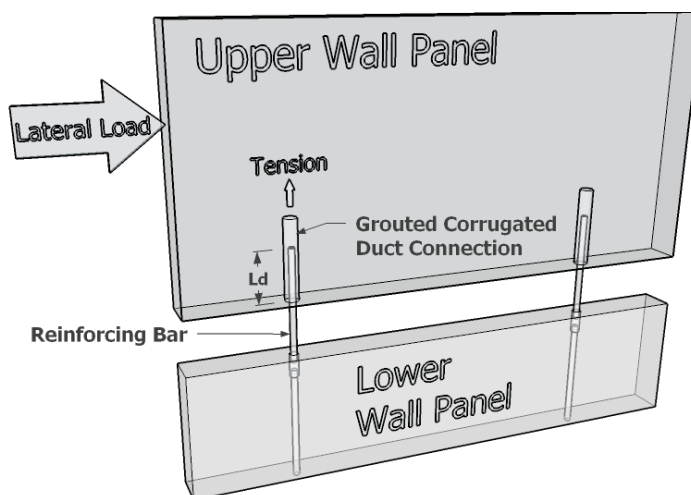
Figure 1.1: Schematic of grouted connections used to connect two walls.

The main function of the connections is to resist tension induced by in-plane and out-of-plane straining actions. The connection also provides the assembly with the necessary ductility in case of excessive deformations. Once the reinforcing bar yields, its post-yield deformation provides such ductility, which is in the form of a horizontal gap opening between two vertically stacked panels (Smith et al. 2013; Smith & Kurama 2014; Soudki et al. 1995; Kang et al. 2013; Priestley et al. 1999). Thus, the ductility of the assembly is limited to the yield strength of the connection bar and its plastic strain capacity.
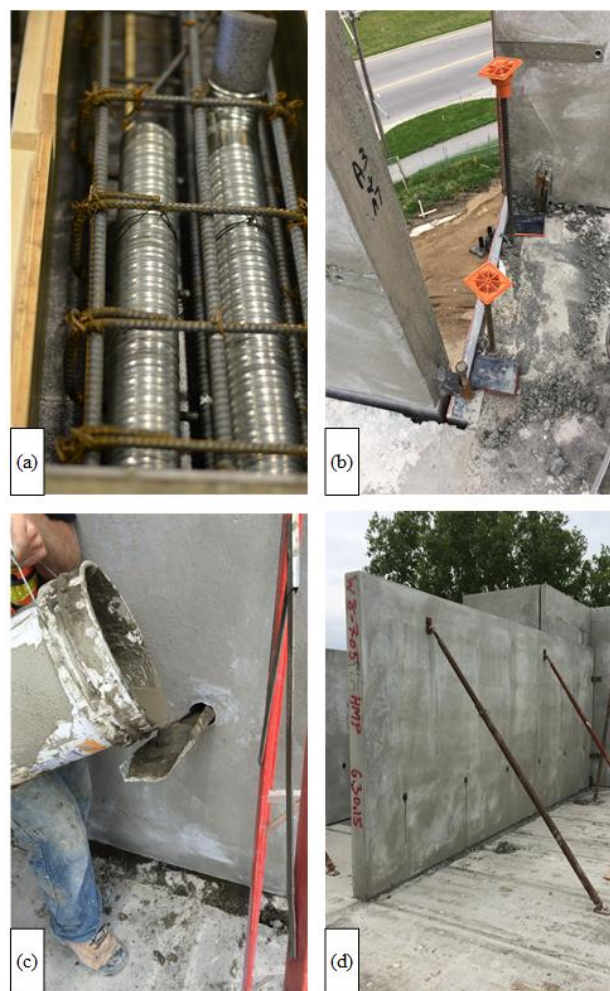
Figure 1.2: Field application of grouted connections: (a) pre-placement of ducts; (b) bar extension from lower panel; (c) field grouting; and (d) wall shoring.

1.2　PROBLEM STATEMENT

Under current design code recommendations, grouted connections are treated similar to a bar-in-concrete idealization, disregarding the composite nature of the corrugated duct. Only scant studies were devoted to understanding the bond behaviour of grouted connections. In the absence of a comprehensive understanding of the behaviour of these connections, designers and manufacturers tend to over-design these connections. Research has shown that increased grouted lengths make precast panels weaker since the effective wall cross-section is reduced due to the presence of the duct (Seifi et al. 2015). Additionally, this This results in excess material and labour expenditures. While limited

previous research (listed in Chapter 2) has pointed out that the bond developed by grouted connections behaved differently from the code idealization under monotonic loads, most of this research was done on grouted connections used in bridge bent-cap systems with different dimensions. Due to the sensitivity of bond, the results from these studies cannot be used to extrapolate the behaviour of grouted connections used in precast walls. Information on the behaviour of grouted connections under cyclic loads was not found in the literature. Moreover, most of these studies provided only qualitative information on some aspects of the connections, such as the confinement effect of the duct.

1.3   RESEARCH SIGNIFICANCE

In light of the above, this thesis strives to create much needed information on the behaviour of grouted connections. Structural aspects of such connections, including stiffness, bond strength, failure modes and ductility, need to be explored to identify possible limit states of failure. This has been undertaken in this thesis via a comprehensive series of experimental and numerical tests. The experimental phase should provide quantitative and qualitative information, including testing various connection schemes under monotonic and quasi-static cyclic loading scenarios. The thesis should also propose alternative design equations to calculate the development length of grouted connections based on specimens reflective of field conditions. Finally, this study also proposes a novel finite element modelling approach to simulate the behaviour of grouted connections.

1.4   SPECIFIC RESEARCH OBJECTIVES

This thesis provides the necessary information on the behaviour and design of grouted connections used in precast walls. As such, the specific objectives of this research are:

1) Investigate the bond behaviour of grouted connections under monotonic loads.

2) Examine the bond performance of grouted connections utilizing various bars to explore their potential to replace conventional steel reinforcement.

3) Provide quantitative and qualitative experimental and analytical evidence on the difference between grouted connections and the commonly used bar-in-concrete idealization.

4) Explore the behaviour of grouted connections under quasi-static cyclic loading.

5) Propose new empirical expressions to design the development length of grouted connections deduced from the tested limit states of the connection.

6) Examine the effect of changing the embedment length on the behaviour of grouted connections.

7) Deduce and calibrate bond-slip models reflecting the nature of grouted connections, to be used in numerical applications.

8) Develop a novel, computationally efficient, finite element model that can accurately reproduce the behaviour of grouted connections.

1.5   THESIS OUTLINE

This research thesis was organized into seven chapters as per the requirements of the integrated-article format predefined by the Faculty of Graduate Studies at Western University. Aside from the current Chapter (Introduction), the remainder of the dissertation is organized as follows:

Chapter 2: presents an overview of the relevant schemes of grouted connections. It also provides information on the experimental and analytical literature pertaining to grouted connections.

Chapter 3: discusses the experimental and analytical findings of a study undertaken in this thesis to highlight the disparities between the behaviour of grouted connections and that of bar-in-concrete specimens. The data was used to arrive at an empirical design equation that can be used to predict the bar stress at a given embedment length.

Chapter 4: examines the bond behaviour of grouted connections under monotonic loads with changing various parameters known to influence the bond. The study included the response of FRP bars to examine their potential use in architectural non-load bearing panels.

Chapter 5: provides experimental information on the behaviour of grouted connections subjected to quasi-static cyclic loading under realistic field conditions. The study provides unique information on the behaviour of such connections as well as measuring the confinement effect of the duct. The results were used to update the design expression proposed in Chapter 3 to reflect the damage incurred by connections due to cyclic loading.

Chapter 6: presents a numerical implementation of the various bond-slip models deduced from the experimental work into a Finite Element (FE) framework. The model used a novel modelling approach to reduce the geometric non-linearity of the anchorage, which enabled a computationally efficient simulation.

Chapter 7: summarizes the results of this research, draws conclusions, and identifies future research needs.

1.6   CONTRIBUTIONS TO STATE-OF-ART

This dissertation scrutinizes aspects of the bond behaviour of grouted connections that were not so far duly explored in the open literature. The thesis delivers several novelties and contributions to the state-of-the-art. First, it provides the scientific community and industry practitioners with the necessary information on the behaviour of grouted connections and proposes alternative more realistic related design equations. Second, it examines the underlying design premises, which were originally proposed by relevant design codes, and provides critical analysis of the behaviour of the connections versus the bar-in-concrete design code idealization. Third, it examines closely and for the first time, information on the behaviour of the connections under cyclic loads, utilizing a novel specimen form that eliminates the spurious parameters associated with bond testing. Finally, it proposes a novel numerical method to model grouted connections using interfacial cohesive elements.

The proposed model is computationally very efficient and can be used to model complete assemblies. It is expected that these novel contributions to the state-of-the-art will have transformative effects on design provisions of emulative connections in the precast concrete construction around the world.

1.7 REFERENCES

ACI Committee 318, 2014. Building Code Requirements for Structural Concrete and Commentary. *American Concrete Institute, Farmington Hills, MI, USA*, pp.1–519.

Fintel, M., 1995. Performance of buildings with shear walls in earthquakes of the last thirty years. *PCI Journal*, 40(3), pp.62–80.

Kang, S.-M., Kim, O.-J. & Park, H.-G., 2013. Cyclic loading test for emulative precast concrete walls with partially reduced rebar section. *Engineering Structures*, 56, pp.1645–1657.

PCI, 2010. PCI Design Handbook 7th Edition. *Precast Concrete Institute, Chicago, IL*, (October), pp.1–828.

Priestley, M.J.N. et al., 1999. Preliminary results and conclusions from the PRESSS five-story pre-cast concrete test building. *PCI Journal*, 44(6), pp.42–67.

Seifi, P., Henry, R.S. & Ingham, J., 2015. Preliminary test results of precast concrete panels with grouted connections. In *New Zealand Society for Earthquake Engineering Technical Conference*. Rotorua, New Zealand, pp. 744–751.

Smith, B.J. et al., 2013. Behavior of Precast Concrete Shear Walls for Seismic Regions : Comparison of Hybrid and Emulative Specimens. *ASCE Journal of Strucutral Engineering*, 139(11), pp.1917–1927.

Smith, B.J. & Kurama, Y.C., 2014. Seismic design guidelines for solid and perforated precast concrete shear walls. *PCI Journal*, 59(3), pp.43–59.

Soudki, K., Rizkalla, S. & LeBlanc, B., 1995. Horizontal connections for precast concrete

shear walls subjected to cyclic deformations. Part 1: mild steel connections. *PCI Journal*, 40(4), pp.78–97.

The Freedonia Group, 2015. Precast concrete products. *Market Research Report*, pp.1–329.

Chapter 2

2 BACKGROUND AND RESEARCH CONTEXT

This chapter presents background information on grouted connections used in precast concrete construction. First, it discusses introductory information on the connections and the related bond mechanics. Then it highlights the most relevant experimental and analytical efforts available in the open literature.

2.1 GENERAL

2.1.1 Precast Walls

Precast concrete shear walls are vertical, cantilever like, structural elements used to transfer lateral forces from the super-structure to the foundation of precast buildings. They can be a part of or the sole component of a building's Lateral Force Resisting System (LFRS). They are usually oriented in both principal axes of the building to resist lateral forces in both directions. To increase their resistance to overturning and uplifting, it is desirable to design shear walls as load bearing elements to increase their resistance against over-turning and to reduce rocking of the panels in-case of excessive deformations. ACI 318-14 Section 18.2.1.6, defines the different types of shear walls as follows: Ordinary structural walls: walls with no special detailing related to seismic loads; Intermediate precast concrete structural walls: Section 18.5.2.2 of the same standard, necessitates yielding of steel in the connections of the walls, the non-yielding components of the connections must provide a strength 50% greater than that of the yielding elements; Special precast concrete structural walls: walls designed and detailed to emulate cast-in-place concrete shear walls, in addition to satisfying requirements of Section 18.5.2.2 pertaining to the connections (ACI Committee 318 2014).

The concept of "Capacity Design" is a design philosophy that allows a building to undergo failure at specific elements (where special seismic considerations and detailing are

provided), while the rest of the elements are designed to deform in the elastic range. This should be achieved without any loss of structural integrity that would result in catastrophic failure. Due to the dissected nature of precast concrete construction, the capacity design concept is taken into consideration in two stages: the design of the element itself; and more importantly in the design of the connection between the elements. Thus, ductility of precast concrete construction is largely induced and/or influenced by the design and detailing of the connections. The selection of the assembly is largely influenced by the experience and judgement of the designer, but also takes into consideration important aspects such as constructability and cost.

2.1.2   Precast Wall Connections

Under current industry practice pertaining to precast concrete construction, precast walls can be connected either by jointed or emulative connections. Jointed connections, typically consisting of bolted or welded plates, are those exhibiting different stiffness than that of the walls they are connecting. Due to this difference in stiffness, the assemblies show a behaviour that differs from cast-in-situ concrete. Apart from their laborious installations, the use of jointed connections in precast shear walls is conditional on experimental evidence and analysis to prove that they have strength and toughness equivalent to that of cast-in-place reinforced concrete.

Alternatively, emulative connections are defined as those connections allowing a precast concrete structure to have an equivalent behaviour to that of a monolithic structure (ACI Committee 550 2001). Emulative connections typically consist of grout and vertical/ horizontal continuity reinforcement. While this can be achieved by a variety of schemes depending on the designer and the fabricator, two main schemes are primarily used: Grouted connections; and grouted splice sleeves. Although both connection types are emulative, grouted splice sleeves are generally not preferred due to their high cost and unforgiving tolerances. A typical wall detail showing both schemes is displayed in **Figure 2.1**. As can be observed from this figure, both connections significantly depend on bond, the main mechanism through which emulative connections achieve their monolithic-like behaviour.
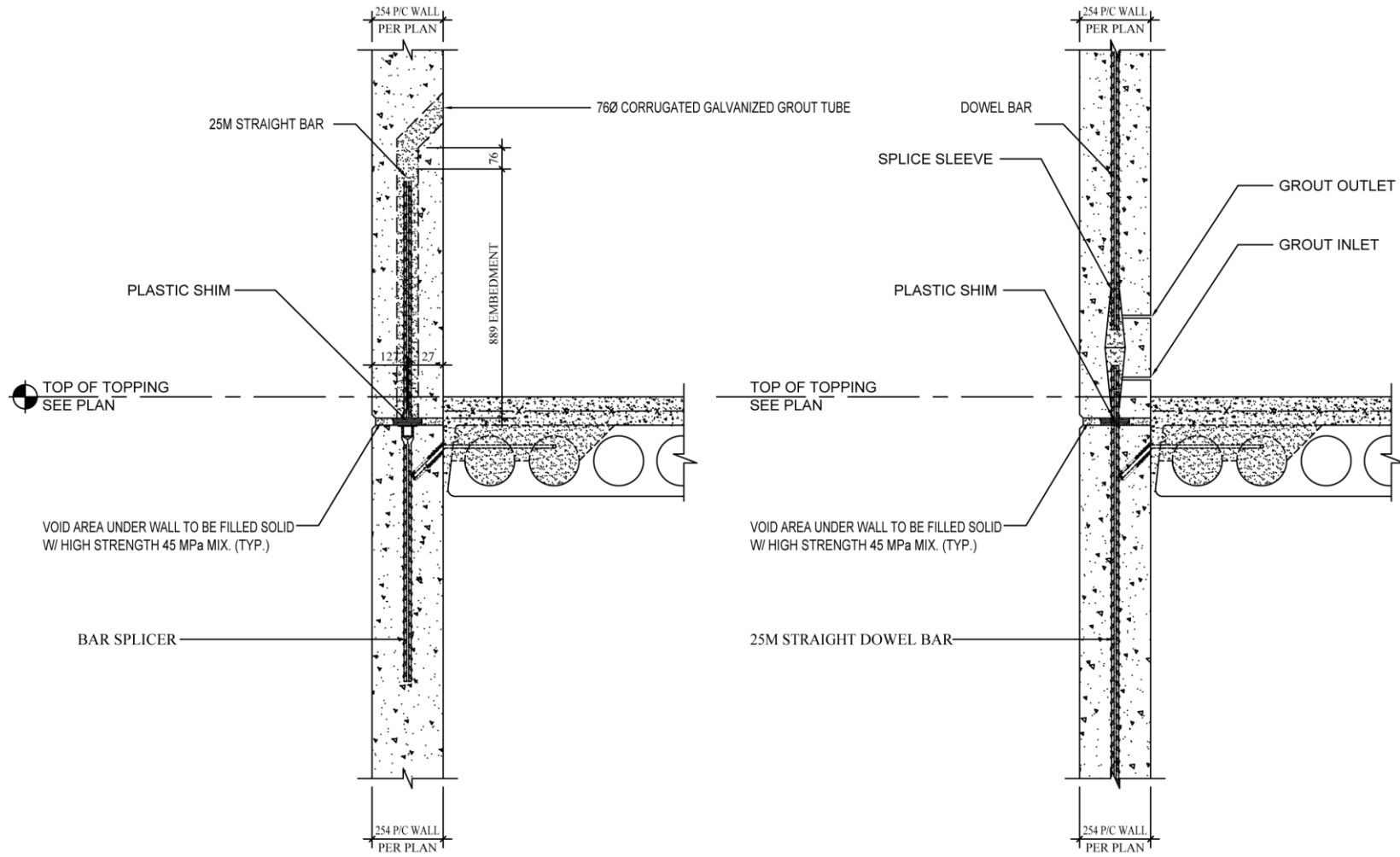
Figure 2.1: [Left to Right] Grouted connections; grouted splice sleeve (courtesy of IES Associates, Windsor, ON).

The concept of emulative connections in precast construction was not used until the early 1990's. It is not clear when or by whom exactly the term was coined, but the studies by Restrepo et al. (1993) and Park (1995) are amongst the earliest references. In the latter, precast buildings were framed using precast beams and columns, where the longitudinal columns passed through voids in the beams and protruded above them. The voids were formed using corrugated ducts. Prior tests undertaken on the components level by Restrepo et al. (1993) showed that the connections exhibited excellent stiffness and ductility. Conclusions from both studies confirmed that the behaviour of such connections is comparable to their monolithic counterpart. Since emulative connections rely on bond to achieve their composite behaviour, it is expedient to provide a review of bond from research and relevant design codes so as to fully understand the behaviour of grouted connections.

2.2 BOND

2.2.1 Bond Mechanics

Bond between deformed steel bars and concrete is a topic that has been extensively investigated in the open literature. This review is not meant to be exhaustive, but merely intends to provide relevant fundamental knowledge that would facilitate the understanding of the behaviour of grouted connections.
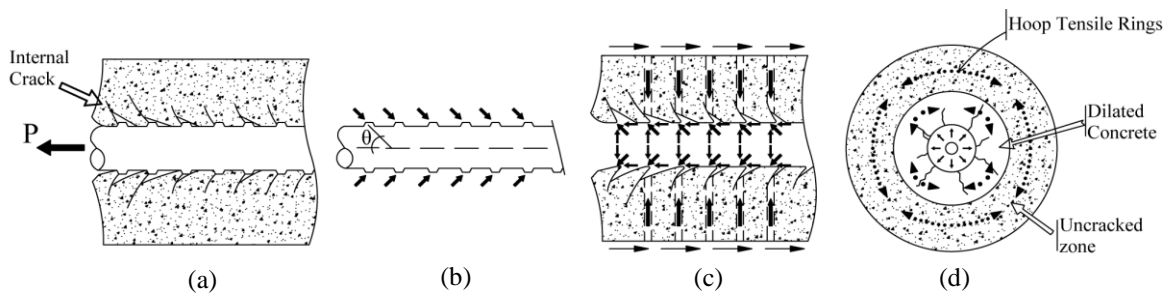
Figure 2.2: [a] Internally cracked zone around a pulled bar; [b] bar forces; [c] forces at the bar-concrete interface; and [d] splitting failure.

In its most basic definition, bond between steel reinforcement and concrete refers to the interaction that allows the transfer of tensile stresses in an assembly. **Figure 2.2** shows the state of stress and forces developed at the interface of an assembly. When a bar embedded in concrete is pulled, the developed resultant forces are inclined by an angle θ with respect to the longitudinal axis of the bar, as shown in **Figure 2.2(b)**. The value of θ is greatly debated in the open literature, but is believed to be roughly proportional to the angle of the face rib of the bar. When the resultant force (**Figure 2.2(c)**) is decomposed into parallel and normal components. The parallel component contributes to bond stresses, while normal components contribute to splitting stresses. Bond is generated through three main mechanisms: chemical adhesion; mechanical bearing; and friction. Chemical adhesion only contributes a small portion of the bond stresses (typically ~1-2 MPa) and disappears with the onset of slip of the bar. Frictional bond components depend on the surface characteristics of the assembly and do not engage until the bar experiences slip. Hence, the bond of deformed bars embedded in steel is primarily dependent on mechanical bearing.

Bond is sensitive to several influential parameters. ACI committees 408R-03 (Bond and Development of Straight Reinforcing Bars in Tension) and 408.2R-12 (Bond under Cyclic Tests), outlines more than seventeen factors that affect the bond of anchored bars, chief among which are:

1- Compressive strength

Most descriptive and design expressions are based on the assumption that the bond strength is proportional to $\sqrt{f_c'}$. Earlier research has shown that, for normal strength concrete (< 70 MPa), the tensile and shear strengths (contributing factors in resisting the parallel and radial components discussed above) to be closely approximated by $\sqrt{f_c'}$ (ACI Committee 408.2R 2012). Later studies have contested this assumption, citing that bond strength increases with an increase in compressive strength. For compressive strengths ranging between 50-80 MPa, bond is proportional to $f_c'^{\frac{3}{4}}$ (Zuo & Darwin 1998).

2- Bar properties

Bar size: larger bars develop lower bond stresses than that of smaller bars for the same embedment length (Orangun et al. 1977; Darwin & Zavaregh 1996);

Bar geometry: the relative rib area R_r, defined as the ratio of bearing area divided by shearing area, has a direct effect on the bond stresses developed. Doubling the R_r could reduce the development length and splice lengths of anchorage by 20% (Cairns & Jones 1996);

Steel stress level: under the same conditions, a bar with a lower yield strength develops lower bond stresses than that of a higher strength bar when no confinement is present, and slightly higher bond stresses when transverse reinforcement is provided (Zuo & Darwin 2000; Zuo & Darwin 1998);

Surface condition: smooth or epoxy coated bars develop lower bond stresses than that of their non-coated and ribbed coutnerparts (Treece & Jirsa 1989);

Steel strain level: increasing the axial strain of the bar beyond yielding reduces the bond stress and invokes additional slip. When the bar starts to soften, the lugs disengage due to the reduction in cross-sectional area resulting from the Poisson effect (Raynor 2000).

3- Embedment length:

Generally, an increase in the bonded length of the anchorage will be accompanied by a decrease in bond stress and increase in bond capacity. It should be noted that there are no conclusive data in the open literature regarding the relationship between bonded length and developed bond stress (ACI Committee 408.2R 2012).

2.2.2   Confinement and Failure Mechanisms

Increasing the confinement of an anchored bar significantly influences the level of bond stress developed and the failure mode of the anchorage. Confinement can help superimpose compressive stresses unto the tensile rings developed, as highlighted in **Figure 2.2(c)**. This

influences the failure mechanism of the anchorage depending on the face angle of inclination and the frequency and magnitude of the compressive struts. Confinement can be classified depending on whether the compressive field is due to an action or a reaction force. Example of an active confinement field is due to an applied external load or a result of pre-stressing. Passive confinement is one which develops in the steel surrounding the anchorage because of pulling. This includes transverse reinforcement in the form of spirals or stirrups, or simply the concrete cover, as shown in **Figure 2.2(d).** Passive and active confinement actions impart different mechanisms. Active confinement acts before the loading begins and works by suppressing splitting before it starts. Conversely, passive confinement only engages after the concrete rings in the vicinity of the bar crack and the hoop tensile capacity is exhausted. It works by restricting and delaying the growth and progression of such cracks. In general, the efficiency for inhibiting the growth of splitting cracks is increased as the confinement field is closer to the bar.

Eligehausen et al. (1982) conducted pull-out tests on concrete specimens embedded at 5 diameters-of-bar (d_b). A variety of parameters were explored in fundamental study on bond of deformed bars in concrete, including the magnitude of the compressive field applied unto the specimens. This was reflected in the specimens by changing the transverse reinforcement of the different specimens and measuring their response. The effect of changing the transverse reinforcement details on the bond stress vs slip response is shown in **Figure 2.3**. It can be observed that there is an increase in bond stress as transverse pressure increased. However, they pointed out that there is a point of diminishing returns, where the transverse pressure is no longer proportional to the increase in bond resistance.
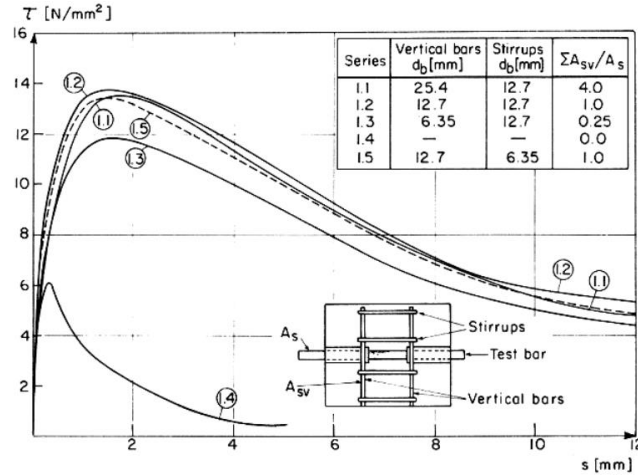
Figure 2.3: Influence of confinement on the bond stress vs slip relationship by Eligehausen et al. (1982) (reproduced with permission).

Others have made similar observations prior to the study conducted by Eligehausen et al. (1982). For example, Tepfers (1973) compared stirrups and spiral in a series of lapped splice beam specimens. Results have shown an increase in bond stress with the increase of the diameter of the stirrups and spiral. The influence of an applied normal compressive pressure on the bond resistance of bars embedded in concrete blocks was studied by Untrauer & Henry (1965). Applied lateral pressure ranged from 0 to 20 MPa (corresponding to 0 to $0.5f_c'$). Results indicate proportional increase in bond strength as the pressure increased, which was attributed to an increase in frictional characteristics of the specimens and restricting the tensile failure modes.
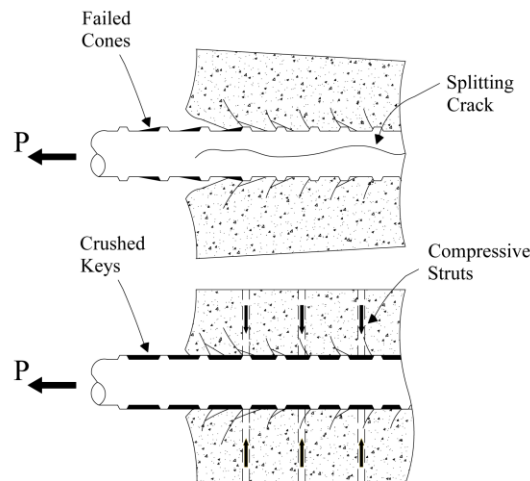
Figure 2.4: [Top to Bottom] Bond splitting and pull-out failures, respectively.

When a steel bar is pulled out from a surrounding cementitious medium, slippage of the bar occurs because of the wedging action of the bar (splitting dominated), or through progressive crushing of the shear keys between successive ribs (pull-out dominated), as shown in **Figure 2.4**. It is also possible for a mixed mode failure to occur in moderately confined anchorages. When no restriction against the expansion of the concrete is offered, splitting failures occur, which depends primarily on the force exerted on the concrete and not on the bar stress or embedded area. Because of this independency, tensile splitting failures are not accepted in the design of anchorages, especially those designed to yield. It is the intent of the design code to reduce the bond stress sufficiently, such that these failures do not manifest (ACI Committee 408 2003). If, on the other hand, sufficient confinement is provided, failure occurs by shearing of the concrete keys between successive lugs of the bar, as shown in **Figure 2.4**. Such failures are dependent primarily on the load per unit length of the bar, thus, showing a proportionality to the bar perimeter (Lutz & Gergely 1967).

2.2.3   Bond Tests

Local bond stress of an embedded bar in an anchorage is described as a characteristic of the assembly. As mentioned before in preceding sections, bond stress does not depend on the embedment length, as it is proportional to a radical of f'_c. It is relevant to highlight here, that amongst the factors the affect the bond, the method of testing poses an exogenous important factor. It influences the nature of the response and failure. Various methods and techniques are reported in the literature on bond, some of which are illustrated in **Figure 2.5**. Out of the schemes shown, pull-out testing is one of the most widely used due to its ease of application. However, this methodology is known to be prone to spurious effects, that are considered favourable conditions of testing bond, particularly the compressive stresses induced at the boundary conditions associated, as shown in **Figure 2.6(b)**.
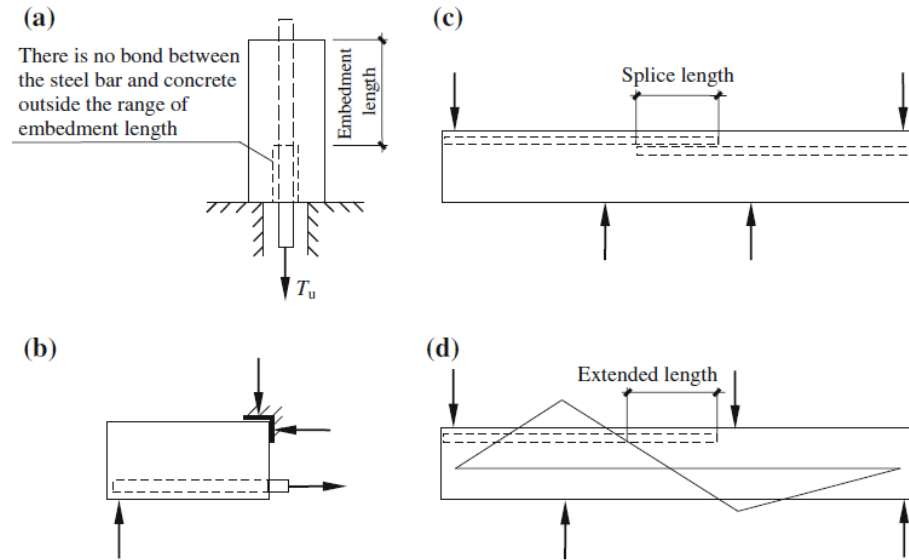
Figure 2.5: Various bond test methods used in the literature as reported in Gu et al.(2015) (reproduced with permission).

Several attempts have been made in the open literature to reduce the artefacts of this compression. The majority of these efforts were concerned with shifting the tested region furthest away from the pulled end, so that the magnitude of the compressive field subsides (RILEM/CEB/FIP 1983). Other suggested placing the bonded region in the middle of the specimen (Losberg 1963). With these modifications and others, pull-out testing is still a widely used methodology. The absence of a unified testing methodology also explains the scatter of published test results on bond in the literature.
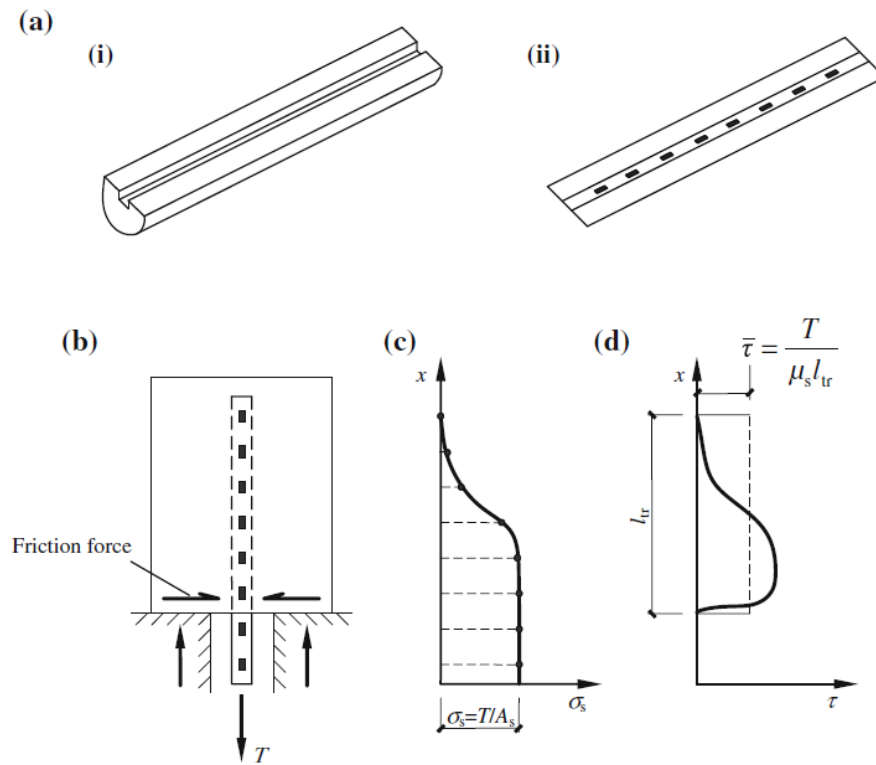
Figure 2.6: (a) (i-ii) Machining and instrumentation for determining local bond stress; (b) superficial compressive field at the boundary conditions of an anchored bar; and (c-d) bar stress and bond stress distribution along the embedment, respectively (Gu et al. (2015) reprinted with permission).

2.2.4   Bond Stresses

Bond stress, τ, can be more accurately defined as the shear stress per unit surface area of an embedded bar, as shown in **Figure 2.7**.
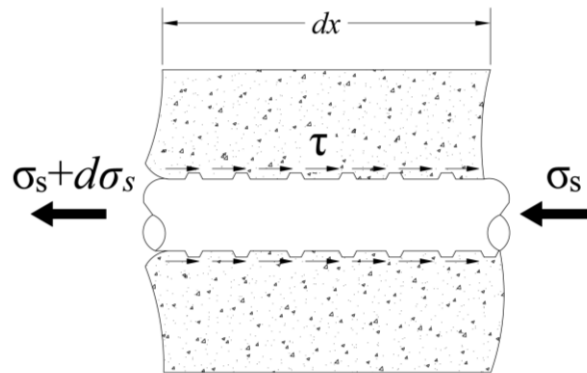
Figure 2.7: Equilibrium of a bar in a pull-out test.

Let the bond stress developed be τ; A: cross-sectional area of the bar; σ_s: bar stress; and μ_s: perimeter of the bar. To obtain an expression for τ, equilibrium of an elementary element is considered as shown in **Eq. 2.1:**

$$A\big((\sigma_s + d\sigma_s) - \sigma_s\big) = \tau \cdot \mu_s \cdot d_x \tag{2.1}$$

Simplifying and solving for τ:

$$\tau = \frac{A}{\mu_s} \cdot \frac{d\sigma_s}{d_x} \tag{2.2}$$

It can be observed from **Eq. 2.2** that the value of τ represents the local bond stress, which is defined by the relative displacement between the bar and the cementitious medium at a respective location of the anchorage. It is difficult to obtain an accurate quantitative value of τ. It is also extremely difficult to verify which ribs are engaged partially or fully, and what contribution of the load is being resisted by each rib. Local bond stresses cannot be experimentally deduced unless extensive instrumentation has been placed on the bar. This is necessary because of the change in stress in the bar along the embedment. Maekawa et al. (2005) described an experiment where the bars are split longitudinally, and strain gauges are placed along a machined grove, as shown in **Figure 2.6(a)**. They acknowledged the difficulties encountered and highlighted that this procedure was not practical.

If an average bond stress is assumed, implying that every segment of the embedment contributes to load resistance, the differential term in **Eq. 2.2** disappears, and the average bond stress $\bar{\tau}$, is calculated as follows:

$$\bar{\tau} = \frac{A}{\mu_s} \cdot \frac{\sigma_s}{l_{tr}} \tag{2.3}$$

Re-arranging and substituting, **Eq. 2.3** reduces to:

$$\bar{\tau} = \frac{T}{\mu_s \, l_{tr}} \tag{2.4}$$

Eq. 2.2 and **Eq. 2.4** are both plotted in **Figure 2.6(d)**. Three important observations can be made. First, the local bond stress varies along the embedment length, with non-linear attenuation away from the loaded end. Second, the maximum average bond stress is smaller than the maximum local stress. Third, for a given value of T applied unto the bar, only a segment of the embedment length is engaged, over which a bond stress develops that is sufficient to resist the applied load.

To help facilitate the understanding of this important concept, **Figure 2.8** plots a qualitative hypothetical distribution of the bond stress vs slip of a deformed bar in concrete. When the magnitude of the pull force is small, the stress peaks near the loaded end. This peak is accompanied by minimal slip because of the break of adhesion, at which point, the ribs begin to crush the medium. In the absence of a confinement mechanism, failure can occur at this early stage. If such mechanisms exist, the load continues to increase, pushing the distribution deeper along the embedment engaging additional ribs. Consequently, the concrete near the loaded end incurs extensive cracking and enters a state of plastification. Hence, additional ribs are engaged along the reserves of the anchorage (portions along the embedment that were not previously engaged), which shifts the distribution deeper. These reserves continue to engage until they are exhausted, after which pull-out failure is eminent.
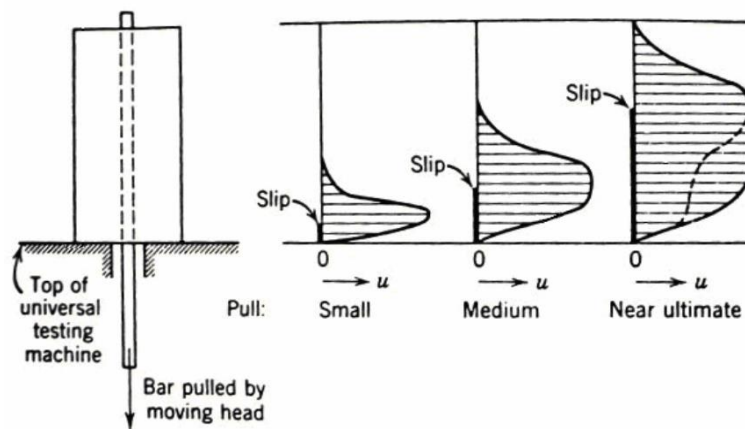
Figure 2.8: Bond stress distribution with varying levels of T (Ferguson et al. (1988) reproduced with permission).

2.3   EXPERIMENTAL STUDIES

The preceding sections described the bond of deformed bars to concrete. In the following sections, a review of the background studies on emulative connections will be examined considering the bond discussion presented above.

2.3.1   Grouted Sleeves

Grouted splices are often used to connect vertical reinforcing bars in emulative connections, as shown in **Figure 2.1**. ACI 318-014 Clause 25.5.7.1 requires mechanical coupling devices to develop at least 125% of the yielding capacity of the bar to ensure that ductility is attained (ACI Committee 318 2014). For this, a variety of coupling systems are commercially available, some of which, are extensively used in the precast industry. Research has shown that, except for the basic evaluation reports supplied by the manufacturer, the behaviour of grouted sleeves and the connections built using them require attention (Jansson 2008).

(a)   **(b)**
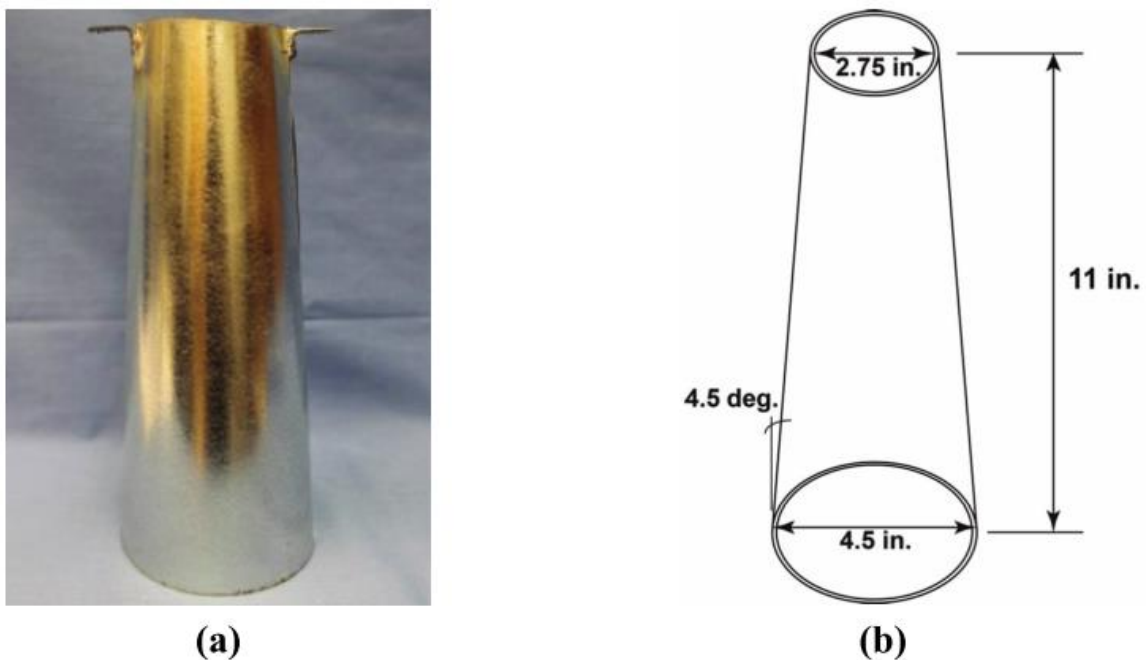
Figure 2.9: Tapered smooth grout sleeve: (a) photo; and (b) dimensions (Aragon & Kurama (2015) reproduced with permission).

A summary of the recent research efforts carried out on grouted sleeve connections is provided in **Table 2.1**. These efforts primarily consist of non-proprietary splice sleeve proposed by authors, and emulative connections utilizing these sleeves. Grouted sleeves generate high confinement stresses, thus allowing large bond stresses to develop. In most cases, 6 to 8 d_b of embedment will usually suffice to mobilize the capacity of the bars connected. Most sleeves reported were in the form of a thick-walled steel pipe, with modifications to enhance the bond internally. For example: tapered pipe diameter and welded bars (Ling et al. 2012); steel rings, steel spirals (Hosseini et al. 2015); internal threading (Henin & Morcous 2015); bolts (Sayadi et al. 2014); or a combinations thereof have been used (Ling et al. 2014). Despite their favourable performance, grouted splices require extensive machining and fabrication. They also offer poor construction tolerances, which explains why most precast fabricators prefer not to use them. The grouted sleeve proposed by Aragon & Kurama (2016) presents the most recent effort in the field. Their splice sleeve (**Figure 2.9)**, offers the same qualities as discussed above, but provides construction tolerances similar to those offered by duct connections.

Table 2.1: Synopsis of studies on grouted sleeve.

Authors	Specimen Description	Specimen Tag	Grout Strength (MPa)	Bar Dia. (mm)	L_d (mm)	Sleeve Dia (mm)	Peak Load (kN)	Failure Types	Main Findings
(Einea, Yamane, and Tadros 1995)	Grouted sleeve with a spliced reinforced bar under direct tension.	Type 1-1	44 - 68	29	254	76.2	364		Strength of the bar using a simple steel tubing. Increasing compressive strength and confinement pressure provided shorter development lengths. More tests on various grout strength and other sleeve geometries are necessary. Cyclic and fatigue loading investigations are necessary to further understand the performance of the connection. Specimens that were spliced using in-line splices were the most suitable from a construction tolerance perspective.
		Type 1-2			203		341		
		Type 1-3			152		294		
		Type 2-1		19	203	50.8	181	Bond Failure	
		Type 2-3			152		119		
		Type 3-2			152		113		
		Type 3-3			127		105		
		Type 3-5			152		199	Bar Fracture	
		Type 3-6			127		147		
		Type 4-1		16-19	127	38.1	133	Bond Failure	
		Type 4-2			152		198		
(Henin and Morcous 2015)	Grouted sleeves with a spliced reinforced bar using a non-proprietary sleeve.	8T16	67.5	25	406	76.2	383	Pull out	The spliced connections achieved strength equivalent to 100% of the ultimate tensile strength of the bar within a development length of 16-in. This was attributed to an increase in confinement offered by the sleeve.
		8P16			406		384	Bar Pullout	
		8T18			457		385	Rupture	
		8T20			508		378		
		9T16			406		403		
		9P16		29	406		444	Bar Pullout	
		9T20			508		458	Rupture	
		9P20			508		431		
(Hosseini et al. 2015)	Pullout and beam specimens consisting of a bar splice inside a spiral sleeve.	S1-A	62	16	160	25	24	Grout Failure	The bond strength increased by 34% when the spiral diameter decreased from 45 to 15 mm. The confinement effect of the spiral (sleeve) played an important role in reducing the length required to develop the bars.
		S3-A				25	70		
		P15 D25-A				25	70	Bar Pull-out	
		P15 D35-A				35	60		
		P15 D45-A				45	52		
		P25 D35-A				35	59		
		P25 D45-A				45	50		
		P35 D25-A				25	66		
		P35 D35-A				35	58		
		P35 D45-A				45	49		
(Ling et al. 2012)	Spliced sleeve specimen tested under incremental tensile loads.	AS-01	58	16	150	43-65	133	Bar Fracture	A variety of spliced sleeve connectors were tested to determine the feasibility of their use to replace mechanical couplers. The tensile capacity of the sleeve, bar-grout bond, and the sleeve-concrete bond were detrimental factors on the performance of the connection. The authors recommended testing the connection under cyclic loading.
		AS-02			300		12	Sleeve Fracture	
		BS-01	63		150		136	Bar Fracture	
		BS-03					119		
		CS-01			100		87		
		CS-02	43		50		98	Bond Failure	
		CS-03			150		80		
		DS-01	49		150		129	Bar Fracture	
		DS-03					123	Bar Fracture	
(Ling, Ahmad, and Ibrahim 2014)	Spliced sleeve specimen tested under incremental tensile loads.	WBS-1	50	16	75	50	86	Bar Slip	The tensile capacity of the sleeve played a vital role in the ultimate tensile capacity of the splice connecter. This is because it bridges the gap that exists between the two in-line spliced bars. Sleeves with mechanisms that engage more mechanical interlock in the concrete generate superior bond capacities. Analytical and experimental results are in agreement.
		WBS-3				75	75		
		WBS-4			125	50	132	Bar Fracture	
		WBS-6				75	126	Bar Slip	
		WBS-7			175	50	134		
		WBS-9				75	133	Bar Fracture	
		THS-1			75	50	112		
		THS-3				75	96	Bar Slip	
		THS-4			125	50	137		
		THS-6				75	135	Bar Fracture	

2.3.2 Grouted Connections Under Monotonic Loads

As highlighted earlier, grouted connections offer favourable advantages, including weld elimination and forgiving erection tolerances. The use of these connections is not customarily restricted to precast wall construction, but is rather used to connect a variety of precast elements including columns, walls, beam-column connections, and bridge bent caps. Despite their increased use, research has shown that sparse information is currently available on the bond of such connections. Additionally, a reliable equation to accurately predict the required development length is yet to be developed. The following is a summary of the major research findings in the literature. For additional information, the reader is referred to Chapters 3 and 4, Sections 3.1 and 4.1, respectively.

Amongst the earliest observations made on grouted connections were those presented by Crisafulli et al. (2002), where the performance of lightly reinforced precast concrete wall panels for use in areas of high seismicity has been examined. The walls were connected using two 16 mm diameter dowels with embedment lengths equal to 43 d_b grouted into 50.8 mm diameter corrugated ducts. Despite the satisfactory performance of the connection, the embedment length (43 d_b) was likely overdesigned. This observation was based on strain measurements taken along the connecting bar, which found peak strains developed at the connection and decreased nearly linearly over 20 d_b once the yield strength was reached (Crisafulli et al. 2002).

Raynor et al. (2002) were among the earliest studies focusing specifically on the bond of grouted connections. They examined the use of these connections in precast framing systems, what later came to be known as hybrid frames. These frames use a combination of post-tensioning and mild steel to achieve superior ductility. Beam-columns of such frames are typically connected using grouted connections, where a certain length of the bar is de-bonded to reduce strains and prevent low cycle fatigue. The bars had short embedment lengths and were tested using monotonic and cyclic loading. Exceptionally high bond stresses were observed and were attributed to the confinement effect of the duct.

Most of the remaining studies on grouted connections revolve around the use in precast segmental construction, specifically bridge bent cap systems. For instance, Brenes et al. (2006) undertook a comprehensive study to explore the influence of changing the corrugated duct materials on the behaviour of grouted connections used in bridge cap systems. The main test parameters investigated were the bar coating, duct material, transverse reinforcement, bar eccentricity and number of connections. It was observed that the behaviour of grouted connections was largely dependent on the stiffness of the duct material and its ability to accommodate lateral strains.

Steuck et al. (2009) conducted pull-out tests on large diameter bars grouted in vertical ducts to be used in a bridge bent cap system. A total of 14 pull-out tests were conducted on bars with varying sizes and embedment lengths, with or without the addition of polypropylene fibre reinforcement. Embedment lengths 3 times smaller than that recommended by the ACI 318-05 were sufficient to mobilize the tensile capacity of the bar. This was ascribed to the additional passive confinement provided by the duct. However, the test setup was done to replicate a bridge bent cap system, using a much larger concrete block than a wall connection would require. This extra concrete contributes greater confinement. Additionally, this research focused on large diameter bars (d_b = 32 mm, 43 mm, and 57 mm) with a larger duct/bar ratio (3.6). Typical wall panel connections use 25 mm diameter bars with a duct/bar ratio of 3.0.

Mandawe et al. (2002) and Matsumoto et al. (2008) investigated the performance of precast bridge bent caps equipped with grouted vertical duct connectors. Their study examined the cyclic behaviour of epoxy-coated 28.5 mm bars embedded in galvanized steel ducts. It was concluded that bars embedded 10 d_b failed by yielding of the bar before pull-out, while specimens embedded 16 d_b failed by bar fracture.

Based on the conclusions made from the survey of studies available, there is consensus on the differentiation between the bond failure of deformed bars grouted in corrugated ducts and that of deformed bars in concrete. Most pertinent studies dealt with the use of grouted connections in precast bent cap systems where the specimens' dimensions were different, which influences the bond behaviour. Additionally, these studies reported empirical

models to predict the behaviour of such connections based on experimental testing (Matsumoto et al. 2008; Einea et al. 1999; Steuck et al. 2009; Brenes et al. 2006). Considering the sensitivity of bond to various influential factors, the results of these studies cannot be extrapolated to the behaviour of grouted connections used in precast walls. In view of the sparsity of information available on the behaviour of grouted connections used in precast walls, a dedicated experimental methodology is yet to be conducted to explore the behaviour of the connections in precast walls.

2.3.3   Grouted Connections Under Cyclic Loads

Very limited information is available on the cyclic behaviour of grouted connections. This sparsity was highlighted in the ACI Committee 408.2R and is reflected in the mere fact that only one study was found in the open literature addressing this topic directly. The investigation conducted by Raynor et al. (2002) studied grouted connections typically used in hybrid precast frames (small cover/diameter ratio). The specimens were subjected to constant amplitude and variable displacement histories. The bars had short embedment and the specimens were sufficiently confined. A comparison between the response of the connections under monotonic and cyclic loading is presented in **Figure 2.10**. Their experimental results indicate that bond stresses due to cyclic loads are 10 to 70% less than those from monotonic loading, depending on the level of slip. However, the reported data in this study were mostly qualitative and lacked experimental evidence on the real failure mechanisms.

Other studies reported on precast walls briefly reported on behavioural aspects of these connections. For example, Seifi et al. (2015) tested under cyclic loading, precast walls having grouted connections that use 16 mm bar and a grouted length of 37.5 d_b. The panels did not suffer premature failure and displayed favourable ductile behaviour characterized by panel sliding via yielding and elongation of the connection reinforcement. Other studies acknowledged the ductility and favourable energy dissipation of grouted connections. However, large embedment lengths were used in such studies and no information pertaining to the bond of the connections was reported.
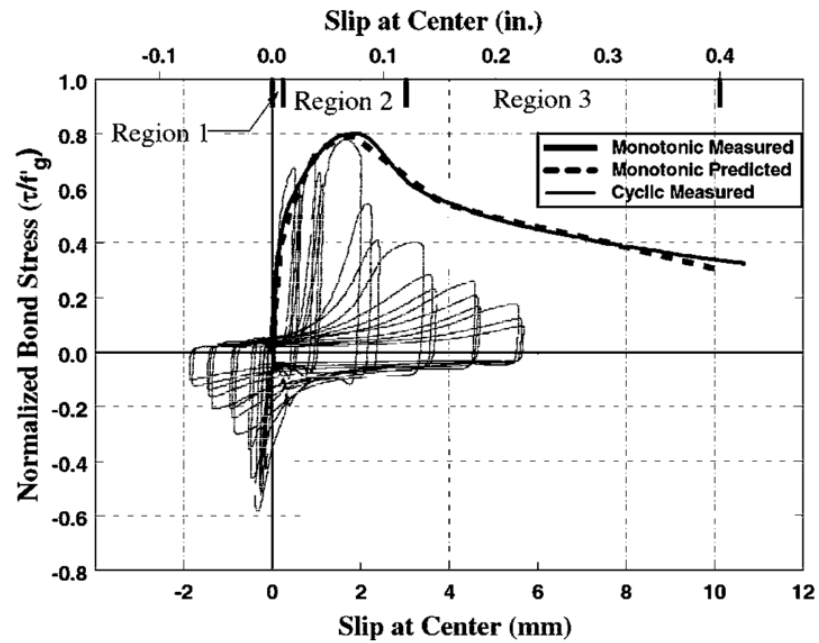
Figure 2.10: Comparison between the bond-slip response of grouted connections under monotonic and cyclic loads after Raynor et al. (2002) (reprinted with permission).

Kang et al. (2013) explored the behaviour of precast concrete wall panels subjected to cyclic lateral loading to evaluate the energy dissipation and ductility of emulative precast walls. They examined the concept of a weaker dowel connection through partial reduction of the bar cross-sectional area, which would result in greater ductility. This is because the weaker connection pushes the plastic hinge formation away from the horizontal joint between the panel and the base, thus resulting in avoidance of local failures anticipated at the joints in the form of shear slip and gap opening. Results revealed that, although the specimen with a reduced rebar connection sustained 30% lower load than that of its non-reduced counterparts, improvements in energy dissipation capabilities and ductility were observed.

Balleri & Riva (2012) investigated the cyclic behaviour and post-seismic repair of columns connected to foundations using grouted connections. Six specimens were considered in the study. Five specimens had different connection configurations with similar bending moment capacities. One specimen was retrofitted and retested. Specimens were tested under constant 600 kN compressive load and cyclic lateral load was applied atop the column, increasing the drift from 0.25 to 5%. Results indicated the suitability of using

grouted duct connections where large seismic demand is anticipated. The increased ductility of the duct connection was attributed to the confining effect of the duct on the grout, which was transferred to the reinforcing bar.

Similar observations were also reported by Popa et al. (2015) when they compared grouted connections to cast-in-place concrete. They noted that the cast-in-place specimen dissipated more energy, yet had more severe damage than that of the precast specimen. It was concluded that the grouted connection was sufficient for use in column-foundation connections subjected to high seismicity. However, in both preceding studies, the connection length was designed as a reinforcing bar in concrete, likely overestimating the required embedment length.

Considering the lack of data pertaining to the cyclic behaviour of grouted connections, further testing and experimental evidence is yet to be conducted and presented to address these knowledge gaps.

2.3.4   Bond-Slip Modelling of Grouted Connections

Most available bond slip models are based on phenomenological observations rather than analytical or mechanistic approaches. A closed form solution to **Eq. 2.2** is difficult, but may be possible under limited contexts. Considering the compatibility of the longitudinal slip-bar strain; and longitudinal slip-radial translation, under various strain and slip domains quickly complicates the problem. As mentioned earlier, it is extremely difficult to know the contribution of lugs to the load capacity. It is also not feasible to deduce such a relationship when the bond and bar enter a state of plastification. Several attempts have been made to approach this problem analytically, for example, Tepfers (1973).

Amongst most recent analytical efforts in this pursuit is the work of Tastani & Pantazopoulou (2013), where the governing differential equations were solved separately for the concrete cover and the bar. They were later coupled using kinematic conditions derived from experimental observations from earlier studies (Tastani & Pantazopoulou 2010). While the model was found to be in good agreement when compared with bond

experiments by the same authors utilizing the same form, no corroboration was undertaken with external studies, which makes the applicability of such model questionable.

Results of such calibrated analytical expressions, when used to correlate results from the international database of bond tests, produces significant scatter. Several plausible explanations can explain this. First, the local bond slip law required to calibrate these analytical expressions is not reported in most studies. Researchers on bond often report average bond stresses for the reasons discussed above. Second, bond is never measured directly. It is only observed through the complex response of a tested specimen, whereby the superficial stresses often obscure the mechanics of bond.

Considering this, phenomenological models based on results from specimens utilizing good form (specimen form reducing or eliminating boundary effects) usually perform better in corroborative efforts. The monotonic bond-slip law presented by Eligehausen et al. (1982) is shown in **Figure 2.11**. Commonly known as the BPE model, this forms the basis of most bond-slip laws proposed by other researchers in most recent studies, with some modifications. This bond slip law was also adopted by the European Model Code (CEB-FIP 2010). A detailed discussion of model equations and their highlights is presented in Chapter 6.
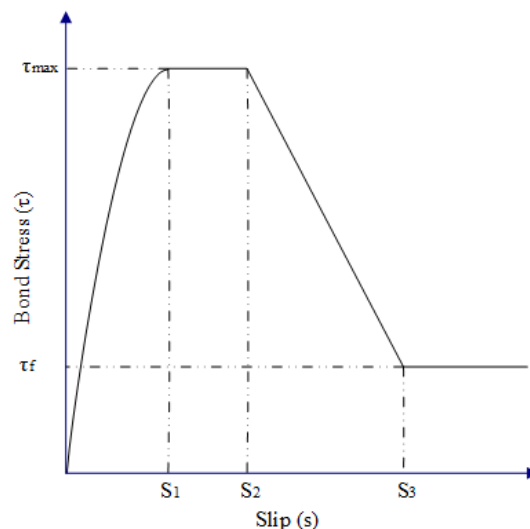
Figure 2.11: Bond-slip law after Eligehausen et al. (1982)

A summary of the bond modelling efforts of grouted connections is graphically illustrated in **Figure 2.12**. The first efforts made to model grouted connections were presented by Raynor (2000) and Raynor et al. (2002). This was achieved by fitting a large set of experimental data obtained from testing grouted connections in hybrid frames. The bond-stresses recorded were exceptionally high. This was due to the grout characteristics and the unusually low duct-bar ratio. Steuck et al. (2009) also deduced a similar model for grouted connections to be used in bridge cap segmental construction. The bars used were No.10 – 18. The duct-bar ratio was unusually large is customarily in bridge cap construction. The effect of the specimen form and method of testing on the bond-slip models is evident from comparison of the models. One of the objectives of this work is to arrive at a phenomenological model reflective of the behaviour of grouted connections in precast walls. The calibrated law would then be used in a Finite Element (FE) platform to model grouted connections. Discussion of the model derivations and constitutive relationship along with the FE model are presented in Chapter 6.
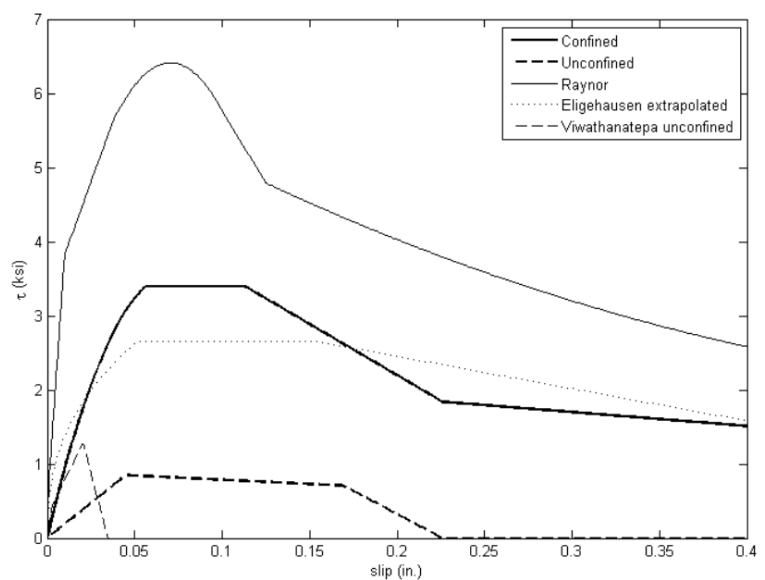
Figure 2.12: Comparison of bond-slip models of grouted connections (Steuck et al. 2009).

2.4   CODES AND STANDARDS

The PCI Design Handbook provides governing design and construction specifications of grout-filled metallic conduit connections (PCI 2010). It specifies a minimum concrete cover of 76.2 mm; a minimum duct thickness of 0.6 mm; 9.5 mm of minimum clearance around the bar; and a grout compressive strength of no less than 35 MPa. Typically, a large diameter bar (20-30 mm) is used in a grout-filled bar connection depending on the size of the wall and its lateral loads. The length of connection is governed by the development length in tension as per clauses of the ACI-318-14. The minimum specified development length of a 25 mm bar is 1067 mm for 35 MPa concrete (ACI Committee 318 2014; PCI 2010). The minimum embedment length of any bar should not be less than 305 mm.

Before presenting common expressions used to design grouted connections, it is prudent to highlight the basis of such expressions. Starting from **Eq. 2.3**, and substituting $A = \frac{\pi}{4} d_b^2$ and $\mu_s = \pi d_b$, we arrive at **Eq. 2.5**:

$$\bar{\tau} = \frac{d_b}{4} \cdot \frac{\sigma_s}{l_{tr}}$$ (2.5)

Re-arraning and solving for the bar stress results in **Eq. 2.6**:

$$\sigma_s = 4 \cdot \bar{\tau} \frac{l_{tr}}{d_b}$$ (2.6)

and:

$$l_{tr} = \frac{\sigma_s}{4 \cdot \bar{\tau}} d_b$$ (2.7)

Eq. 2.7 forms the basis for code development length design equations with some adaptations to account for a variety of influential factors.

The ACI 318-14 and the Association of State Highway and Transportation Officials (AASHTO 2017) provide equations to calculate the development length required to mobilize and fully develop a bar. The ACI equation is given by **Eq. 2.8** expressed as follows:

$$L_d = \left(\frac{3}{40} \frac{f_y}{\sqrt{f_c'}} \frac{\psi_l \psi_e \psi_s \lambda}{\left(\frac{c_b + k_{tr}}{d_b} \right)} \right) d_b \qquad (2.8)$$

Where: L_d = tension development length in in.; f_y = specified yield strength of the bar psi; ψ_l = reinforcement location factor; ψ_e = reinforcement coating factor; ψ_s = reinforcement size factor; λ = lightweight aggregate factor; c_b = cover dimension measured from center of the bar; and k_{tr} = transverse reinforcement index.

Eq. 2.8 is based on the work of Orangun et al. (1975) and relies on the assumption that the bond strength is proportional to $\sqrt{f_c'}$. It also includes an embedded steel stress factor of 1.25 to satisfy ductility requirements; a strength reduction factor, ϕ equal to 0.9 to give consideration for deviations in material properties. An upper theshold limit of 2.5 is placed on the term $\left(\frac{c_b + k_{tr}}{d_b} \right)$ and a more conservative value of 1 is encouraged. This limitation on the confinement factor is to safeguard against pullout type failures.

AASHTO provides three equations depending on the diameter of the bar. For a No. 8 bar, **Eq. 2.9** can be used:

$$L_d = \frac{1.25 A f_y}{\sqrt{f_c'}} \qquad (2.9)$$

Eq. 2.9 is adopted with minor modifications from ACI 318-71. The differences between the two terms are due to a unit conversion factor from psi to ksi, and some minor rounding of the coefficients.

2.5 REFERENCES

AASHTO, 2017. LRFD Bridge Design Specifications. *American Association of State Highway and Transportation Officials, Atlanta GA, USA*, pp.1–1780.

ACI Committee 318, 2014. Building Code Requirements for Structural Concrete and Commentary. *American Concrete Institute, Farmington Hills, MI, USA*, pp.1–519.

ACI Committee 408, 2003. Bond and Development of Straight Reinforcing Bars in Tension. *American Concrete Institute, Farmington Hills, MI, USA,*, pp.1–49.

ACI Committee 408.2R, 2012. Report on Bond of Steel Reinforcing Bars Under Cyclic Loads. *American Concrete Institute, Farmington Hills, MI, USA*, p.39.

ACI Committee 550, 2001. Emulating Cast-in-Place Detailing in Precast Concrete Structures. *American Concrete Institute, Farmington Hills, MI, USA*, pp.1–16.

Aragon, T.C. & Kurama, Y.C., 2015. A Type III Tapered-Cylindrical Grouted Splice for Energy Dissipation Bars in Seismic Precast Concrete Joints. In *ASCE Structures Congress 2015*. Portland, OR, pp. 1999–2009.

Aragon, T.C. & Kurama, Y.C., 2016. Preliminary Testing of a Type III Tapered-Cylindrical Grouted Seismic Connector for Ductile Deformed Steel Rebar. In *PCI Convention and National Bridge Conference*. Nashville, TN, pp. 1–13.

Balleri, A. & Riva, P., 2012. Seismic performance and retrofit of precast concrete grouted sleeve connections. *PCI Journal*, 57(1), pp.97–108.

Brenes, F.J., Wood, S.L. & Kreger, M.E., 2006. Anchorage Requirements for Grouted Vertical-Duct Connectors in Precast Bent Cap Systems. In *Texas Department of Transportation Technical Report No. FHWA/TX-06-4176-1*. pp. 1–251.

Cairns, J. & Jones, K., 1996. An evaluation of the bond-splitting action of ribbed bars. *ACI Materials Journal*, 93(1), pp.10–19.

CEB-FIP, 2010. Model Code 2010. *Federation Internationale du Beton, Lausanne, Switzerland.*, pp.1–292.

Crisafulli, F.J., Restrepo, J.I. & Park, R., 2002. Seismic Design of Lightly Reinforced Precast Concrete Rectangular Wall Panels. *PCI Journal*, 47(4), pp.104–121.

Darwin, D. & Zavaregh, S.S., 1996. Bond Strength of Grouted Reinforcing Bars. *ACI Structural Journal*, 93(4), pp.486–495.

Einea, A., Yehia, S. & Tadros, M.K., 1999. Lap splices in confined concrete. *ACI Structural Journal*, 96(6), pp.947–955.

Eligehausen, R., Popov, E.P. & Bertero, V. V., 1982. Local bond stress-slip relationships of deformed bars under generalized excitations. *NSF Report No. UCB/EERC-82/23*, pp.69–80.

Ferguson, P.M., Breen, J.E. & Jirsa, J.O., 1988. *Reinforced Concrete Fundamentals*, Wiley.

Gu, X., Jin, X. & Zhou, Y., 2015. Basic Principles of Concrete Structures. *Springer*, pp.1–596.

Henin, E. & Morcous, G., 2015. Non-proprietary bar splice sleeve for precast concrete construction. *Engineering Structures*, 83, pp.154–162.

Hosseini, S.J.A. et al., 2015. Bond behavior of spirally confined splice of deformed bars in grout. *Construction and Building Materials*, 80, pp.180–194. Available at: http://linkinghub.elsevier.com/retrieve/pii/S0950061814013993.

Jansson, P., 2008. Evaluation of Grout-Filled Mechanical Splices for Precast Concrete Construction. *Michigan Department of Transportation Report No. 07 TI-2094*, pp.1–72.

Kang, S.-M., Kim, O.-J. & Park, H.-G., 2013. Cyclic loading test for emulative precast concrete walls with partially reduced rebar section. *Engineering Structures*, 56, pp.1645–1657.

Ling, J.H. et al., 2012. Behaviour of grouted pipe splice under incremental tensile load. *Construction and Building Materials*, 33, pp.90–98. Available at: http://dx.doi.org/10.1016/j.conbuildmat.2012.02.001.

Ling, J.H., Ahmad, A.B. & Ibrahim, I.S., 2014. Feasibility study of grouted splice connector under tensile load. *Construction and Building Materials*, 50, pp.530–539. Available at: http://dx.doi.org/10.1016/j.conbuildmat.2013.10.010.

Losberg, A., 1963. Force transfer and stress distribution at anchorage and curtailment of reinforcement. *Chalmers University of Technology Rep. No. 608*, pp.1–49.

Lutz, L.A. & Gergely, P., 1967. Mechanics of Bond and Slip of Deformed Bars in Concrete. *ACI Journal Proceedings*, 64(11), pp.711–721.

Maekawa, K., Okamura, H. & Pimanmas, A., 2005. Non-linear mechanics of reinforced concrete. *Taylor and Francis*, pp.1–2005.

Mandawe, J., Mislinski, S. & Matsumoto, E., 2002. Reinforcement Anchorage in Grouted Duct Connections for a Precast Bent Cap System in Seismic Regions. In *PCI/FHWA Concrete Bridge Conference*. Nashville, TN.

Matsumoto, E.E. et al., 2008. Development of a precast concrete system. *PCI Journal*, 53(3), pp.74–86.

Orangun, C.O., Jirsa, J.O. & Breen, J.E., 1977. A Reevaluation of Test Data on Development Length and Splices. *Journal of the American Concrete Institute*, 74(3), pp.114–122.

Orangun, C.O., Jirsa, J.O. & Breen, J.E., 1975. Strength of anchored bars: a reevaluation of test data on development length and splices. *Texas Highway Department Research report no. 154-3F1975*, pp.1–90.

Park, R., 1995. A perspective on the seismic design of precast concrete structures in New Zealand. *PCI Journal*, 40(3), pp.40–60.

Popa, V. et al., 2015. Experimental testing on emulative connections for precast columns using grouted corrugated steel sleeves. *Bulletin of Earthquake Engineering*, 13(8), pp.2429–2447.

Raynor, D.J., 2000. Bond Assessment of Hybrid Frame Continuity Reinforcement. *M.Sc Thesis, University of Washington*.

Raynor, D.J., Dawn, E.L. & Stanton, J.F., 2002. Bond-Slip Response of Reinforcing Bars

Grouted in Ducts. *ACI Structural Journal*, 99(5), pp.568–576.

Restrepo, J., Park, R. & Buchanan, A., 1993. Seismic behaviour of connections between precast concrete elements. *University of Canterbury, Research Report No. 93-3*.

RILEM/CEB/FIP, 1983. Bond test for reinforcement steel. 2. Pull-out test. *Recommendation RC6*.

Sayadi, A. et al., 2014. The relationship between interlocking mechanism and bond strength in elastic and inelastic segment of splice sleeve. *Construction and Building Materials*, 55, pp.227–237.

Seifi, P., Henry, R.S. & Ingham, J., 2015. Preliminary test results of precast concrete panels with grouted connections. In *New Zealand Society for Earthquake Engineering Technical Conference*. Rotorua, New Zealand, pp. 744–751.

Steuck, K.P., Eberhard, M.O. & Stanton, J.F., 2009. Anchorage of large-diameter reinforcing bars in ducts. *ACI Structural Journal*, 106(106), pp.506–513

Tastani, S.P. & Pantazopoulou, S.J., 2010. Direct Tension Pullout Bond Test: Experimental Results. *Journal of Structural Engineering*, 136(6), pp.731–743.

Tastani, S.P. & Pantazopoulou, S.J., 2013. Reinforcement and concrete bond: State determination along the development length. *ASCE Journal of Structural Engineering*, 139(9), pp.1567–1581.

Tepfers, R., 1973. A Theory of Bond Applied to Overlapped Tensile Reinforcement Splices for Deformed Bars. *PhD Thesis, Chalmers University of Technology*, pp.1–330.

Treece, R.A. & Jirsa, J.O., 1989. Bond Strength of Epoxy-Coated Reinforcing Bars. *ACI Materials Journal*, 86(2), pp.167–174.

Untrauer, R.E. & Henry, R.L., 1965. Influence of normal pressure on bond strength. *ACI Journal Proceedings*, 62(5), pp.577–586.

Zuo, J. & Darwin, D., 1998. Bond Strength of High Relative Rib Area Reinforcing Bars. *University of Kansas Center for Research Report No. 46*, pp.1–346.

Zuo, J. & Darwin, D., 2000. Splice strength of conventional and high relative rib area bars in normal and high-strength concrete. *ACI Structural Journal*, 97(4), pp.630–641.

Chapter 3

3 EXPLORATORY INVESTIGATION OF GROUTED CONNECTIONS UNDER DIRECT TENSILE LOAD

3.1 INTRODUCTION

Grouted reinforcing bar connections (or simply grouted connections) are versatile ties widely used in precast construction to resist tensile loads. The connection is attractive due to its simple application, forgiving tolerance, and weld elimination. It is generally comprised of a large diameter reinforcing bar (usually 25 mm or greater) projected from one panel and grouted into a metallic duct placed in the other, as shown in **Figure 3.1.** Despite their increased use in precast wall construction, a limited number of studies have been devoted to study the behaviour of such connections.
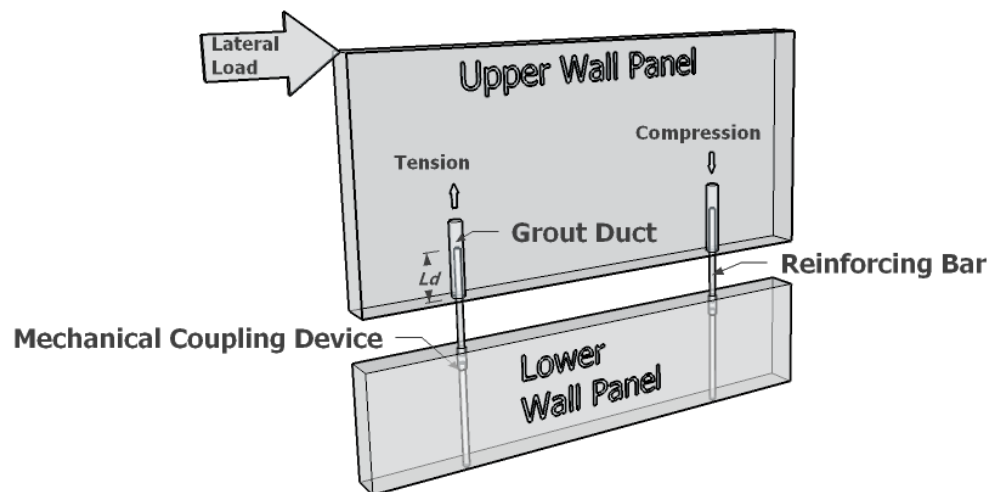
Figure 3.1: Grouted connection and its use in precast walls.

The use of grouted connections in precast wall buildings generally satisfies one of two requirements: (i) structural integrity (Section 16.2.5 in the ACI 318-14), which prevents progressive collapse (ACI Committee 318 2014); and (ii) as a ductile device used to yield

when subjected to large in-plane deformations. Currently, the grouted length of the connections is determined per the provisions of ACI 25.4.2.3 based on the minimum development length in tension. The minimum specified development length of a No. 8 bar is 1067 mm for a 28 MPa concrete and the minimum embedment length of any bar should not be less than 305 mm (ACI Committee 318 2014; PCI 2010). This usually results in excessive grouting lengths and introduces a plane of reduced stiffness at the interface between the connection and the wall (Seifi et al. 2015). A recent study by the present authors emphasized the differences between grouted connections and the current code treatment (Elsayed & Nehdi 2017).

Raynor et al. (2002) investigated the behaviour of grouted connections used in hybrid frames using short bar embedment lengths under monotonic and cyclic pull-out loads. They concluded that bars embedded in corrugated ducts behave differently from their non-ducted counterparts, primarily due to the confinement effect of the duct. Steuck et al. (2009) performed pull-out tests on grouted connections used in bridge bent cap structures, where a large diameter bar (No. 10, 14, and 18) is customarily used. The corrugated duct generated confinement sufficient to suppress splitting failures of the concrete. Similar studies on bridge bent cap structures were conducted by Brenes et al. (2006) and Matsumoto et al. (2008) who explored various configurations of the connection and reached similar conclusions. Belleri & Riva (2012) showed that grouted connections used in column-footing assemblies have favourable ductility compared to that of monolithic assemblies, attributing this to the additional confinement effect of the duct. Although there is agreement among the limited number of studies on the additional confinement imparted by the corrugated duct, quantitative supporting evidence has often not been provided.

Most of the published literature on grouted connections pertains to its use in bridge bent cap structures. Bond is not measured directly and is known to be sensitive to several influential factors such as the cover-to-bar ratio, testing configuration, material properties, and confinement. Hence, the relevant sparse experimental results and associated models cannot be directly extrapolated to the specific case of grouted connections used in precast walls. Accordingly, the present study is a dedicated experimental methodology to address these knowledge gaps. The specific objectives of this paper are: i) provide quantitative and

qualitative experimental evidence on the behaviour of grouted connections in precast walls; ii) examine the behaviour of grouted connections equipped with Fibre Reinforced Polymer (FRP) bars that can be used in non-seismic application; and iii) develop and calibrate suitable analytical treatments to explain the behaviour of these connections.

3.2   EXPERIMENTAL PROGRAM

In the present study, 22 full-scale pull-out tests were carried out to investigate the behaviour of grouted connections. The main test parameters are shown in **Table 3.1**, were:

Table 3.1: Matrix of tested parameters

		Parameters					
		Embedment Length				[1] Duct	
		6	8	10	12	D	ND
Bar Type	Grade 60	x	x	x	x	x	x
	Grade 100	x			x	x	
	BFRP	x			x	x	
	GFRP	x			x	x	

[1] *D and ND refer to ducted and non-ducted, respectively*

- **Embedment length**: anchored lengths of 6, 8, 10 and 12 d_b (where d_b is bar diameter) were chosen to explore the bond over short and medium anchorages.
- **Bar type**: the bars tested included Grade 60 and Grade 100 rebar, Glass FRP, and Basalt FRP. Bars were selected to examine the bond behaviour of grouted connections under different bar strain domains and the associated effect on the bond (e.g. Grade 60 (plastic bar strain); Grade 100 (elastic bar strain); FRP (elastic bar strain)). Exploring the effects of different strain levels and surface treatments of bars responds to specific construction needs. For example, ductile bars were studied for use in panels subjected to large tensile and ductility demands. FRP bars were considered in light panels to satisfy structural integrity requirements.
- **Duct**: both ducted and non-ducted specimens were considered to investigate the role of the corrugated duct. Specimen details, materials properties and test methodology are presented below.

3.2.1 Materials Properties

Table 3.2: Concrete mixture proportions

Materials	Per 1 m^3
CSA Type 30 Cement	435 kg
Sand	842 kg
14 mm aggregate (round)	842 kg
Water	200 Litres
Air	5%
Air Entrainment/Lubricant	20 ml/100 kg cement
High Range Water Reducer	630 ml/100 kg cement
Total	2,322 kg

Self-consolidating concrete having average 28-d compressive (ASTM C39 2016) and splitting tensile strengths (ASTM C496/C496M 2011) of 50.6 MPa and 4.9 MPa, respectively was used to pour the specimens. Its mixture proportions are shown in **Table 3.2**. A high-strength non-shrink grout with an average 28-d compressive strength of 39.3 MPa and tensile strength of 6 MPa was used. Mechanical properties of the concrete and grout are summarized in **Table 3.3**. The mechanical properties of the various bars measured per ASTM guidelines (ASTM 370 2014) are reported in **Table 3.4.** The dowel bars used included Grade 60 and Grade 100 rebar along with GFRP and BFRP bars (**Figure 3.2**). Bars were sourced from a single production from one supplier. Ductile Grade 60 and 100 rebars had ribs, which were 5.1 mm and 4.5 mm, respectively. The relative rib area for both bars was equal to (0.15). Elastic BFRP was of a generic type and pultruded using an epoxy resin. BFRP bars had uniform spiral indentations of 2.6 mm spaced at 10.5 mm. GFRP was sourced from Pultrall (V-rod Type). According to the manufacturer's specifications, GFRP bars were pultruded using a Vinyl ester resin. The bars had a uniform sand coating along its length. Detailed mechanical properties of the bars are given in **Table 3.4**.

Table 3.3: Mechanical properties of concrete and grout

Material	Age	Compressive Strength (MPa)	Tensile Strength (MPa)	Young's Modulus (MPa)	Poisson's Ratio
Concrete	7	43.1	4.2	26,075	0.255
	Testing Day	50.6	4.9	26,036	0.234
Grout	7	38.4	4.5	20,712	0.229
	Testing Day	39.3	6.3	22,713	0.235

Table 3.4: Mechanical properties of bars

Bar Type	Diameter (mm)			Rib height	Yield Stress (MPa)		Tensile Strength (MPa)		Strain at Failure (%)	
	Nominal	Measured			Nominal	Measured	Nominal	Measured	Nominal	Measured
		With ribs	Without ribs							
Steel	25.40	26.24	23.17	1.535	400	421	602.0	598.0	21.0	24.4
GFRP	26.99	30.52		-	-	-	1,264.0	1,063.1	2.0	2.1
BFRP	25.00	24.72		0.71	-	-	613.0	757.0	3.1	1.7
X100	25.40	27.57	24.27	1.650	690	800	1,158.0	1,220.7	10.0	18.7

Grade 60		
Grade 100		
BFRP		
GFRP		
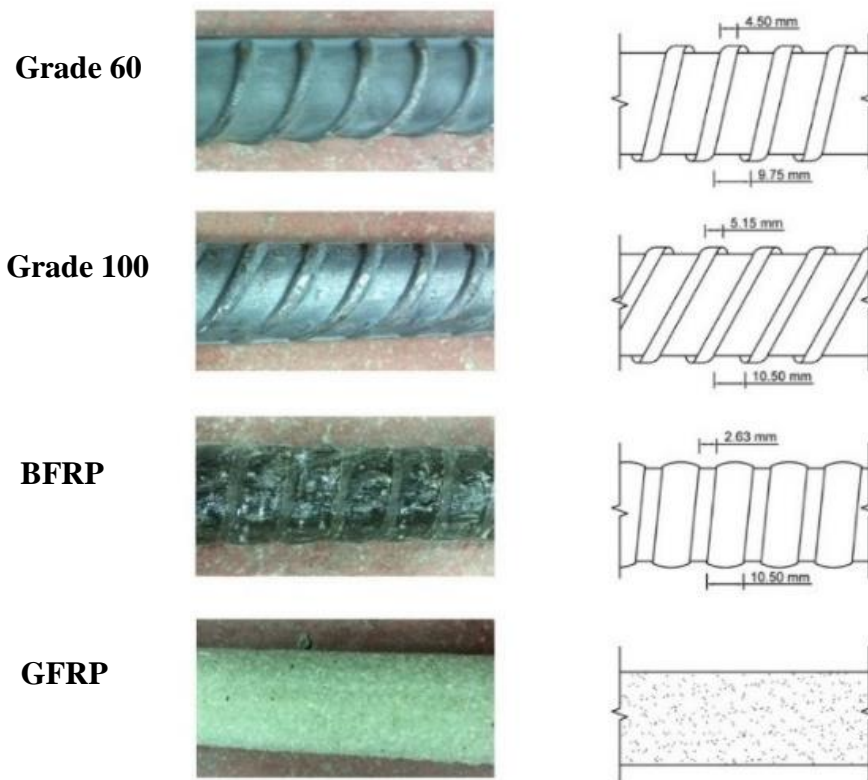
Figure 3.2: Bar types

3.2.2   Test Specimens

Grouted specimens used in this study are based on actual connections of a typical precast bearing wall (10 ft x 10 ft x 8 in). They mimic actual loading, dimensions, materials and curing conditions encountered in the field. A depiction of a test specimen is shown in **Figure 3.3**. A non-reinforced rectangular concrete prism with a cross-section of 203.2 mm x 203.2 mm was used to represent the portion of a wall with a grouted connection. The concrete prisms were intentionally non-reinforced (as opposed to mesh reinforcements found in typical precast walls) to capture a conservative view of their bond behaviour. A 76.2 mm, 30-gauge thick corrugated duct was placed concentrically in the specimen. After concentric placement of the bars inside the duct, the specimens were grouted (in the vertical direction) with a non-shrink high-strength grout, which was mixed at low speed for 10 minutes then at high speed for 5 minutes, adding water until a flowing consistency was achieved (3.75 L/25 kg). The top and bottom segments of the bar were de-bonded using a

2 mm (14 gauge) thick polystyrene wrap. Both the concrete and the grout were individually left to cure after casting. All specimens were cured for 28-d before and after grouting at a temperature of 23°C and relative humidity of 60%. To prevent premature crushing of the FRP in the grips, hollow steel tubing with an inside diameter of 50.8 mm was grouted along 203.2 mm of the bar. Grouting of the steel tubing was performed using high-strength non-shrink grout cured for 20 days.
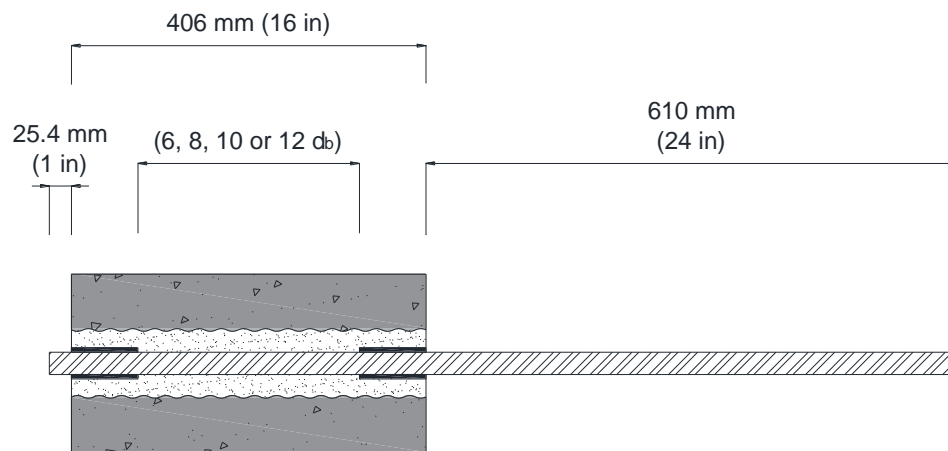
Figure 3.3: Dimensions of test specimens

3.2.3   Test Setup and Procedure

The experimental test setup is exhibited in

Figure 3.4**Figure 3.4.** To verify repeatability of results, two identical specimens were tested for each set of parameters. After curing, specimens were placed atop the active pulling end of an open-loop Tinius Olsen testing machine with a maximum capacity of 530 kN. The strains in the bar were measured by a strange gauge placed amid the distance between the heads of the testing machine. The slip of the bar at the loaded and unloaded ends was measured using two strain-based linear variable displacement transducers (LVDT). The reading of the LVDT at the loaded end was corrected by subtracting the elongation of the bar along the length L as shown in **Figure 3.4.** Rebar pull-out tests in concrete have long been a simple and economical methodology to compare the bond of anchored bars (Steuck et al. 2009; Raynor et al. 2002; Matsumoto et al. 2008; Achillides

& Pilakoutas 2004), yet it is still a subject of contention among investigators, primarily because of the induced compression at the boundary conditions of the specimen. This imposes additional confinement, which artificially enhances the bond. Such induced compression was mitigated in the present study by de-bonding the bars near the loaded end of the specimen, which reduced the intensity of the compressive field on the anchored region. Additionally, a 215.9 mm x 215.9 mm x 25.4 mm hollow steel cradle with a 152.4 mm x 152.4 mm opening was used, which limited the contact area to 25.4 mm along the perimeter of the specimen (5 d_b away from the centre-line of the bar). Darwin & Zavaregh (1996) performed pull-out tests with the edge of the bearing plate 4.5 and 12 d_b from the centre of the test bar and found no significant difference in confinement. For this reason, the hollow steel cradle was thought to be sufficient in mitigating the artefacts of the end conditions.
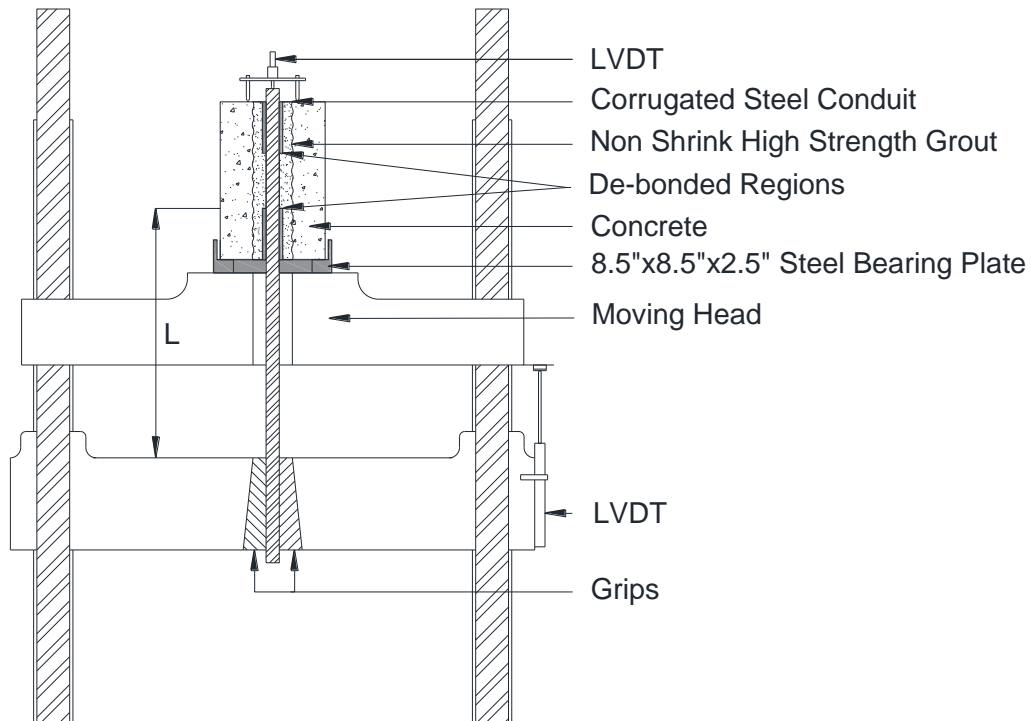
Figure 3.4: Test setup

The bar was extended to the lower plate and gripped by two steel jaws over a length of 165.1 mm. The tensile load was applied monotonically at a rate of 60 MPa/min. A data

acquisition system recorded the test readings at a rate of 10 readings per second. Specimens were labelled as follows: the first two characters represent the type of grout used (NS for non-shrink), followed by a numeral that represents the embedment length (6, 10, and 12 d_b), followed by a letter indicating the bar type (B for basalt, D for deformed, G for glass, and X for high strength steel), followed by a number representing the specimen designation in its group (1 and 2). To differentiate non-ducted specimens, they were designated by ND. For example, NS-12-D2 refers to a deformed bar specimen with an embedment length equal to 12 times the bar diameter.

3.3   EXPERIMENTAL RESULTS

The test was stopped when a pull-out failure (defined as rigid body displacement of the bar equal to the spacing between two successive ribs) or bar fracture was observed. The bar stress, f_{max}, was calculated based on the nominal area. Two specimens were tested for each set of parameters to verify repeatability of the results. The average of the two measured responses was used for analysis purposes unless otherwise mentioned. The assumption of uniform bond stress along the length of an embedded bar is not accurate, specifically when the embedment is longer than (3-7 d_b) (Tastani & Pantazopoulou 2013). The distribution of bond stresses along the embedded length peaks close to the loaded end of the bar and attenuates non-linearly towards the passive end. The exact distribution of the bond stresses along the embedded length of a bar cannot be determined without extensive instrumentation. For this reason, several researchers often find it practical to resort to this simplification (Steuck et al. 2009; Einea et al. 1995; Ganesan et al. 2014; Ashtiani et al. 2013; Tastani & Pantazopoulou 2010; El Refai et al. 2015; El-Hacha et al. 2006; Marchand et al. 2015). It is also relevant to highlight that this assumption is supported by ACI Committee 408R-03 which states "…it is both convenient and realistic for design purposes to treat bond forces as if they were uniform over the anchored, developed, or spliced length of the reinforcement." (ACI Committee 408 2003). It should be noted that the assumption of uniform bond stress is just used in this study to provide a basis for comparison between the different specimens, and does not imply, by any means that such a distribution is realistic. Accordingly, the average bond stress U is calculated as the force along the embedded length per unit surface area of the bar as follows (**Eq. 3.1**),

$$U = \frac{F}{\pi \, d \, L_d}$$

(3.1)

where F = tensile load; d = nominal bar diameter; and L_d = bar embedment length:

3.3.1   Failure Modes

The experimental results are reported in **Table 3.5**. Typical failure of representative specimens is portrayed in **Figure 3.5**. At the end of each test, grouted specimens were split to visually assess the conditions of the bar and the surrounding concrete. The profiles of representative failed bars are further shown in **Figure 3.6**. Ducted specimens equipped with Grade 60 rebar embedded at 6, 8 and $10d_b$ failed in a pull-through mode by crushing of the grout keys between successive ribs (**Figure 3.6**). Grade 100 bars anchored at $6d_b$ and $12d_b$ showed a similar response. Grade 60 bars embedded at $12d_b$ failed by bar fracture. Specimens grouted with ductile bars did not suffer splitting failures at any loading stage. The concrete block did not exhibit cracking during the test, except for NS-12-X1 and X2, where some hairline cracking was observed on the exterior of the concrete prism. These cracks did not appear to influence the overall behaviour since they initiated when the specimen approached the 400 kN mark. At this load level, it is likely for specimens to experience some cracking in the absence of transverse reinforcement.

Figure 3.5: [Top Left] Splitting failures in ductless Grade 60 at 12 d_b (NS-12-D1-ND); [Top Right] Splitting cracks between duct and concrete block (NS-12-G1); [Bottom Left] Duct pull-out (NS-12-G2); [Bottom Right] Failed cones between duct ribs (NS-12-G2).

Table 3.5: Test results

[1] Specimen Tag	Failure Type	$U_{av\ max}$ (MPa)	F_{max} (kN)	f_{max} (MPa)	ε_{max}	SF_{maxU} (mm)	SL_{maxU} (mm)	ε_{maxU}	U_{res} (MPa)	$U_{max\ BPE}$ (MPa)	α	P
'NS-6-D1'	'Pull-out'	22.38	272.12	537.03	0.102	0.89	3.69	0.098	21.97	22.16	0.15	0.05
'NS-6-D2'	'Pull-out'	21.73	264.31	521.61	0.086	0.94	2.94	0.078	20.00	21.70	0.11	0.05
'NS-8-D1'	'Pull-out'	17.64	286.10	564.63	0.170	0.66	6.03	0.160	15.65	17.50	0.14	0.06
'NS-8-D2'	'Pull-out'	17.75	287.76	567.89	0.159	0.66	1.90	0.153	15.84	17.69	0.13	0.08
'NS-10-D1'	'Pull-out'	14.08	285.30	563.05	0.177	0.56	6.15	0.163	13.71	13.76	0.15	0.08
'NS-10-D2'	'Pull-out'	14.47	293.38	578.98	0.192	0.73	6.93	0.183	13.66	14.43	0.07	0.07
'NS-12-D1'	'Bar Fracture'	12.18	296.31	584.78	0.277	0.06	8.39	0.220	12.18	-	-	-
'NS-12-D2'	'Bar Fracture'	12.20	296.64	585.42	0.267	0.06	7.73	0.202	12.20	-	-	-
'NS-12-D1-ND'	'Grout Splitting'	10.60	257.70	508.58	0.064	0.42	2.33	0.061	-	10.58	0.21	0.39
'NS-12-D2-ND'	'Grout Splitting'	09.46	230.20	454.31	0.040	0.63	1.51	0.040	-	9.46	0.26	0.71
'NS-6-G1'	'Pull-out'	17.98	232.30	406.03	0.007	0.24	3.40	0.007	3.98	17.59	0.29	0.02
'NS-6-G2'	'Pull-out'	18.92	244.52	427.39	0.007	0.41	3.48	0.007	7.74	18.77	0.14	0.05
'NS-12-G1'	'Pull-out'	13.41	346.50	605.63	0.009	0.24	3.87	0.009	3.87	13.34	0.21	0.01
'NS-12-G2'	'Duct pull-out'	13.59	351.10	613.67	0.009	0.49	2.98	0.009	5.42	13.55	0.23	0.04
'NS-6-B1'	'Pull-out'	16.57	198.30	403.97	0.006	3.49	2.85	0.006	15.56	16.51	0.10	0.07
'NS-6-B2'	'Pull-out'	14.19	169.90	346.12	0.007	0.80	2.84	0.006	13.37	13.68	0.09	0.12
'NS-12-B1'	'Pull-out'	10.74	257.00	523.56	0.010	0.78	4.35	0.010	4.10	10.50	0.06	0.06
'NS-12-B2'	'Pull-out'	10.89	260.68	531.04	0.011	3.35	3.01	0.010	8.07	10.80	0.04	0.13
'NS-6-X1'	'Pull-out'	21.21	257.90	508.97	0.033	0.64	0.82	0.022	18.07	19.50	0.27	0.04
'NS-6-X2'	'Pull-out'	23.14	281.40	555.35	0.030	0.58	0.72	0.019	19.77	21.03	0.34	0.06
'NS-12-X1'	'Pull-out'	17.27	420.10	829.08	0.046	0.30	1.26	0.033	15.18	16.81	0.28	0.03
'NS-12-X2'	'Pull-out'	18.56	451.30	890.65	0.054	0.36	1.67	0.044	12.98	18.45	0.19	0.04

Note: F_{max} = ultimate load; f = peak stress in bar; $U_{av\ max}$ = bond strength; ε_{max} = peak strain in bar; SF_{maxU} = slip corresponding to maximum bond stress at the free end; SL_{maxU} = slip corresponding to maximum bond stress at the loaded end; ε_{maxU} = strain corresponding to maximum bond stress; U_{res} = Residual bond strength; $U_{max\ BPE}$ = analytical bond strength; α and p = model fitting parameters

[1] **NS** *refer to Non-Shrink grout;* **6, 8, 10, and 12** *refer to the bar anchored length, respectively;* **D, G, B and X** *refer to Grade 60 rebars, GFRP bars, BFRP bars, Grade 100, respectively;* **ND** *refer to Non-Ducted specimens*
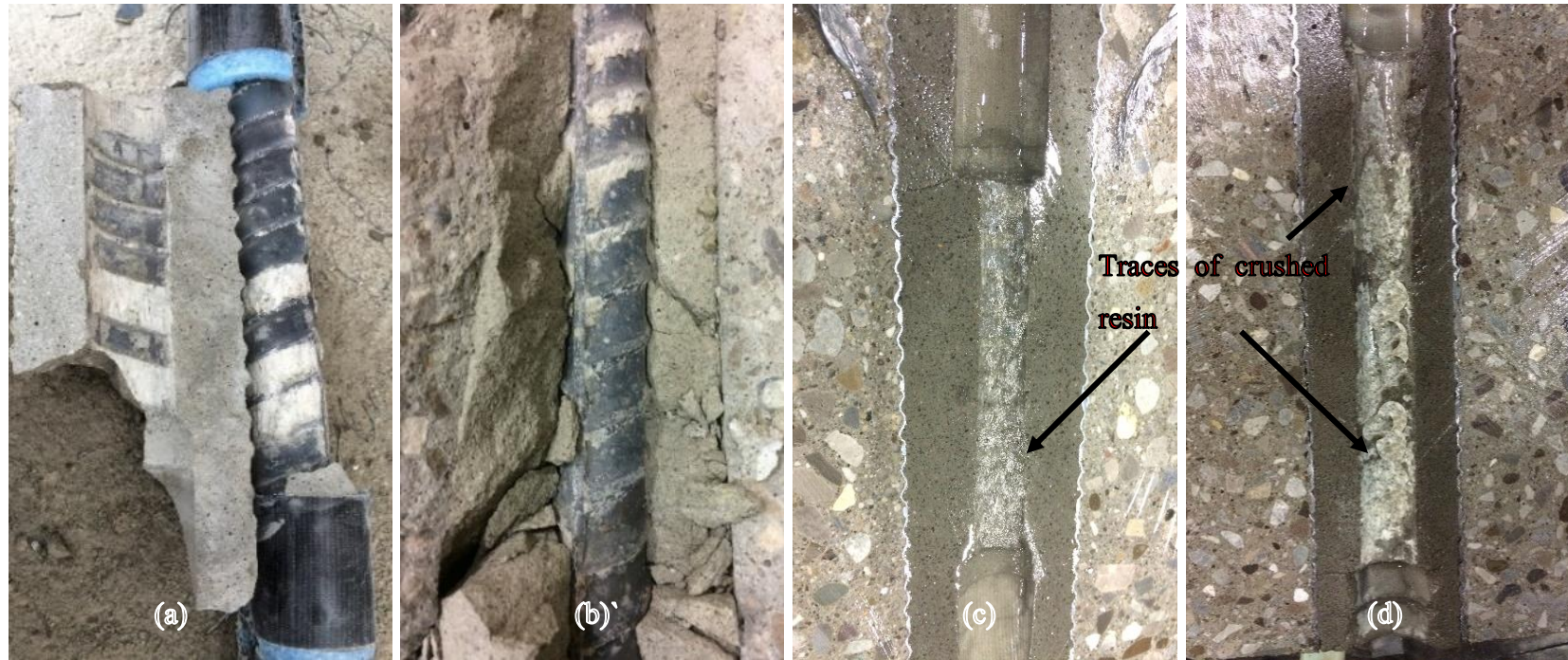
Figure 3.6: Profile of failed bars; [LEFT to RIGHT] a) Crushing of grout keys (NS-6-D1); b) Cracked cones inside a ductless grout cylinder (NS-12-D2-ND); c) Damage localization near the loaded end of BFRP bars (NS-6-B2); and (d) Interfacial damage along the anchored length (NS-12-G1).

All BFRP and GFRP specimens failed by bar pull-out, except for NS-12-G2, which failed by duct pull-out in a very brittle mode, as shown in **Figure 3.5**. Although the pull-out of FRP bars was similar to that of their ductile counterparts (no cracking in the grout cylinder was observed), a difference in their failure mechanisms was observed. All FRP specimens had a splitting crack that propagated radially from the duct until it reached the exterior of the block. These cracks had varying intensity and propagated as the load approached the recorded peak of the specimen. BFRP bar specimens had finer cracks than that suffered by specimens having GFRP bars. While these splitting cracks were due to insufficient concrete cover, their absence in specimens with ductile bars suggests that grouted FRP bars behaved differently. This can be further explained by examining **Figure 3.6** where traces of crushed resin (white residue) can be observed along the anchored length, indicating that the shear capacity of the interfacial layer (between the bar core and the exterior layer) was exceeded. For BFRP bars, these traces appear to be more localized near the loaded end, although resin traces were still visible along the embedment. GFRP bars had similar white traces as their BFRP counterparts, except that such traces appear to be more distributed over the anchored length. The presence of these traces with sand coated GFRP bars indicates that bond failure took place along the full anchored length. Similar observations were also reported by El Refai et al. (2015) and Davalos et al. (2008). This further explains the splitting cracks suffered in all specimens with FRP bar. The uniform load distribution along the entire anchored length resulted in the corrugated duct, enclosed grout, and FRP bar behaving as a single large diameter bar embedded in concrete. With such a large diameter bar, the low cover-to-diameter ratio (0.83) made the specimens more susceptible to splitting failures. The duct pull-out type failure of specimen NS-12-G2 is a magnified manifestation of this phenomenon.

It should be noted that, unlike non-ducted specimens where grout splitting/expansion dominated the failure as shown in **Figure 3.5** and **Figure 3.6**, the grout enclosed by the corrugated duct in all ducted specimens did not incur cracking, irrespective of the bar type or anchored length. In the case of non-ducted specimens, the absence of failure cones close to the loaded specimen end suggests that disengagement of the ribs occurred during earlier stages of the loading, which was accompanied by severe cracking as the grout around the

bar was dilatated. Consequently, the load was redistributed over the remainder of the length. This is evident from the shear cones present on the profile of the bar close to the unloaded end (**Figure 3.6**). Typical failure of the non-ducted specimens highlights the effectiveness of the corrugated duct in providing uniform restraining action along the anchored length.

3.3.2   Load/Strain vs Slip
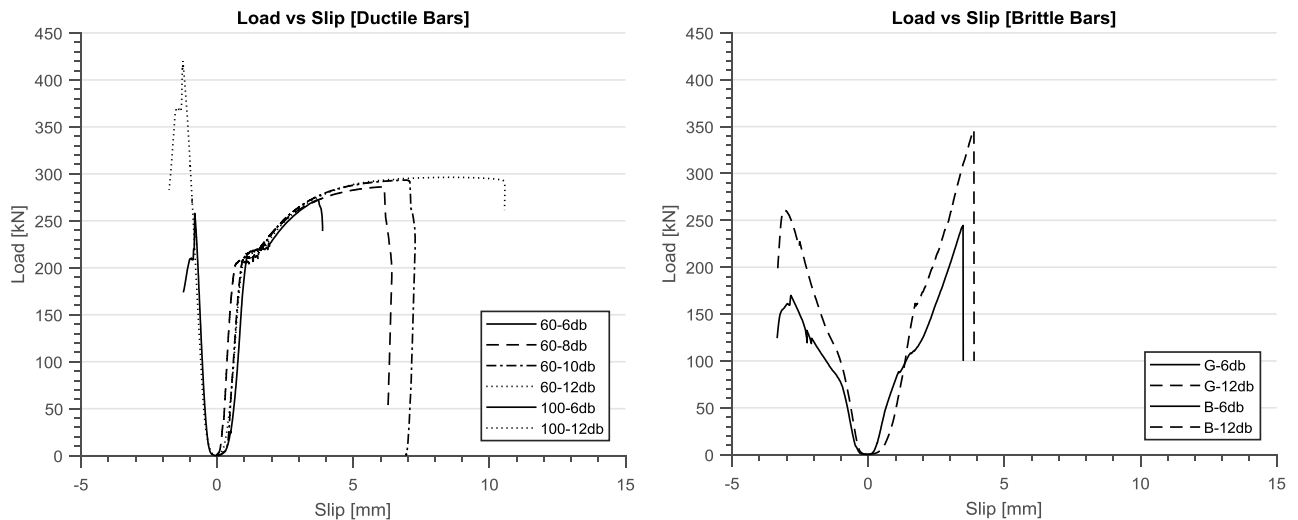
Figure 3.7: Load vs loaded end slip envelopes (representative specimens): [Left] Ductile bars (negative abscissa represents Grade 100); [Right] Brittle Bars (negative abscissa represents BFRP).

The load versus slip response of the tested specimens is illustrated in **Figure 3.7** (bars plotted on the negative abscissa represent a different bar material). Additionally, the ultimate load at different embedment lengths is plotted in **Figure 3.9**. As previously discussed, this test setup is prone to inducing artificial compression, which can enhance the bond of the test specimen. Although a compressive field was introduced unto the specimens with varying embedment, the failure was consistent among the specimens with an embedment length of 6, 8 and 10 d_b. It should be noted that, the magnitude of the induced compressive field increases with an increase in embedment due to the reduction of the de-bonded lengths close to the loaded end.
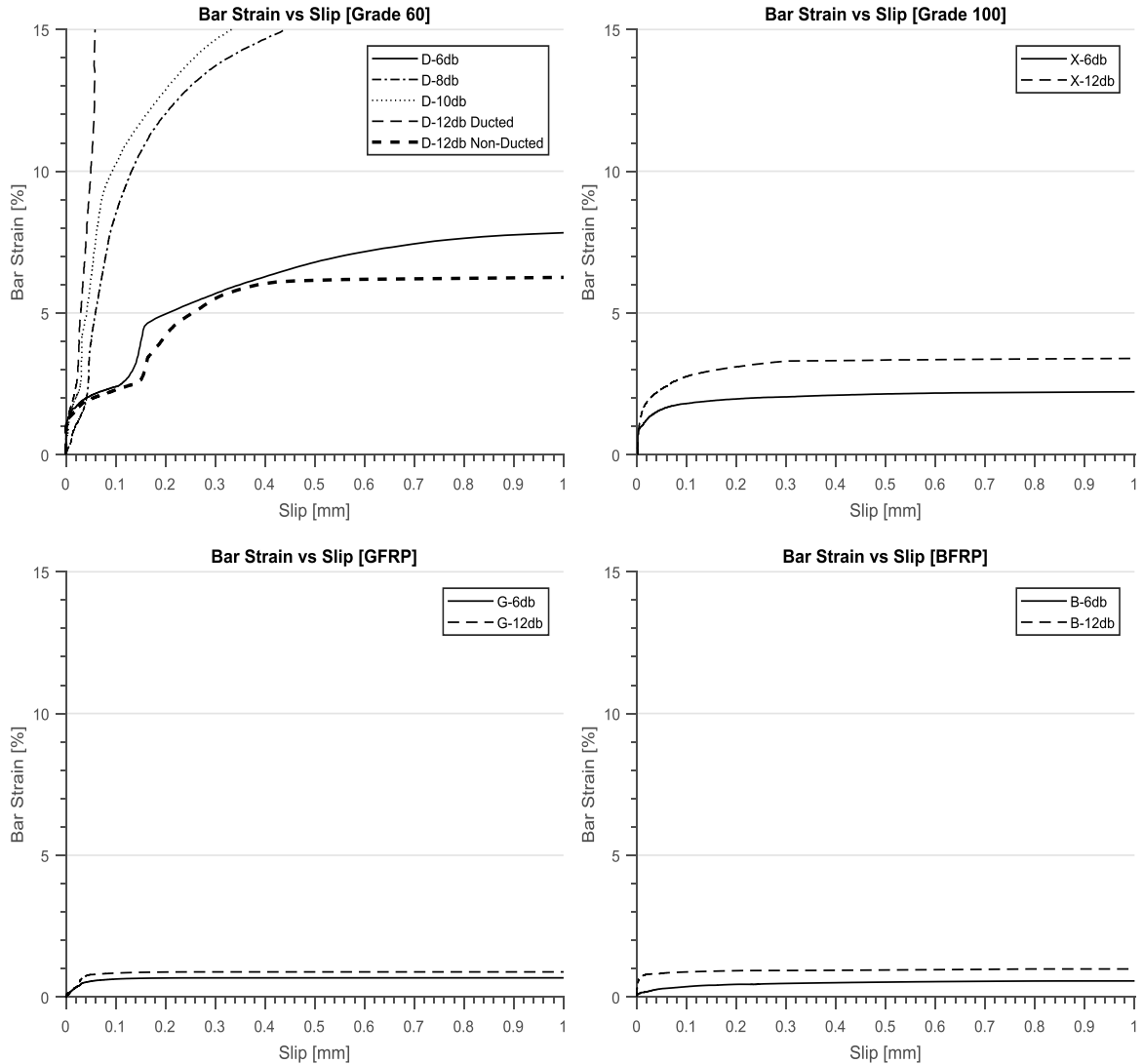
Figure 3.8: Strain vs free end slip at different embedment length.

However, given that the specimens at 8 and 10 d_b failed by shearing of the grout keys at an average load of 286.93 and 289.34 kN, respectively, it is believed that the magnitude of this compressive field did not significantly influence the results. The response of Grade 60 bars was identical up to the average yielding point of the bars (~220 kN). Grade 60 bars achieved an average load carrying capacity of 296.47 kN at 12 d_b. Considering that the bar was exposed to loads exceeding the measured yield stress, it appears that the length of the anchorage marginally affects the load carrying capacity of the connection. The length of the anchorage, however, significantly affected the slippage of the bars. A significant increase in slip was observed as the anchored length increased (at 12 d_b bars slipped 2.5

times more than at 6 d_b). The strain-slip relationship for the different bars is plotted in **Figure 3.8** to highlight the effects of yield penetration in invoking additional slippage of the bars. This additional slip is apparent when Grade 60 bars are examined, as indicated in **Figure 3.8**. The level of strain hardening of the bars had a detrimental effect on the corresponding slip domain. This is confirmed by the softening of the curves observed at different slip levels, as observed by Bonacci & Marquez (1994) and Tastani & Pantazopoulou (2013), where cracking in the shorter direction initiated after the yielding of the bar, indicating that cracking of the matrix is expected with such strain penetrations. Yet, grouted connections did not incur cracking resulting from similar strain levels. Further comparisons with data in the open literature was not possible due to the scarcity of information pertaining to bond in grouted connections, particularly that the scant relevant data published focused on shorter embedment lengths (bar remained elastic).
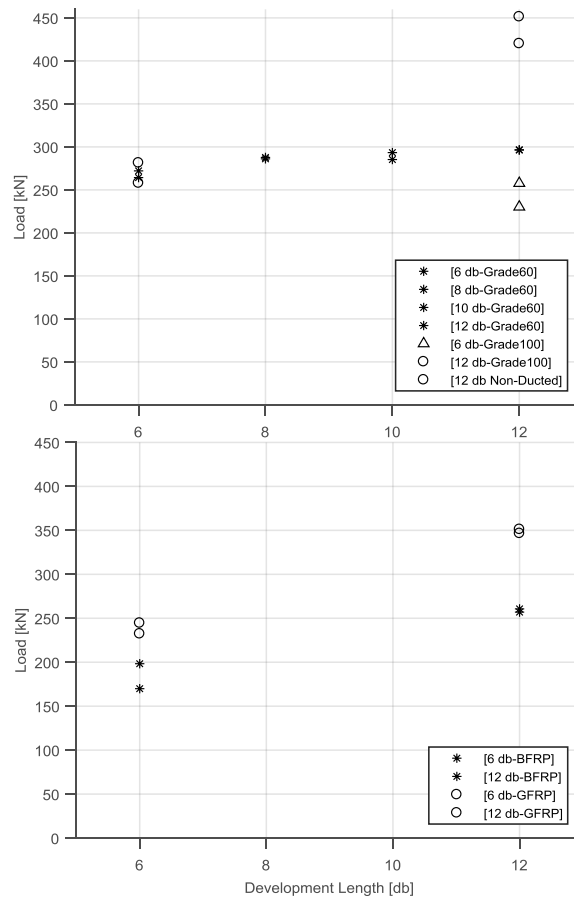
Figure 3.9: Ultimate load vs embedment length: [Top] ductile bars; [Bottom] brittle bars.

The difference between the performance of specimens made with Grade 60 and Grade 100 bars are illustrated in **Figure 3.7**. For the same load level, Grade 60 bars at 6 and 12 d_b slipped 2 and 8 times more than their Grade 100 counterparts, respectively. This was primarily due to the yielding of grade 60 bars. Plasticity of the bars forces the cross-section to contract, thus disengaging the lugs close to the loaded end due to Poisson's effect. This phenomenon is not expected when Grade 100 bars are considered because the longitudinal strains are within the elastic range. Given that both bars failed by shearing of the grout keys, Grade 60 bars required an appreciable amount of displacement to reach similar load level to that of Grade 100 bars. This is significant because grouted connections are often used as ductile devices designed to yield in tension. Since the design of yielding anchorages is associated with displacements, requiring more displacement to develop the bar (and mobilize fracture) is desirable, so long as this additional displacement is not due to splitting. For rational comparison of the slip domains over which the maximum load occurred, the slip of each specimen was normalized by the loaded end slip corresponding to the maximum bond stress recorded (**Table 3.5**: SL_{maxU}). **Figure 3.10** exhibits this relationship, showing the amount of displacement required to mobilize the largest load recorded by the various specimens, where the degree of slip was measured as the slope of the line. The steeper the slope of the line, the more displacement was required to mobilize ductile behaviour. Slopes for specimens with Grade 60 rebar became steeper as the anchored length increased until fracture of the bars was observed (12 d_b).
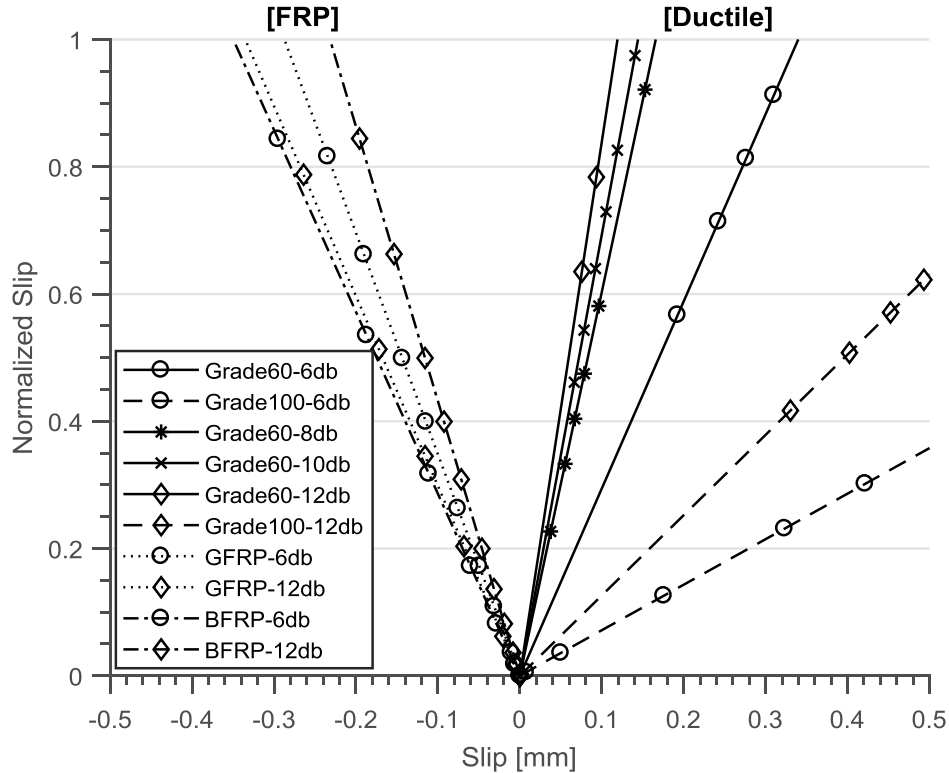
Figure 3.10: Normalized slip vs slip (loaded end) at $6d_b$ and $12d_b$ for various bars (Grade 60 at $8d_b$ and $10d_b$ are also shown).

The responses of specimens made with GFRP and BFRP bars were similar to that of specimens having Grade 100 bars (increase in anchorage results in an increase in load, but not slip). It showed similar ascending branch for each type of bar regardless of the embedment length. An almost linear increase in load carrying capacity was accompanied by a corresponding increase in slip till bars failed by pull-out. However, FRP bars experienced local slippage along the tubing length (used for gripping) at several locations along the response as characterized by sudden change in slope (**Figure 3.7**). GFRP bars had 29.5 and 34.5% higher in load carrying capacity than its BFRP counterparts at 6 and 12 d_b, respectively. This was attributed to the larger GFRP bars diameter since for a given embedment length, larger bars require more force per unit surface area to initiate slip (ACI Committee 408 2003). However, both bars recorded low strain values (>1%). Slip at the unloaded end was not initiated until later during the test, after which failure suddenly occurred as the bond generated by the anchorage was exhausted. It can be observed in

Figure 3.10 that both BFRP and GFRP bars developed their maximum loads over a comparable slip domain, despite the 30% higher load level resisted by the GFRP.

3.3.3   Bond Stress-Slip Response

Representative bond stress-vs-slip response for specimens tested in this study is shown in **Figure 3.11**. There are two distinctive branches: one where a gradual increase in bond stress is accompanied by minor increase in slip values until a maximum bond stress is attained (ascending branch); and a second branch where a decrease in bond stress is accompanied by significant increase in slip values (softening branch). Between these two branches and depending on the type of rebar and its geometry, a region where the maximum bond stress is constant exists. The general bond behaviour is characterized by three main branches: i) elastic response (ascending branch) valid for $0 < S < S_1$; ii) As the maximum bond stress is attained, plastification of bond is assumed to occur in the region bound between S_1 and S_2. If splitting cracks are restricted, and depending on the anchorage length, the specimen can exhibit a plateau; and iii) Loading beyond S_2 and up to S_3 results in deboning and progressive detachment of the engaged ribs. The resulting slope depends primarily on the confinement and its subsequent effect on the coefficient of friction.
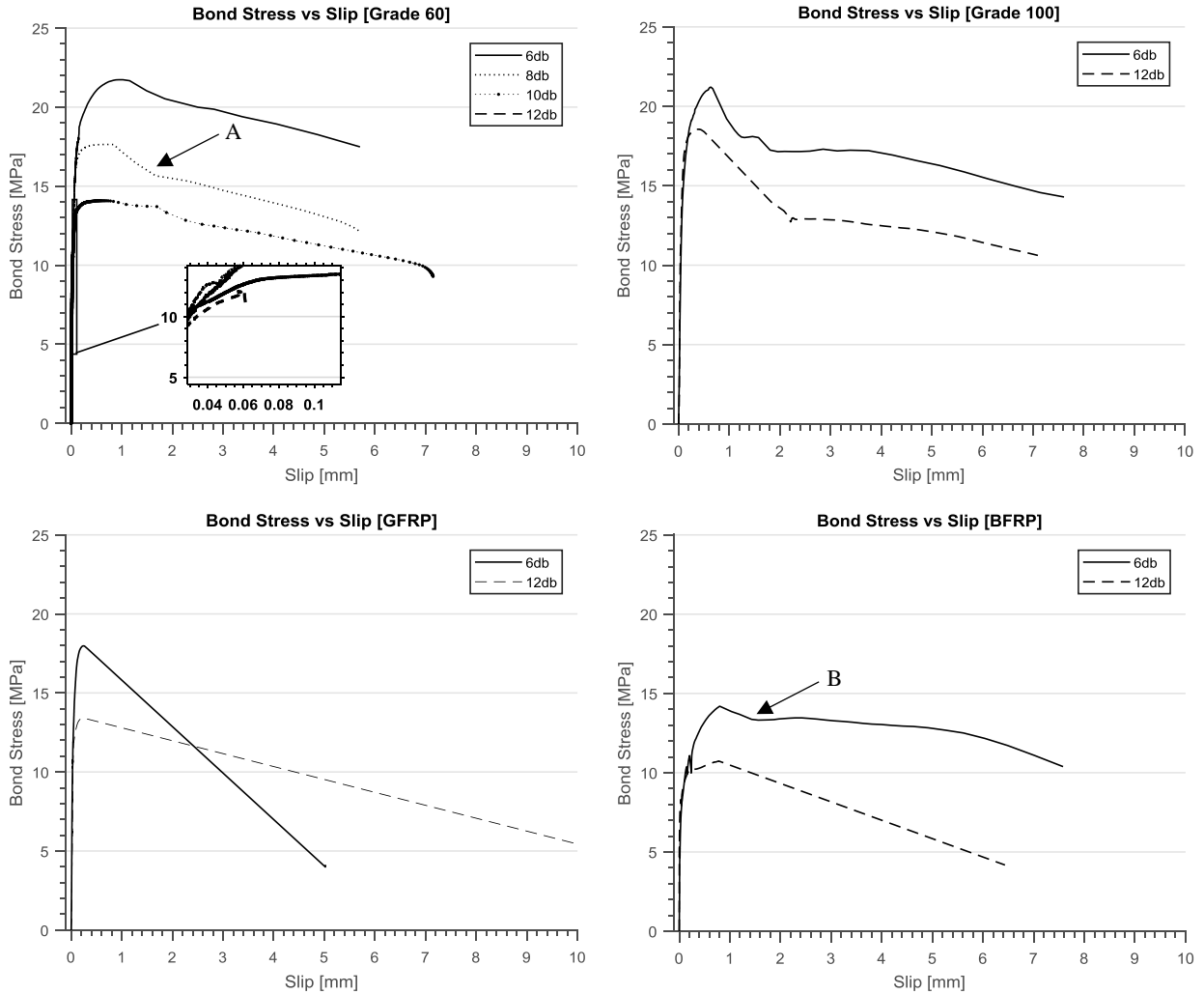
Figure 3.11: Bond stress vs free end slip envelopes of grouted specimens for different bars tested.

Bond-slip curves of the tested ductile metallic bars had similar overall trend to that discussed above. Grade 60 and 100 bars embedded at $6d_b$ achieved a comparable average bond stress of 22 MPa. This was expected since both bars had similar relative rib areas. However, this behaviour changed when the embedment length increased from 6 to 12 d_b, where Grade 60 bars achieved an average bond stress of 12.19 MPa, which is 31.9% less than those of their Grade 100 counterparts. Two different mechanisms of bond are observed and can be explained considering the classical equilibrium requirement of the stresses at an anchored zone as described by **Eq. 3.2**:

$$U_{av} = \frac{E\varepsilon d_b}{4\,L_d} \tag{3.2}$$

Where: U_{av} = average bond stress; E = elastic modulus of the bar; ε = strain in the bar; d_b = diameter of bar; L_d = development length.

In the case of Grade 100 rebar, the increase in embedment length (from 6 to 12 d_b) was accompanied by a corresponding increase in elastic strain in the bar. This explains the similarity between the bond stress estimates at both embedment lengths. If the bars are pulled beyond their elastic limit, as in the case of Grade 60 bars, the increase in embedment length further brings about significant increase in slip. If a medium or long anchorage length (non-uniform distribution) is provided, the bond stresses are redistributed over the remainder of the anchorage towards the free end as it utilizes the anchorage reserves. This can be observed in **Figure 3.11** where the length over which the maximum bond stress plateaus, which increases with the increase in embedment.

Theoretically, a limit of L_d exists where an increase in the anchored length does not result in a corresponding increase in the average load carrying capacity. This can be observed from the trend of Grade 60 bars at different embedment lengths, where the estimated maximum average bond stress and the increase in embedment length were inversely proportional. In the present study, the above stated limit appears to be between 10 and 12 d_b since a shift in the failure mode between 10 and 12 d_b was observed. Bonacci (1994) reported similar observations when the anchorage length fell between 11 to 12 d_b, highlighting that the change between acceptable and non-acceptable anchorage occurs rather abruptly.

Specimens with FRP bars behaved differently from their counterparts made with ductile bars. Beyond the maximum bond stress, sudden drop in bond stress along the failing branch was observed. This was due to the different nature of transmitting bond forces along the length of an embedded FRP bars since they transmit bond through chemical adhesion and frictional stresses between the outermost layers of the bars and concrete. This explains the higher bond stresses achieved by sand coated GFRP bars regardless of their embedment

length. GFRP bars achieved an average bond strength of 20.25 and 13.49 MPa at 6 d_b and 12 d_b, respectively, which compares to the maximum average bond stress of ductile metallic bars, despite their sole reliance on frictional aspects of the interface.

BFRP bars did not have a sand coated layer (**Figure 3.2**), but rather uniform indentations along their entire length. At 6 d_b embedment length, BFRP bars achieved a bond strength of 15.38 MPa, 16.6 % less than that of their GFRP counterparts. This was primarily due to the smoother surface of the bars, although some mechanical bearing is expected due to their surface geometry.

3.3.4   Residual Bond Stress

To further assess frictional resistance along the descending branch, it is important to examine the residual bond stress of the different bars, which describes the post maximum bond stress attained at the end of the descending branch of the response. The residual bond stresses normalized by the maximum average bond stress for different bars were plotted in **Figure 3.12**. This was done by inspection of individual bond stress-slip responses to determine the point on the descending branch where a sudden change in slope (**Figure 3.11** point A) or flattening (**Figure 3.11** point B) of the branch occurred. The corresponding values of bond stress were recorded in **Table 3.5**. Ductile bars had higher residual bond stresses than that of their FRP counterpart due to the engagement of the frictional bond mechanisms after bearing of the ribs was exhausted, which is likely magnified due to the confinement effect of the duct and its subsequent effect on the coefficient of friction at the interface between the bar and the concrete. GFRP specimens had the lowest increase since they relied primarily on friction to transmit bond stress. Once the shear capacity of the interface was exhausted, the bars slipped abruptly. The flowing consistency of the grout is thought to have enhanced the bar-grout interfacial characteristics, which was reflected in higher load capacity of specimens (**Figure 3.7**).
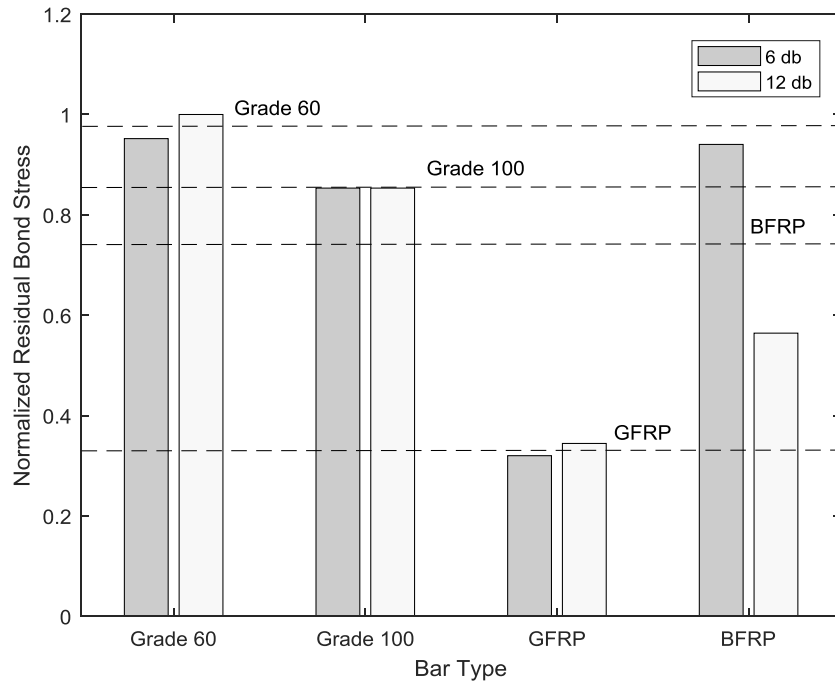
Figure 3.12: Normalized residual bond stress (dotted line represents the average).

3.3.5　Duct Confinement

To highlight the confining mechanism in grouted connections, two ductless specimens under identical conditions were tested. The bond stress versus unloaded end slip response of the NS-12-D1 and NS-12-D2-ND specimens is shown in **Figure 3.13**. Ducted specimens achieved a maximum average bond strength of 12.18 MPa, while the non-ducted specimens achieved an average bond strength of 10.03 MPa. The free end slip reflects the damage incurred by the non-ducted specimens, given that the ducted specimens experienced almost no slip, indicating that the anchorage reserve was progressively engaged. The free end slip of ductless specimens was at least 10 times more than that in their ducted counterparts. The ascending branch stiffness of both envelopes was comparable up to a bond stress of 3 MPa, after which a reduction in stiffness was observed. It is believed that, at this low bond stress, the onset of bond plastification of the non-ducted specimens was initiated. The increase in the slip rate was accompanied by an increase in strain as more of the anchorage reserves was utilized. Another plateau was observed as the bars yielded, causing significant yield penetration. The specimen failed by bar pull-out

shortly thereafter. This failure was characterized by large splitting cracks emanating from the inside of the bar, penetrating the grout cylinder radially, and propagating through the concrete block, as shown in **Figure 3.5**. Four features underscore the effect of the duct confinement: i) Consistently higher bond stress values were observed for the ducted specimens. The slip corresponding to the bond strength of the ducted specimens was one order of magnitude lower than that of their ductless counterparts (**Table 3.5**; **Figure 3.13**); ii) Enhanced ductility of the response as cracks were neither observed in the specimen within the grout cylinder bound by the duct, nor on the concrete block. Conversely, the absence of the duct resulted in severe cracking towards the loaded end of the ductless specimen, which occurred earlier during the test. This is visible from the reduced stiffness as discussed earlier (**Figure 3.13**), and the absence of the failed shear cones towards the loaded end (**Figure 3.6**); iii) Difference in failure modes as observed in **Figure 3.13** where sudden failure was a result of bar fracture in the case of ducted specimens with an anchored length of $12d_b$, while brittle pull-out accompanied by splitting characterised failure for the ductless specimens; and iv) the curve fitting parameter α (discussed hereunder) consistently had lower values for grouted specimens, implying more confinement.
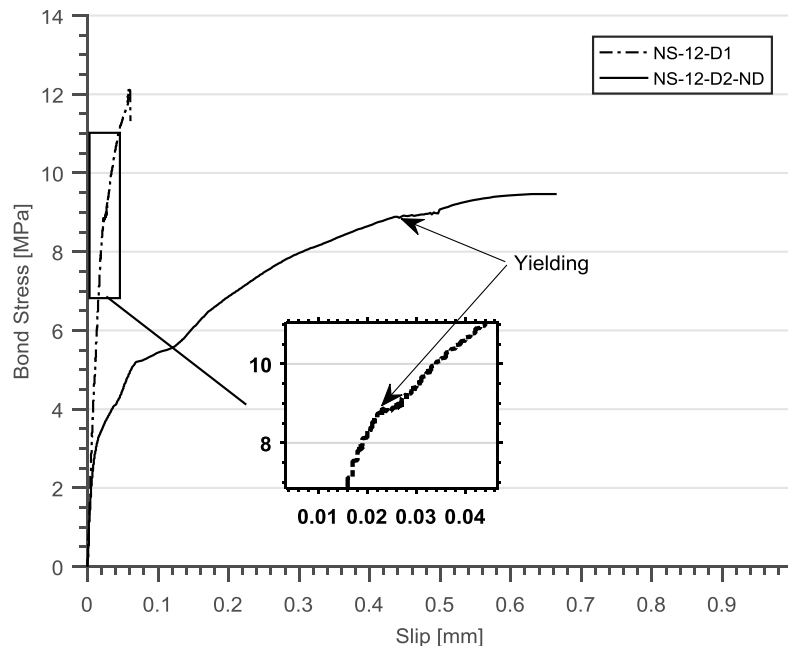
Figure 3.13: Comparison between the behaviour of ducted and non-ducted specimens at $12\ d_b$.

3.4 ANALYTICAL MODELLING

Two constitutive bond-slip laws were considered in this study. The Elighausen, Popov and Bertero (BPE) model presented by Eligehausen et al. (1982) was used to describe the behaviour of ductile bars. The modified BPE (mBPE) proposed by Cosenza et al. (1997) was used to capture the behaviour of FRP bars. **Figure 3.14** depicts these two models. The experimental results from pull-out tests (**Table 3.5**) were used to calibrate these models for the respective bar types. The ascending branch ($s \leq s_1$) of both models is essentially identical and can be expressed by **Eq. 3.3** as follows:

$$\frac{\tau}{\tau_{max}} = \left(\frac{s}{s_{max}}\right)^{\alpha} \tag{3.3}$$

Where τ and s are the corresponding bond stress and slip at a given loading increment; τ_{max} and s_{max} are the maximum recorded average bond stress and slip, respectively; and α is a model fitting parameter.
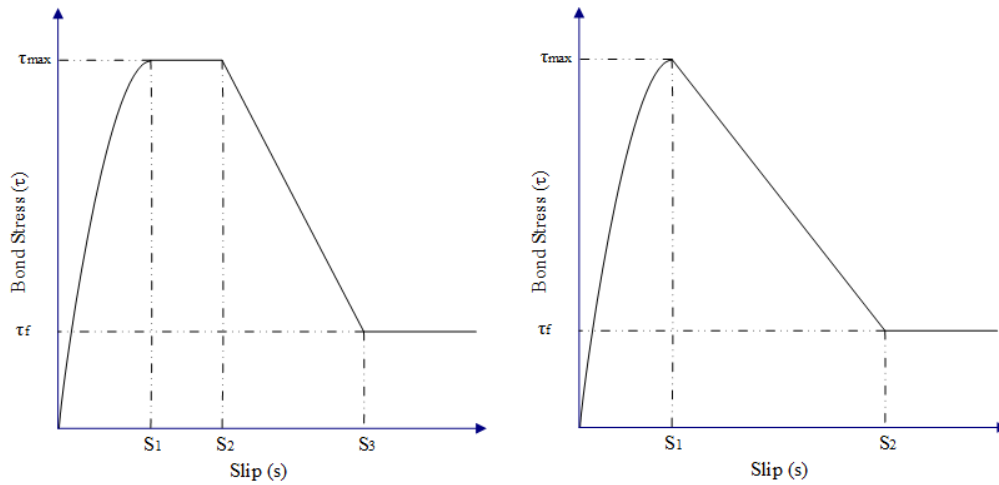
Figure 3.14: Bond-slip law: [Left] BPE; and [Right] mBPE.

According to the CEB-FIP (2010), which adopts the BPE model to explain the bond stress of bars, the model parameter α reflects the degree of stiffness of the ascending branch and should have values between 0 and 1. Per the same standard, the recommended value of parameter α for confined concrete is 0.4. The closer the value of α to zero, the more it is

indicative of a stiffer ascending branch of the response. To calibrate α, **Eq. 3.4** is solved by integrating the ascending branch of the experimental data, allowing an estimation of α.

$$A_\tau = \int_0^{s_1} \tau(s)\, ds = \tau_{max} \left(\frac{s}{s_{max}}\right)^\alpha ds \tag{3.4}$$

Where A_τ is the area underneath the ascending branch of each specimen. The BPE model describes a branch where the bond strength plateaus ($s_1 < s < s_2$), which is expressed by **Eq. 3.5**:

$$\tau = \tau_{max} \tag{3.5}$$

As observed in **Figure 3.14,** the mBPE model accounts for the unique behaviour of the FRP bond (by eliminating this branch). This was supported by applying the classical BPE model to experimental data, which showed a lack of this second branch when the bond of FRP bars was considered Cosenza et al. (1997). This was also observed in the experimental results discussed earlier.

The failing branch of the BPE model, ($s_2 < s < s_3$) calls for a linearly descending branch up until $\tau = \tau_f$, after which a horizontal branch that expresses the frictional resistance of the envelope when ($s > s_3$). Values of s_2, s_3, and τ_f are based on the experimental data. The descending branch of the mBPE ($s_1 < s < s_2$) is given by **Eq. 3.6** as presented by Cosenza *et al.* (Cosenza et al. 1997):

$$\frac{\tau}{\tau_{max}} = 1 - P\left(\frac{s}{s_1} - 1\right) \tag{3.6}$$

Where P is the slope of the descending branch from (s_1, τ_{max}) to (s_2, τ_f). Beyond this descending branch, ($s > s_2$), the mBPE was identical to the BPE model.

The calculated parameters (α and P) are shown in **Table 3.5**, while the mean values, standard deviations, and coefficients of variation of calibrated model parameters are listed in **Table 3.6**. Ducted specimens with Grade 60 bars had a mean calibrated parameter α of 0.1255, approximately 50% less than that of their ductless counterparts, which should be

considered in view of the very different failure modes of both types of specimens which indicated the superior ductility provided by of the confinement action of the duct. Specimens with Grade 100 bars and GFRP bars had comparable α values. Specimens with BFRP bar had the lowest calculated values of α, which is consistent with the finding of El Refai et al. (2015). The descending branch slope, P, for GFRP specimens was slightly higher than that of specimens with BFRP bars, though a sharper and more sudden decrease in bond was observed for GFRP bars. This can possibly be attributed to the larger scatter in the data as indicated by the high coefficient of variation observed for GFRP bars. Comparison between the experimental and the predicted envelopes are shown in **Figure 3.15**. The predicted values appear to be in good agreement with the experimental results. The mBPE model appears to render the experimental behaviour of FRP bars accurately.

Table 3.6: Mean, standard deviation, and coefficient of variation of calibrated parameters

	Ductile			**FRP**			
	Grade 60		Grade 100	BFRP		GFRP	
Parameter	Ducted	No Duct					
	α_{BPE}			α_{BPE}	P_{mBPE}	α_{BPE}	P_{mBPE}
Mean	0.1255	0.2376	0.2699	0.0737	0.093	0.2165	0.0315
Standard Deviation	0.0320	0.0387	0.0599	0.0233	0.037	0.0599	0.0171
Coeff. of Var.	25.4670	16.2677	22.1887	31.6307	40.007661	27.6800	54.3977
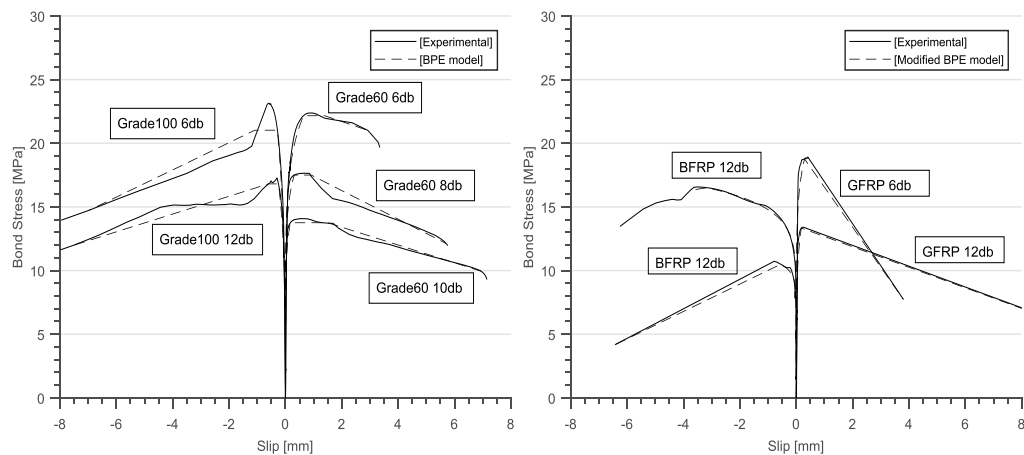
Figure 3.15: Corroboration of the analytical model: [Left] BPE model; [Right] modified BPE model.

3.5   SUMMARY AND CONCLUSIONS

Twenty-two full-scale pull-out test specimens were used to investigate the behaviour of grouted connections used in precast wall construction and the difference in their bond behaviour due to the passive confinement effect of the duct. The test set-up was carefully designed to mimic field grouting conditions. The results provided useful insights into the behaviour of grouted connections under various changing parameters. Based on the experimental and analytical results presented above, the following conclusions can be drawn:

Grouted connections tested experimentally did not suffer splitting failures resulting from expansion in the grout cylinder surrounding the bar, regardless of the different embedment lengths and their subsequently different bond stress. The corrugated duct was able resist the dilatation of the grout. When the duct was absent, brittle failure mechanisms prevailed and cracks propagated from the unloaded end of the bar radially splitting the grout cylinder and the concrete block.

Grouted connection specimens using ductile bars failed by shearing of the grout keys, regardless of the stress level in the bar and the embedment length. Conversely, specimens made with FRP bars incurred shearing failure along the interface of the bar and the surrounding grout. FRP bars achieved a high load carrying capacity despite their surface geometry (mechanical bearing was absent). Specimens with FRP bar had splitting tensile cracks between the corrugated duct and the concrete block, which was more pronounced in the case of GFRP. This is believed to be a direct result of the high frictional bond components due to GFRP's sand blasted surface.

The bar's strain level had a detrimental effect on the magnitude of its recorded slip. Yield penetration seemed to invoke significant slip on deformed bars. However, this was not associated with cracking and deterioration of the assembly. Considerable displacement was required to mobilize the full capacity of the bars at 12 d_b

The BPE and mBPE bond-slip models were calibrated based on the experimental results and produced acceptable estimation of the experimental behaviour. The analytical

envelopes resembled the experimental behaviour accurately. Values of the calibrated model parameter α provided evidence of confinement when compared to those listed in the CEB-FIP model code (**Table 3.6**).

3.6   REFERENCES

Achillides, Z. & Pilakoutas, K., 2004. Bond Behavior of Fiber Reinforced Polymer Bars under Direct Pullout Conditions. *ASCE Journal of Composites for Construction*, 8(2), pp.173–181.

ACI Committee 318, 2014. Building Code Requirements for Structural Concrete and Commentary. *American Concrete Institute, Farmington Hills, MI, USA*, pp.1–519.

ACI Committee 408, 2003. Bond and Development of Straight Reinforcing Bars in Tension. *American Concrete Institute, Farmington Hills, MI, USA,*, pp.1–49.

Ashtiani, M.S., Dhakal, R.P. & Scott, A.N., 2013. Post-yield bond behaviour of deformed bars in high-strength self-compacting concrete. *Construction and Building Materials*, 44, pp.236–248.

ASTM 370, 2014. Standard Test Methods and Definitions for Mechanical Testing of Steel Products. *American Society for Testing and Materials*, 01.03, pp.1–50.

ASTM C39, 2016. Standard Test Method for Compressive Strength of Cylindrical Concrete Specimens. *American Society for Testing and Materials*, 04.02, pp.1–7.

ASTM C496/C496M, 2011. Standard Test Method for Splitting Tensile Strength of Cylindrical Concrete Specimens. *American Society for Testing and Materials*, 04.02, pp.1–5.

Belleri, A. & Riva, P., 2012. Seismic performance and retrofit of precast concrete grouted sleeve connections. *PCI Journal*, (PCI Journal Winter), pp.97–109.

Bonacci, B.J.F., 1994. Bar yield penetration in monotonically loaded anchorages. *ASCE Journal of Strucutral Engineering*, 120(3), pp.965–986.

Bonacci, J. & Marquez, J., 1994. Tests of Yielding Anchorages under Monotonic Loadings. *ASCE Journal of Strucutral Engineering*, 120(3), pp.987–997.

Brenes, F.J., Wood, S.L. & Kreger, M.E., 2006. Anchorage Requirements for Grouted Vertical-Duct Connectors in Precast Bent Cap Systems. In *Texas Department of Transportation Technical Report No. FHWA/TX-06-4176-1*. pp. 1–251.

CEB-FIP, 2010. Model Code 2010. *Federation Internationale du Beton, Lausanne, Switzerland.*, pp.1–292.

Cosenza, E., Manfredi, G. & Realfonzo, R., 1997. Behavior and Modeling of Bond of FRP Rebars to Concrete. *Journal of Composites for Construction*, 1(2), pp.40–51.

Darwin, D. & Zavaregh, S.S., 1996. Bond Strength of Grouted Reinforcing Bars. *ACI Structural Journal*, 93(4), pp.486–495.

Davalos, J.F., Chen, Y. & Ray, I., 2008. Effect of FRP bar degradation on interface bond with high strength concrete. *Cement and Concrete Composites*, 30(8), pp.722–730.

Einea, A., Yamane, T. & Tadros, M.K., 1995. Grout-Filled Pipe Splices for Precast Concrete Construction. *PCI Journal*, 40(1), pp.82–93.

El-Hacha, R., El-Agroudy, H. & Rizkalla, S.H., 2006. Bond Characteristics of High-Strength Steel Reinforcement. *ACI Structural Journal*, 103(6), pp.771–782.

Eligehausen, R., Popov, E.P. & Bertero, V. V., 1982. Local bond stress-slip relationships of deformed bars under generalized excitations. In *Proceedings of the 7th European Conference on Earthquake Engineering*. Athens, Greeze, pp. 69–80.

Elsayed, M. & Nehdi, M.., 2017. Experimental and Analytical Study on Grouted Duct Connections in Precast Concrete Construction. *Materials and Structures*, 50(198), pp.1–15.

Ganesan, N., Indira, P. V. & Sabeena, M. V., 2014. Bond stress slip response of bars embedded in hybrid fibre reinforced high performance concrete. *Construction and*

Building Materials, 50, pp.108–115.

Marchand, P. et al., 2015. Bond behaviour of reinforcing bars in UHPFRC. *Materials and Structures*, 49(5), pp.1979–1995.

Matsumoto, E.E. et al., 2008. Development of a precast concrete system. *PCI Journal*, 53(3), pp.74–86.

PCI, 2010. PCI Design Handbook 7th Edition. *Precast Concrete Institute, Chicago, IL*, (October), pp.1–828.

Raynor, D.J., Dawn, E.L. & Stanton, J.F., 2002. Bond-Slip Response of Reinforcing Bars Grouted in Ducts. *ACI Structural Journal*, 99(5), pp.568–576.

El Refai, A., Ammar, M. & Masmoudi, R., 2015. Bond Performance of Basalt Fiber-Reinforced Polymer Bars to Concrete. *ASCE Journal of Composites for Construction*, 19(3), pp.1–12.

Seifi, P., Henry, R.S. & Ingham, J., 2015. Preliminary test results of precast concrete panels with grouted connections. In *New Zealand Society for Earthquake Engineering Technical Conference*. Rotorua, New Zealand, pp. 744–751.

Steuck, K.P., Eberhard, M.O. & Stanton, J.F., 2009. Anchorage of large-diameter reinforcing bars in ducts. *ACI Structural Journal*, 106(106), pp.506–513.

Tastani, S.P. & Pantazopoulou, S.J., 2010. Direct Tension Pullout Bond Test: Experimental Results. *Journal of Structural Engineering*, 136(6), pp.731–743.

Tastani, S.P. & Pantazopoulou, S.J., 2013. Reinforcement and concrete bond: State determination along the development length. *ASCE Journal of Structural Engineering*, 139(9), pp.1567–1581.

Chapter 4

4 EXPERIMENTAL AND ANALYTICAL STUDY ON GROUTED CONNECTIONS IN PRECAST CONCRETE CONSTRUCTION

4.1 INTRODUCTION AND BACKGROUND

Precast concrete construction has gained a great momentum over the past couple of decades owing to combining the speed and accuracy of a plant manufactured products and the related body of knowledge, in terms of design specifications and research data, that have been cumulated. Design schemes for precast systems can take several forms. Load-bearing precast walls and double tees or hollow core flooring are often used conjointly. Vertical precast wall panels can be conveniently connected in the field using a grouted connection, often used due to its favourable tolerances and weld elimination. The connection can also be used to resist in plane tension arising from lateral loads. **Figure 4.1** displays a typical wall-to-wall detail highlighting such a grouted connection. A large diameter reinforcing bar (No.8 or larger) is typically bridged over the horizontal joint between two vertical panels via a mechanical coupler. The extended length is then grouted inside a corrugated metallic duct, which is embedded in the precast panel.
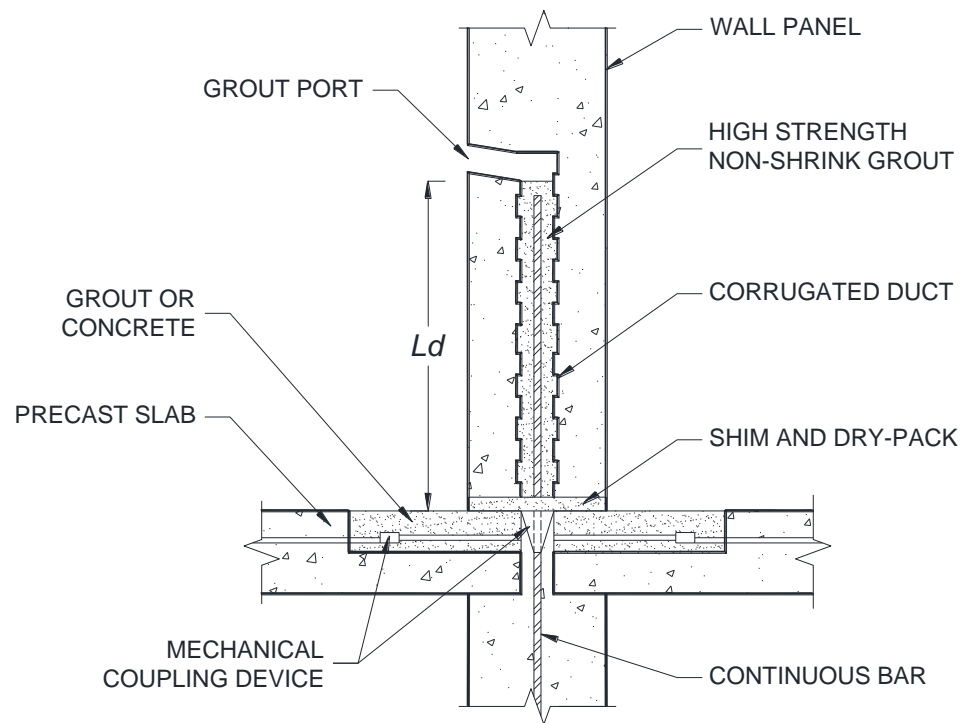
Figure 4.1: Schematic diagram showing a grouted connection.

The use of grouted connections in precast load-bearing walls is subject to the following requirements: (i) to satisfy structural integrity requirements (a minimum of two ties per panel according to ACI 318-14 Section 16.2.5) (ACI Committee 318 2014); and (ii) to carry tensile loads induced from in-plane lateral loads. During excessive seismic demands and damage accumulation, the connection provides ductility to the assembly, which is often in the form of the horizontal gap opening between two vertically stacked walls. This is manifested due to the yielding of the bar. This non-linearity releases energy and enables a more ductile structure. Recent seismic events mandate dedicated investigation of these modes. This topic will be addressed by the authors in later publications.

Per ACI 318-14 and PCI 2010, grouted connections are modelled after the equations describing the development of deformed bars in tension. Some of the equations that describe the development length in tension are shown in **Table 4.1** (where; L_d = development length in tension; f_y = reinforcement yield stress; $f_{c'}$ = concrete compressive strength; $\left(\frac{c_b + k_{tr}}{d_b}\right)$ = confinement factor; d_b = diameter of bar; d_{duct} = diameter of duct; β =

modification factor for duct material; $f_{s,cr}$ = critical level of stress in reinforcement; γ = modification factor due to group effect; $f_{cg'}$ = grout compressive strength).Yet, while there is common perception among experts that the behaviour of bars grouted ducts has shown substantial discrepancy with the bar-in concrete idealization, this is neither quantified nor documented in the open literature.

Table 4.1: Various Empirical equations for grouted connections

Source[*]	Model	Variables
ACI 318-14	$L_d = \dfrac{3f_y}{40\sqrt{f_c'}\left(\frac{c_b+k_{tr}}{d_b}\right)}$	$L_d = Development\ Length\ in\ Tension$ $f_y = Reinforcement\ Yield\ Stress$ $f_c' = Concrete\ Compressive\ Strength$
Steuck et al. (2009)	$L_d = \dfrac{f_y}{130\sqrt{f_g'}}d_b + \left(\dfrac{d_{duct}-d_b}{2}\right)$	$\left(\dfrac{c_b+k_{tr}}{d_b}\right) = Confinement\ Factor$ $d_b = Diameter\ of\ Bar$ $d_{duct} = Diameter\ of\ Duct$
Brenes et al. (2006)	$L_d = \dfrac{\beta f_{s,cr}}{45\gamma\sqrt{f_c'}}d_b$	$\beta = Modification\ factor\ for\ Duct\ Material$ $f_{s,cr} = Critical\ Level\ of\ Stress\ in\ Reinforcement$ $\gamma = Modification\ Factor\ for\ Group\ Effect$
Matsumoto et al. (2008)	$L_d = \dfrac{0.024f_y}{\sqrt{f_{cg}'}}d_b$	$f_{cg}' = Grout\ Compressive\ Strength$

Einea et al. (1995) were among the first studies on the confinement effect of metallic sleeves. In their work, they proposed a grout-filled steel tubing as a splice sleeve to bridge reinforcement bars with variable bar diameter and embedment length. The degree of confinement was varied by changing the connection scheme. All their specimens failed by pull-out of the reinforcing bars via shearing of the grout keys. Raynor et al. (2002) evaluated the bond between deformed bars in grouted ducts commonly used in hybrid frames. The bars had short embedment lengths and were tested using monotonic and cyclic loading. Higher bond stresses for grouted connections were observed and attributed to the confinement effect of the duct. Similar observations were also reported by (Steuck et al. 2009) who conducted pull-out tests on large diameter bars grouted in vertical ducts to be used in a bridge bent cap system. Embedment lengths 3 times smaller than that recommended by the ACI 318-05 were sufficient to mobilize the tensile capacity of the bar. This was ascribed to the additional passive confinement provided by the duct (Steuck et al. 2009).

Brenes et al. (2006) undertook a comprehensive study to explore the influence of changing the corrugated duct materials on the behaviour of grouted connections. The main test parameters investigated were the bar coating, duct material, transverse reinforcement, bar eccentricity and number of connections. It was observed that the behaviour of grouted connections was largely dependent on the stiffness of the duct material and its ability to accommodate lateral strains. Matsumoto et al. (2008) tested various schemes used as grouted connections under pull-out and cyclic conditions. Test parameters included the bar diameter and embedment length. It was found that splitting failures did not occur in grouted connections, which was attributed to the role of the duct.

Based on the above literature, there is general consensus on the differentiation between the bond failure of deformed bars grouted in corrugated ducts and the that of deformed bars in concrete. Nonetheless, the majority of pertinent studies deal with the use of grouted connections in precast bent cap systems and often reported empirical models to predict the behaviour of grouted connections as summarized in **Table 4.1** (Matsumoto et al. 2008; Einea et al. 1999; Steuck et al. 2009; Brenes et al. 2006).

Considering the sensitivity of bond to various influential factors, the results of these studies cannot be extrapolated to the behaviour of grouted connections used in precast walls. In view of the sparsity of information available on the behaviour of grouted connections used in precast walls, a dedicated experimental methodology is presented herein to address remaining knowledge gaps. Thus, the objective of this paper is threefold: (i) Experimentally evaluate the behaviour of a typical grouted connection detail; (ii) Provide quantitative experimental evidence to differentiate between the behaviour of grouted connections and bars embedded in concrete; and (iii) Coin a reliable empirical expression which can estimate the behaviour of grouted connections and ultimately serve as a user-friendly design tool. This paper reports the findings of experimental and analytical programmes that describe the characteristic bond stress of grouted connections. Direct comparison between the connections and their duct-less counterparts show that, under the same conditions, grouted connections do not suffer from splitting failures, which is attributed to the restraining effects of the corrugated duct.

4.2 EXPERIMENTAL PROGRAM

4.2.1 Test Specimens

To compare the behaviour of grouted connections to that of bars embedded in concrete, the experimental program was designed to measure the response of specimens under identical conditions. The first test set consisted of bars embedded in concrete, while the second set comprised grouted connections anchored at a similar embedment length and tested under similar setting. As depicted in **Figure 4.2**, the specimens consisted of non-reinforced concrete prisms measuring 203.2 x 203.2 x 406.4 mm mimicking the case of a typical precast wall.
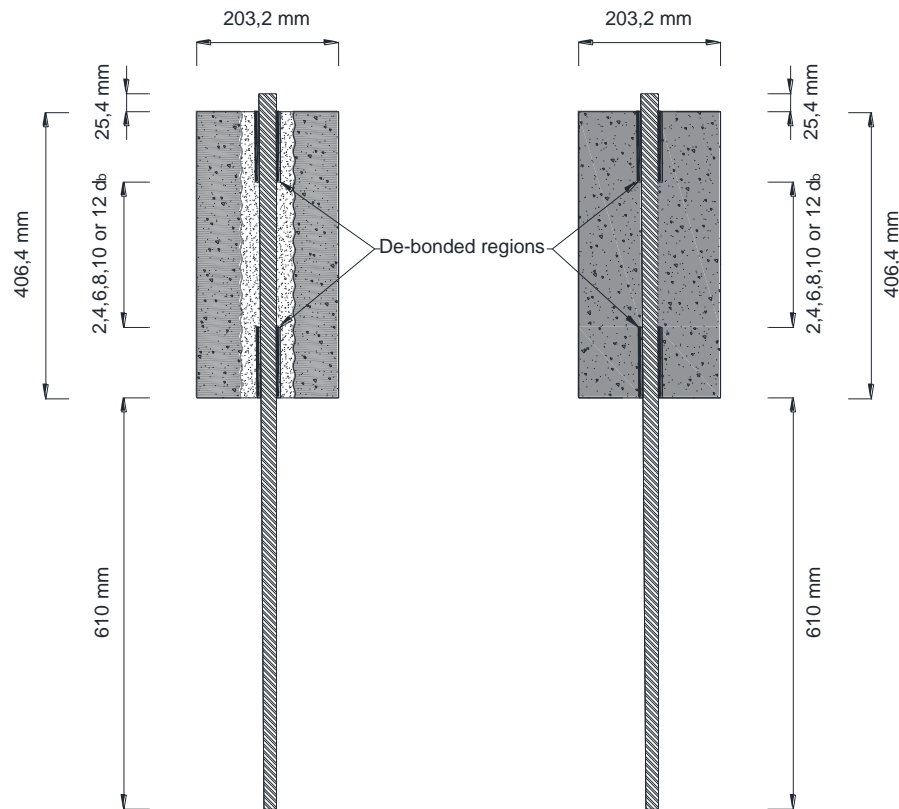
Figure 4.2: Test specimens: (left) Grouted specimen; (right) Bar in concrete specimen.

Grouted connection specimens had a 76-mm diameter and 30-gauge corrugated steel duct embedded concentrically in the prism. De-bonding of the bars was carried out by wrapping them with 2-mm thick polystyrene wrap. The de-bonded length varied depending on the

embedment length of the specimens (2, 4, 6, 8, 10 and 12 d_b embedment were considered in this study). The embedment lengths were chosen to allow for an assessment of the bond at the elastic and inelastic segments of the idealized bond stress versus slip curve. After concentric placement of the bars inside the corrugated duct, non-shrink grout was mixed at low speed for 10 minutes then at high speed for 5 minutes, adding water until a desirable flowing consistency was achieved, after which grouting of the specimens was carried out in the vertical position.

4.2.2   Materials Properties

Table 4.2: Concrete mixture design and mechanical properties

Materials	Per 1 m³	Comp. Strength (MPa)		Tensile Strength (MPa)		Young's Modulus x 10³ (MPa)		Poisson's Ratio	
		Age (Days)							
		7	28	7	28	7	28	7	28
Concrete									
CSA Type 30 Cement	435 kg								
Sand	842 kg								
14 mm aggregate (round)	842 kg								
Water	200 Litres								
Air	5 %	53.7	61.6	5.1	6.1	26.0	26.0	0.25	0.24
Air Entrainment/Lubricant	20 ml/100 kg cement								
High Range Water Reducer	630 ml/100 kg cement								
Grout									
Proprietary High Strength Non-Shrink grout (ASTM C1107	-	38.4	39.3	4.5	6.3	20.7	22.7	0.22	0.23

The concrete mixture composition and mechanical properties of the concrete used in the study are shown in **Table 4.2**. Concrete used in this study was self-consolidating produced at an industrial plant. The mechanical properties of the concrete and grout were determined as per the procedure outlined in ASTM C39 (2016) for compressive strength, ASTM C496/C496M (2011) for splitting tensile strength, ASTM C469/C469M-14 (2014) for modulus of elasticity. The 28-day compressive and splitting tensile strengths (average values obtained on three identical 100 x 200 mm cylinders) were 50.6 MPa and 5 MPa, respectively. The grout used in connections is a proprietary high-strength non-shrink mixture with an average 28-day compressive strength of 40 MPa and tensile strength of 6 MPa.

As per the manufacturer's recommendations, 3.8 litres (1 US gal) of water was added to each 25 kg (55 lb) dry bag to achieve a self-levelling consistency. All specimens were cured for 28 days at ambient conditions (*T* of 23°C and *RH* of 60%). The connector dowels used in the specimens consisted of grade 400 No .8 (25-mm) deformed bars. All steel used in this study was sourced from a single production from the same supplier. Mechanical properties of the connector dowel were tested according to the ASTM 370 guidelines (ASTM 370 2014). The average yield stress and the corresponding yield strain were 418 MPa and 0.2-0.23%, respectively. The ultimate tensile stress and strain were 603 MPa and 1.2-1.8%, respectively.

4.2.3   Pull-out Testing

The adequacy of using of pull-out tests to evaluate the bond between concrete and reinforcement has been a matter of controversy. Indeed, stresses at the anchored end of a pull-out specimen vary considerably from those typically encountered in service. This un-realistic stress state where the bar is exposed to tensile stresses and a longitudinal normal compressive field is applied unto the concrete can artificially enhance the bond of the bar through additional confinement (**Figure 4.3**).
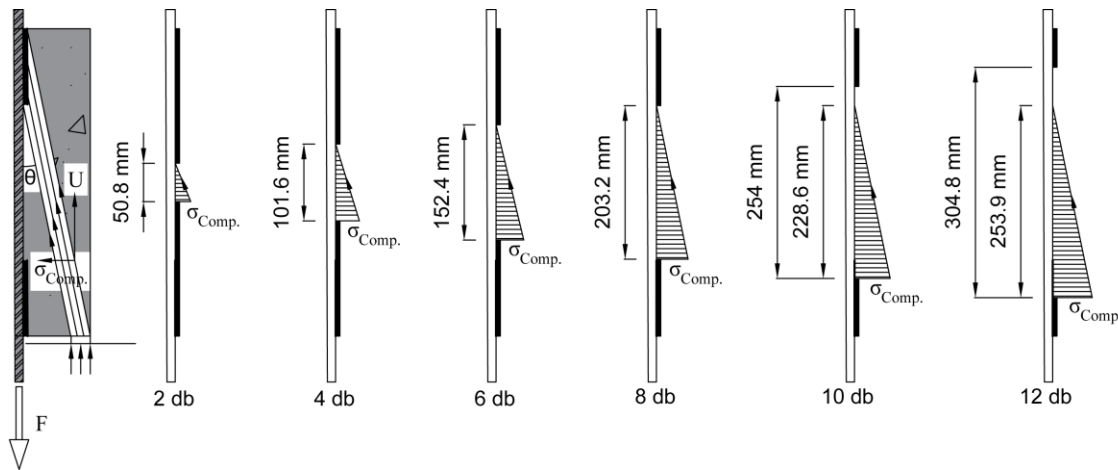
Figure 4.3: Strut and Tie analysis of the superficial compressive fields resulting from the boundary conditions at: (from left to right) 2, 4, 6, 8, 10, and 12 d_b embedment length.

Friction between the specimen and bearing plates additionally magnifies this effect. Likewise, bond is not directly measured by the commonly used tests and is known to be sensitive to a multitude of influential factors, including confinement, compressive strength

and the physical and mechanical properties of the bar. Nevertheless, pull-out tests provide a simple and economical means to comparing anchored bars tested under similar conditions (Achillides & Pilakoutas 2004; El Refai et al. 2015; Steuck et al. 2009; Matsumoto et al. 2008). In the present study, pull-out testing was adopted while careful consideration is exercised to reduce the artefacts mentioned above. The mitigation of such bond enhancing conditions was achieved through a two-tier strategy: first, a 215.9 mm x 215.9 mm x 25.4 mm hollow steel cradle with 152.4 mm x 152.4 mm opening was used beneath the specimen to reduce the confinement in the immediate vicinity of the bars, and for a length of 5 d_b in both directions. Second, the de-bonding of the bars away from the active end of pulling (where the effects of the induced compression are most prevalent) helped shift the tested zone to regions where the magnitude of the compressive field is of a lesser intensity.

4.2.4   Test Procedure

Two specimens were tested for each set of parameters to verify repeatability of the results. The average of the two measured responses was used for analysis purposes unless otherwise mentioned. After curing each specimen for 28 days, it was placed atop the active pulling end of an open loop Tinius Olsen testing machine with a maximum capacity of 530 kN, as shown in **Figure 4.4.**

The loading machine was calibrated prior to the beginning of the testing to ensure that the load was consistent among the specimens. The bar was extended to the lower plate and gripped by two steel jaws over a length of 165.1 mm, where the load was applied monotonically at a rate of 60 MPa/min. To record the slip of the bar, a 25-mm strain based linear variable displacement transducer (LVDT) was mounted by a steel tripod and placed on the protruding bar from the top (unloaded end) to record the slip relative to the top surface of the specimen. The elongation of the bar at the loaded end of the specimen was monitored by measuring the relative movement between the fixed and moving heads of the machine via a 150-mm spring LVDT. Prior to each test, the calibration of both LVDTs used in the study was checked with the aid of precision gage blocks to ensure accuracy. During the test, a data acquisition system recorded the load and slip readings at a rate of 10 reading per second.
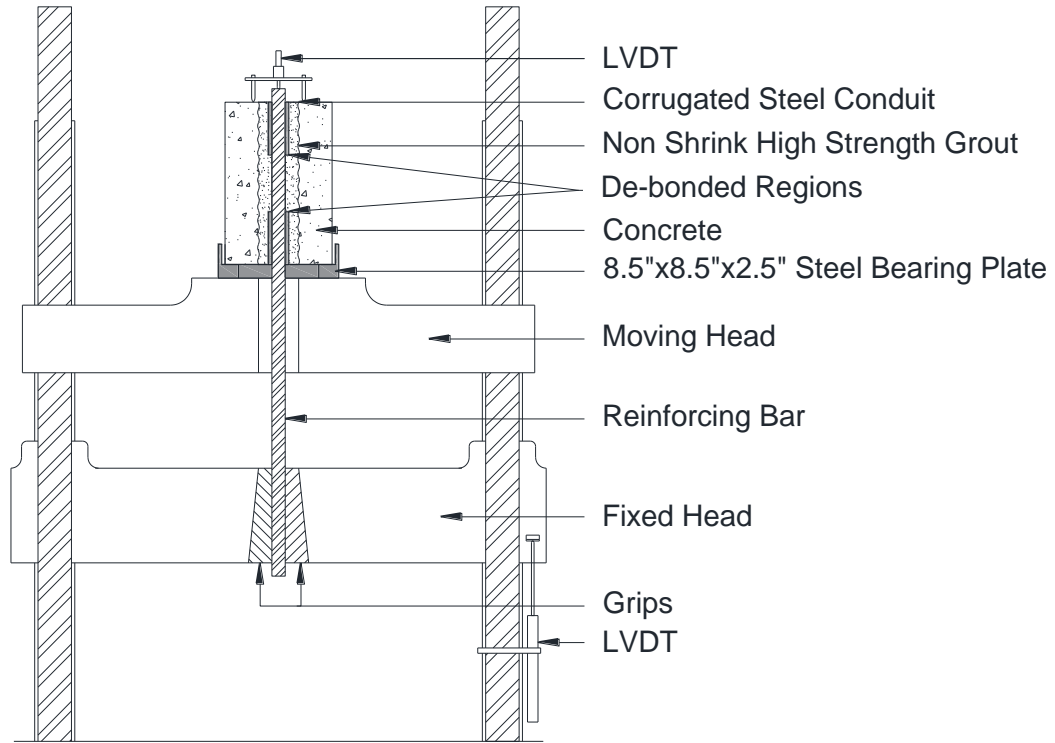
Figure 4.4: Test setup and instrumentation.

4.3   EXPERIMENTAL RESULTS AND DISCUSSION

Results from the 24 pull-out test specimens are presented in **Table 4.3** where: L_d = embedment length in d_b; F_{max} = ultimate load; U_{av} = maximum average bond stress; U_{rs} = maximum residual bond stress; f = stress in the reinforcement; S_{max} = slip corresponding to maximum average bond stress; D_{max} = displacement at peak load; α_{BPE} = coefficient corresponding to the level of confinement.

Table 4.3: Pull-out test results

(1) Specimen Tag	L_d (d_b)	F_{max} (kN)	U_{av} (MPa)	U_{rs} (MPa)	f (MPa)	S_{max} (mm)	D_{max} (mm)	α_{BPE}	k-s	Failure Type
C-2-D1	2	60.90	15.02	14.26	120.19	1.33	9.50	0.25	0.49	Pull-out
C-2-D2		74.50	18.38	15.02	147.03	3.22	11.90	0.27	0.45	Pull-out
C-4-D1	4	191.92	23.67	19.18	378.76	1.21	13.50	0.34	0.30	Splitting + Pull-out
C-4-D2		179.76	22.17	18.78	354.76	3.36	15.40	0.34	0.37	Splitting + Pull-out
C-6-D1	6	204.80	16.84	5.31	404.18	2.04	17.10	0.32	0.34	Splitting + Pull-out
C-6-D2		245.52	20.16	(2) NA	484.54	0.78	35.60	0.49	0.32	Splitting
C-8-D1	8	297.33	18.33	-	586.78	0.86	87.00	-	-	Bar Fracture
C-8-D2		295.88	18.24	-	583.93	0.62	87.70	-	-	Bar Fracture
C-10-D1	10	298.52	14.73	-	589.14	0.06	82.00	-	-	Bar Fracture
C-10-D2		296.65	14.64	-	585.45	0.06	81.70	-	-	Bar Fracture
C-12-D1	12	297.08	12.21	-	586.29	0.04	74.60	-	-	Bar Fracture
C-12-D2		296.33	12.18	-	584.82	0.03	69.81	-	-	Bar Fracture
NS-2-D1	2	72.42	17.87	13.57	142.92	0.82	11.60	0.18	0.40	Pull-out
NS-2-D2		76.33	18.12	14.69	150.64	1.07	11.10	0.19	0.35	Pull-out
NS-4-D1	4	214.41	26.45	22.73	423.14	0.60	17.40	0.23	0.39	Pull-out
NS-4-D2		206.35	25.45	21.02	407.23	0.62	12.70	0.26	0.30	Pull-out
NS-6-D1	6	263.97	21.71	19.57	520.95	0.62	33.70	0.23	0.44	Pull-out
NS-6-D2		250.91	20.63	18.86	495.17	0.94	43.51	0.19	0.55	Pull-out
NS-8-D1	8	286.10	17.64	15.65	564.63	0.66	85.10	0.17	0.58	Pull-out
NS-8-D2		287.76	17.75	13.58	567.89	0.66	77.70	0.13	0.56	Pull-out
NS-10-D1	10	285.30	14.08	12.84	563.05	0.56	82.60	0.11	0.53	Pull-out
NS-10-D2		293.38	14.47	13.66	578.98	0.73	93.20	0.07	0.63	Pull-out
NS-12-D1	12	304.90	12.54	-	601.73	0.06	94.60	-	-	Bar Fracture
NS-12-D2		303.24	12.46	-	598.40	0.09	98.90	-	-	Bar Fracture

Note: Fmax = ultimate load; f = peak stress in bar; Uav= average bond stress; Urs= residual bond stress Smax = slip corresponding to maximum bond stress; Dmax = displacement corresponding to maximum bond stress; k-s = Kolmogorov-Smirnov statistic.

*(1) **NS and C** refer to Non-Shrink grout and Concrete, respectively; **2, 4, 6, 8, 10 and 12** refer to the bar embedded length, respectively; **D1 and D2** refer to the specimen repetition identifier.*

(2) Data became unreliable

Specimens were labelled as follows: the first set of characters represents the type of matrix used (NS for non-shrink and C for concrete), followed by a numeral representing the embedment length (2, 4, 6, 8, 10 or 12 d_b). The next set of characters represents the type of bar used (D for deformed steel bars) and the following number refers to the specimen number in its group (1 or 2). For example, NS-12-D2 refers to a deformed bar connection specimen with an embedment length equal to 12 times the bar diameter, while specimen C-4-D1 refers to a deformed bar in concrete embedded along 4 times the bar diameter.

The assumption of uniform bond stress along the length of an embedded bar is not an accurate simplification, specifically when the embedment is longer than 3-7 d_b (Tastani & Pantazopoulou 2013). As the embedment length increases, non-linearity in the distribution is introduced. The distribution tends to peak closer to the loaded end of the bar and attenuates non-linearly towards the passive end. The exact distribution of the bond stresses along the embedded length of a bar cannot be determined without extensive instrumentation. For this reason, several researchers often find it practical to resort to this simplification (Steuck et al. 2009; Einea et al. 1995; Ganesan et al. 2014; Ashtiani et al. 2013; Tastani & Pantazopoulou 2010; El Refai et al. 2015; El-Hacha et al. 2006; Marchand et al. 2015). It is also relevant to highlight that this assumption is supported by ACI Committee 408R-03 which states that "…it is both convenient and realistic to treat bond forces as if they were uniform over the anchored, developed, or spliced length of the reinforcement" (ACI Committee 408 2003). Given that, the average bond stress U was calculated as the force along the embedded length per unit surface area of the bar, as shown in **Eq. 4.1** as follows:

$$U = \frac{F}{\pi\, d\, L_d} \tag{4.1}$$

Where F is the tensile load; d is the nominal bar diameter; and L_d is the bar embedment length.

4.3.1   Bond Failure Mechanisms

Illustrations of the failure modes encountered in this study are shown in **Figure 4.5**. Failure modes of representative test specimens are also exhibited in **Figure 4.6.** Additionally, **Figure 4.7** shows the profile of the failed bars.
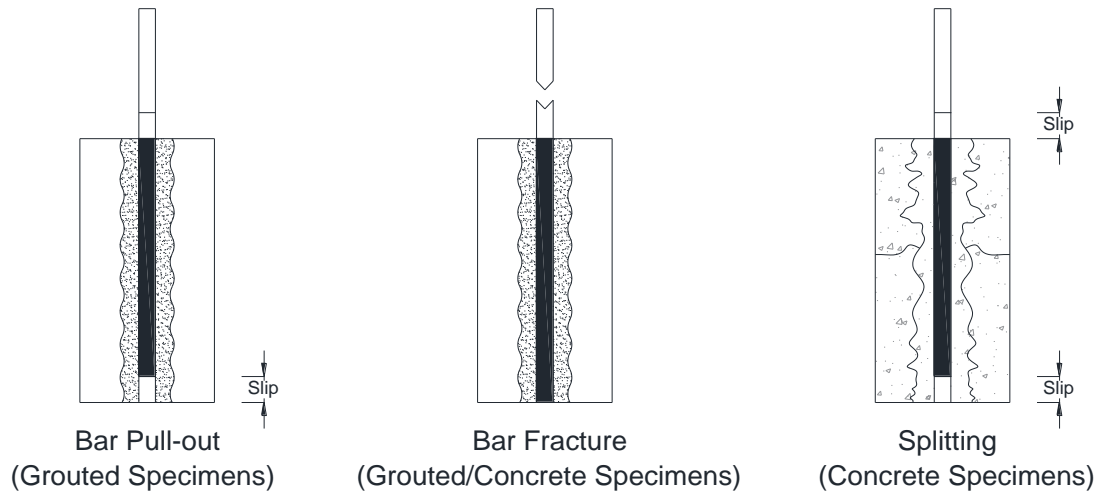
Figure 4.5: Failure modes of different specimens

All concrete specimens failed by a mixed (splitting/ pull-out) mode, except specimens embedded at 8, 10 and 12 d_b, which failed by bar fracture. Ducted specimens failed by pull-out, except for NS-12-D1 and D2, where a bar fracture occurred. At an embedment length of 2 d_b, comparable specimens from the two groups failed by bar pull-out. At this short embedment length, the engagement of the ribs did not generate sufficient hoop tension to cause an apparent splitting failure. The slip of the bars is rather dependant on the local failure at the interface between the concrete and bar ribs. This was not the case when the embedment length was 4 and 6 d_b, where concrete specimens experienced splitting cracks propagating to the surface since the concrete hoop tension was the primary confining action contributing to the slip resistance (**Figure 4.6**). At 4 d_b and 6 d_b, longitudinal cracks started initiating towards the loaded end and continued to grow along the embedment length. As the loading continued, these cracks propagated transversally, causing portions of the block to completely separate, as observed in **Figure 4.6**. The bars eventually failed by pull-out with splitting along a plane that extended from the crest of a rib to the bottom of a successive one, as exhibited in **Figure 4.7.**

Figure 4.6: (left to right) Split tensile cracking (C-4-D1); Pull-out failures vs splitting failures of comparable specimens at 6 and 4 db (NS-6-D1/ C-6-D1 and C-4-D2/ NS-4-D1, respectively); and Slippage of bars vs bar fracture at 10 db embedment (C-10-D2 and NS-10-D2).

Figure 4.7: (left to right) Wedging of grout keys between ribs in a (C-6-D2); and Crushing of grout keys between ribs at 6 and 10 db embedment (NS-6-D1 and NS-10-D2, respectively).

Comparable grouted specimens (4 and 6 d_b embedment) had a failure that differed considerably from their concrete counter parts. As shown in **Figure 4.7**, bars from these specimens failed by crushing of the concrete between the ribs, indicating a compression

failure. No splitting cracks were observed inside the grout cylinder or anywhere on the outer surface of the concrete block (**Figure 4.8**).

The absence of splitting failures at this embedment length points to the contribution of the corrugated duct in resisting the lateral expansion of the grout. This observation is supported by three main arguments: (i) consistently higher bond stresses were achieved by grouted specimens; (ii) scatter of the results between the subgroups of the concrete specimens inherent from the nature of concrete exposure to tension (average COV of 70% and 350% for 4 and 6 d_b, respectively); and (iii) the additional resistance against slip provided by ducted specimens.
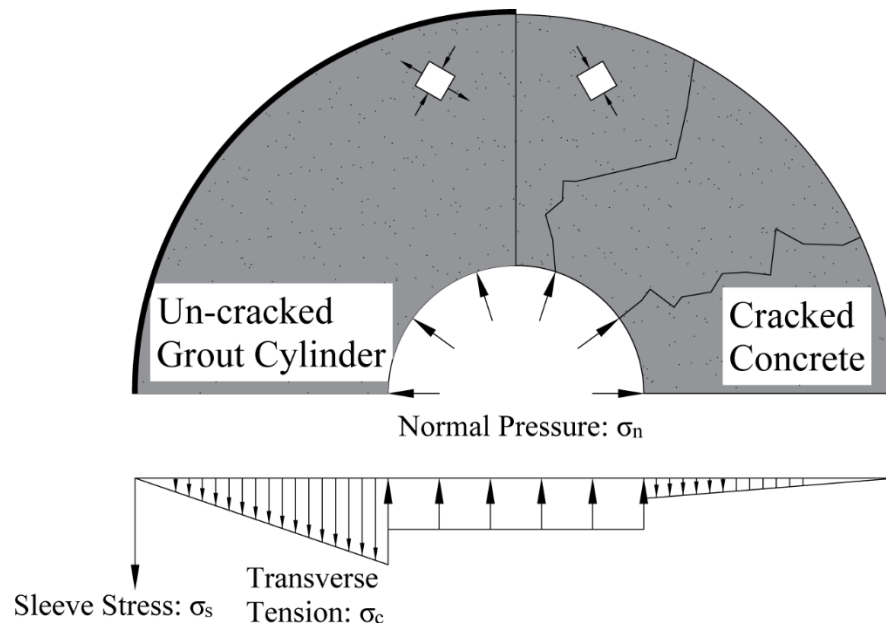
Figure 4.8: Stress state inside corrugated grouted connection vs cracked concrete cylinder.

Concrete specimens with bars embedded at 8 and 10 d_b failed by rupture of the bars at a stress corresponding to the average measured tensile capacity**.** Comparable grouted specimens failed by pull-out of the bars via shearing of the grout keys, similar to their 4 and 6 d_b specimens, as depicted in **Figure 4.7(c)**. It should be noted that the crushing of the grout keys in the failure of grouted specimens occurred irrespective of the value of the bond stress. This observation, when viewed considering the bar strain levels, reveals that

the bond of grouted connections did not seem to be affected by the level of strain of the bar, but rather by the amount of slip mobilized unto it.

4.3.2   Bond Stress - Slip Behaviour

A comparison of the bond behaviour of grouted specimens compared to that of their duct-less concrete counterparts is portrayed in **Figure 4.9** (representative specimens at different embedment lengths)**.**
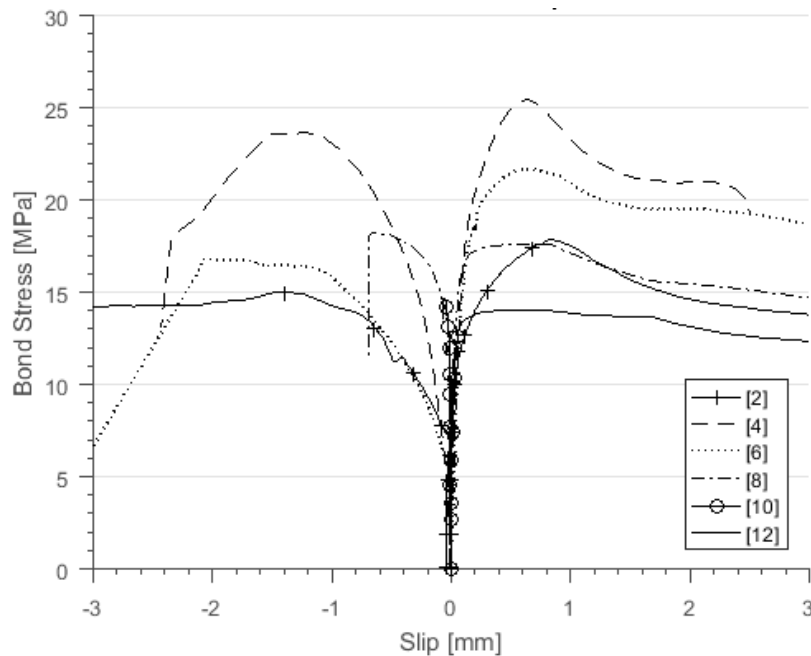
Figure 4.9: Bond stress vs slip response of representative grouted specimens (positive slip) and concrete specimens (negative slip) at 2, 4, 6, 8, 10 and 12 d_b embedment.

The typical bond stress-slip response was characterized by an ascending branch, a region where the maximum bond plateaus over a certain slip domain, followed by a softening branch with varying slope. The softening branch of the bond-slip response of grouted specimens was characterized by predominant slip (**Figure 4.9**). Although this trend prevailed regardless of the embedment length, significant differences can be observed between the responses of the two types of specimens tested.

Up until an embedment length of 8 d_b, the ascending branch of the bond of grouted connections appeared to have a stiffer response. The increased stiffness of grouted specimens was highlighted when comparable specimens failed in the pull-through mode

and not via bar fracture. This observation was specifically pronounced when the embedment length was 4 and 6 d_b since these embedment lengths present a loading case which imposes critical hoop tension levels. Additionally, grouted specimens consistently achieved, on average, 7.7%, 13.2%, and 14.4% higher bond stress than that of their concrete counterparts for the 2, 4, and 6 d_b embedment lengths, respectively.

Considering the nominal increase in the maximum average bond stress, it is important to examine this under the slip domain over which it occurred. To highlight this, the slip recorded for each specimen was normalized by the value of slip at maximum bond stress (Table 3: S_{max}). **Figure 4.10** exhibits the slip versus its value when normalized by the slip at maximum bond stress of various specimens. The degree of slip under a certain level of bond stress is illustrated as the slope of the plotted line, whereby a steeper slope indicates higher slip. It can be observed in **Figure 4.10** that grouted specimens incurred less slip than that in their concrete counterparts, irrespective of the embedment length.
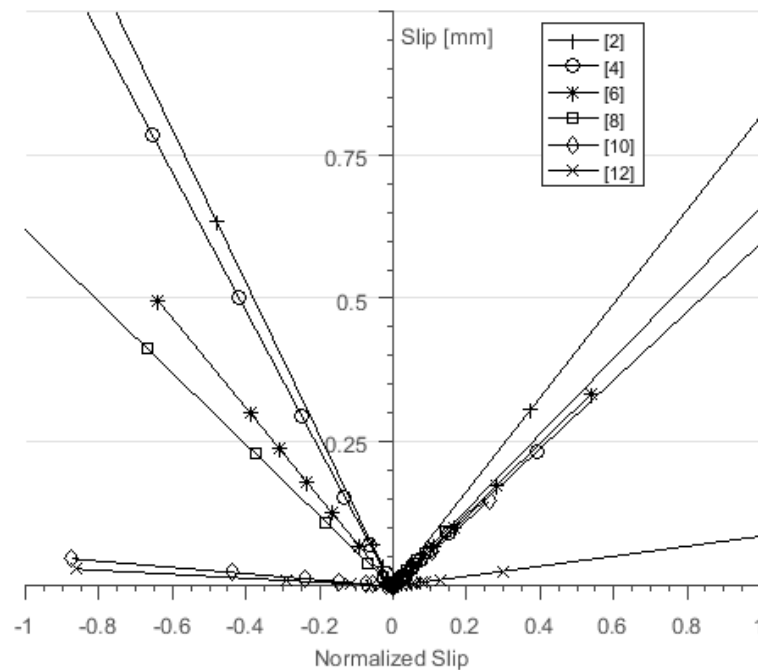
Figure 4.10: Comparison between slippage of bars at different embedment: (left) Concrete; (right) Grouted connections.

However, at shorter development lengths, bars in concrete slipped significantly more. This was partly attributed to the exposure of the concrete cover to excessive tensile stresses and

its subsequent dilatation. Moreover, grouted connections had an arresting mechanism through the confinement effect provided by the corrugated duct. Comparable slopes were obtained once the failure of the specimens shifted from a mixed/pull-out to a bar fracture failure (10 and 12 d_b).

Comparable concrete specimens had a steep softening branch after the maximum bond stress was attained. This can be further examined by analysing the post-maximum bond stress, or residual bond stress, which describes the bond behaviour after reaching its maximum capacity, giving insight into the additional resistance along the failing branch of the bond stress-slip response. Residual bond stresses were extracted by examination of individual bond-slip curves of grouted and concrete specimens via determining the corresponding bond stress of the point on the softening branch at which either a flattening of the curve or a sudden change in slope occurred. The recorded values are given in **Table 4.3**. Grouted specimens achieved an average residual stress increase of 4.9, 15.9 and 72% at 2, 4 and 6 d_b, respectively. A possible reason would be the normal confining pressure of the corrugated duct specimens, enhancing the frictional aspects of the bond, which was not engaged until the rib bearing components of bond have been exhausted.

4.3.3 Bond Stress - Bar Strain Behaviour

The elongation of the bars was measured via an LVDT affixed to the testing machine (**Figure 4.4**), which monitored the relative movement between the moving and fixed heads. The starting point of all tests (distance between the fixed and moving heads) was kept constant. Hence, the initial length of the bars was taken as the distance between the upper end of the grips and the end of the de-bonded length. The measured elongation was then corrected by subtracting the recorded slip at the unloaded end. With the knowledge of the original and elongated lengths of the bars, the average strain during the test was calculated. **Figure 4.11** depicts the average bond stress versus strains and provides useful insights into the bond behaviour (and its corresponding failure) under different bar strain levels (elastic, yielding, and plastic).
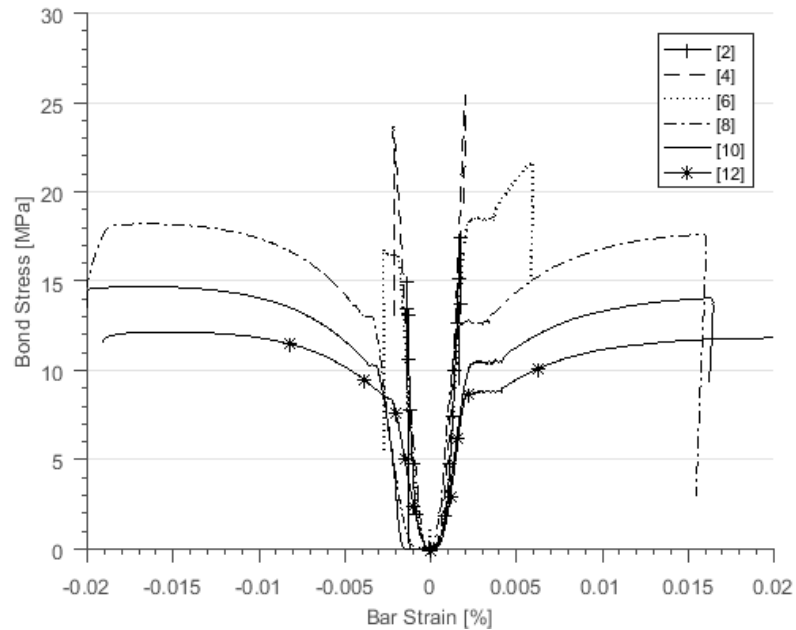
Figure 4.11: Bond Stress vs. Bar Strain for representative specimens: (Left) bars embedded in concrete; (right) grouted connections at 2, 4, 6, 8, 10 and 12 d_b embedment.

Comparable bond stress and corresponding strain values (<0.1%) can be observed from the comparison of concrete and grouted specimens at 2 d_b embedment length. This is consistent with failure patterns discussed earlier. At 4 d_b, the grouted specimens had 7% increase in bond at a comparable strain (0.20 and 0.21% for grouted and concrete, respectively). Visual examination did not indicate bar yielding. However, this strain level is very close to the yield strain recorded from test coupons (0.2-0.6%). Yet, the increase in bond stress did not invoke tensile failure in the grouted specimens, which was the primary mode of failure of comparable concrete specimens. It is important to note that the concrete specimens had an average 28-day compressive strength 56% higher than that of the grout. At 6 d_b embedment, bars representing both groups indicated a visible yield plateau at 18.53 and 16.51 MPa for the grouted and concrete specimens, respectively, with splitting cracks dominating the pull-out failure of the concrete specimens. Grouted specimens failed by crushing of the grout keys (pull-out) in the strain hardening zone. It is interesting to highlight that at an 8 d_b embedment; the concrete block did not suffer splitting cracks despite the maximum average bond stress of 18.24 MPa (10.5% increase from 6 d_b). This is a result of the engagement of additional bar ribs, which effectively reduced the transverse tension on the concrete cover, since the force is divided by a greater number of ribs.

Grouted specimens embedded at 8 and 10 d_b yielded similar observations to the grouted 6 d_b specimens, all of which displayed pull-out failures at a strain level equal or slightly exceeding the ultimate tensile strain of the bar.

4.3.4   Analytical Analysis

In an attempt to mimic the behaviour of grouted connections, the analytical bond-slip law proposed by Eligehausen et al. (1982), BPE model was considered. This model was adopted by the CEB-FIP code (1990) and has been utilized by several other (El Refai et al. 2015; Comite Euro-International Du Beton 1993; Cosenza et al. 1997; Baena et al. 2009; Ashtiani et al. 2013). In the present study, the model was calibrated using experimental results obtained from pull-out through the average bond stress calculated using **Eq. 4.2** and the free-end slip values measured and reported in **Table 4.3**. The ascending branch ($s \leq s_1$) of the BPE model is expressed by the following relation:

$$\frac{\tau}{\tau_{max}} = \left(\frac{s}{s_{max}}\right)^{\alpha}$$

(4.2)

Where τ and s are the corresponding bond stress and slip at any loading increment; τ_{max} and s_{max} are the maximum recorded average bond stress and slip, respectively; and α is a model fitting parameter.

According to MC90, the value of α should be between 0 and 1 to be physically meaningful and a recommended value of 0.4 should be used for confined and un-confined concrete (Comite Euro-International Du Beton 1993). A value of α closer to 0 implies stiffer response where a steep increase in bond stress is reached without much slip. The second branch of the model calls for a constant bond stress region ($\tau = \tau_{max}$) when the slip domain is between s_1 and s_2, at which point, a linearly descending branch describes the behaviour of the softening branch of the bond ($s_2 < s < s_3$). For $s > s_3$, a horizontal branch depicts the friction as $\tau = \tau_f$. Thus, to adapt the model to the current state, parameters α, s_2, s_3 and τ_f should be calibrated using experimental results.

To calibrate the parameter α, Cosenza et al. (1997) presented the following relationship:

$$A_\tau = \int_0^{s_1} \tau_{max} \left(\frac{s}{s_{max}}\right)^\alpha ds = \frac{\tau_{max} \cdot s_1}{1 + \alpha} \tag{4.3}$$

where A_τ is the area underneath the ascending branch of each specimen.

The parameter α was calibrated by equating the areas underneath the ascending branch of the experimental data to **Eq. 4.3**. However, careful consideration was taken when equating the two areas so as not to compromise the trend of the curve (Cosenza et al. 1997). The goal was to calibrate the model for grouted connections, but later expanded to the concrete group to provide a basis of comparison between the two groups. The values of α obtained for each specimen (failing in pull-out) are shown in **Table 4.3**.

To facilitate the comparison between the experimental and analytical results, the goodness-of-fit was analysed using the two-sample Kolmogorov-Smirnov test (K-S test). The K-S test examines the difference between experimental and analytical results at each point, thus it is sensitive to both the location and magnitude of the differences between two distributions. In a typical K-S test, the cumulative difference between two distributions is used to calculate the Kolmogorov-Smirnov statistic (K-S), a scalar quantity between 0-1 that represents the maximum difference between the two distributions (Massey 1951). Hence, the K-S stat is a powerful tool that can be used to assess similarity (values of which are reported in **Table 4.3**). The reported K-S stat values show that experimental and analytical results are in good agreement, given the differences in both domains.

The calibrated parameter α for each specimen was used to plot the analytical envelopes for each specimen. Comparisons between the experimental and predicted analytical curves of grouted connections are depicted in **Figure 4.12** for representative specimens at embedment lengths of 4, 6, 8, and 10 d_b. Good correlation can be observed between the analytical and actual curves. An important observation is that the analytical predictions of the horizontal branch, attained after the maximum bond stress was achieved, was improved at longer embedment (8 and 10 d_b).
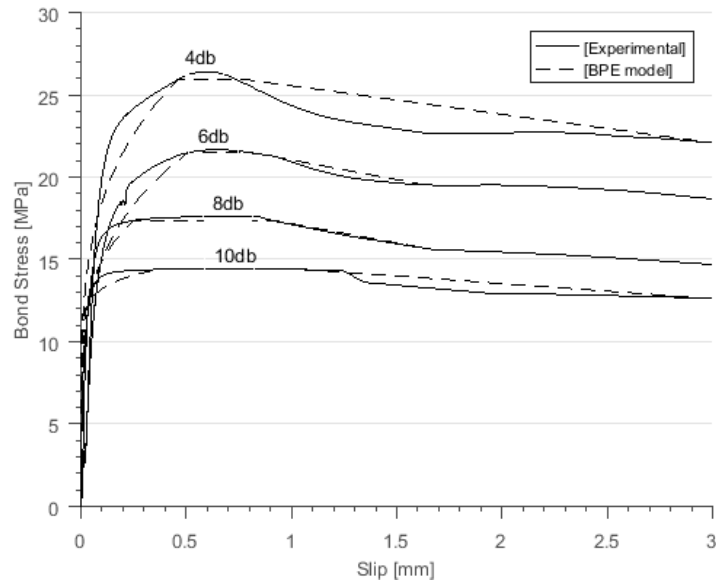
Figure 4.12: Experimental results vs analytical predictions of grouted specimens based on the BPE model.

Analytical results of the concrete specimens showed that the parameter α fell in the range of 0.25 to 0.49 with a mean value of 0.34. Comparable grouted specimens had a range of 0.18 to 0.26 and a mean value of 0.18. The comparatively higher values recorded for parameter α indicate a reduction in the stiffness of the ascending branch for concrete specimens. Grouted specimens had a steeper ascending branch despite the grout's lower compressive strength. This is believed to be due to the duct's pressure, which effectively restrained the grout and augmented the bond capacity.

4.4   IMPLEMENTATION AND DISCUSSION

Under the current practice, the design of grouted connections adheres to the model used by the ACI 318-14 following the development of reinforcing bars in tension. Several design equations have been proposed primarily by studies investigating grout connections in bridge bent applications (Steuck et al. 2009; Matsumoto et al. 2008; Brenes et al. 2006). Such equations (**Table 4.1**) are empirical expressions with similar approach to the ACI 318-14, which was developed by Orangun et al. (1977) using statistical techniques. It is worth mentioning that under the current design procedures, a maximum confinement factor $\left(\frac{c_b + k_{tr}}{d_b}\right)$ of 2.5 is allowed for confined concrete, and a value of 1 is encouraged, which

yields more conservative results. A comparison between the predictions of these models is plotted in **Figure 4.13**.
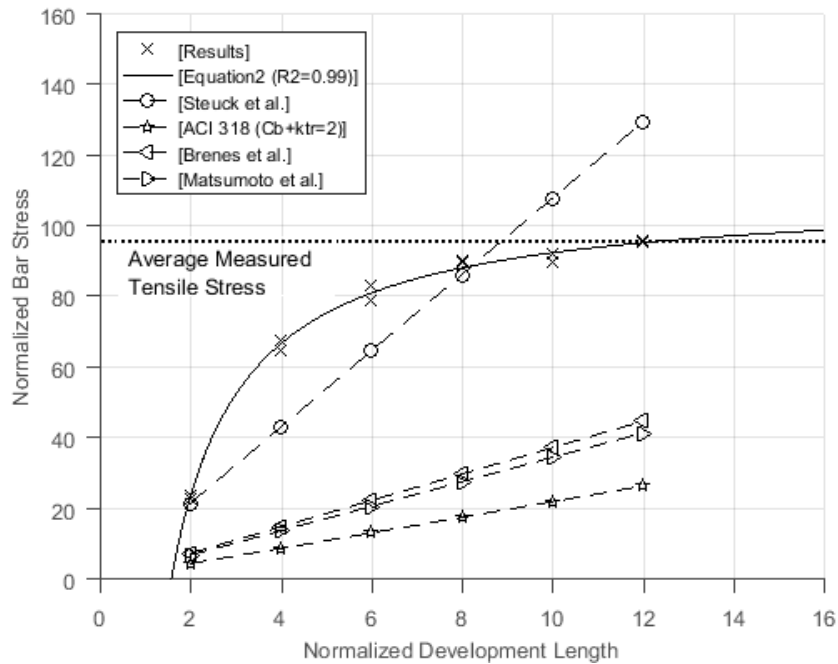
Figure 4.13: Predicted bar stress at corresponding development length of various models (**Table 4.1**).

One fundamental weakness can be observed; the developed models depict a linear relationship between the development length and the normalized bond stress, and consequently with the stresses developed in the bar. While these depictions yield simplified design expressions suitable for use by practitioners, they are essentially based on assuming uniform stress distribution along the length of developed bars, disregarding the nonlinear variations of the bond stress, which tends to increase with the increase in embedment.

To facilitate comparisons with previous equations, pull-out results from five embedment lengths (10 specimens) tested in this study were plotted and fitted using a power regression curve with 98% confidence, as shown in **Figure 4.13**. The goodness of fit was assessed by the R-squared value, which was 99%. The resulting equation takes the following:

$$\phi \, \gamma_s \, L_d = d_b \left(0.629 - 0.0057 \frac{f_s}{\sqrt{f_g{}'}} \right)^{-0.98}$$
(4.4)

where f_s is the stress in the steel connector in MPa; $f_g{}'$ is the grout compressive strength MPa; L_d is the predicted development length and γ_s is a steel stress normalization factor; ϕ is a safety factor taken as 1.2 to account for variability in the materials.

Only grouted specimens failing in pull-through mode were used in the development of **Eq. 4.4** (2, 4, 6, 8 and 10 d_b). Since this proposed equation was intended to describe development lengths that mobilize the tensile capacity of bars, it is interesting to note that the predictions of the equation at 12 d_b produced a normalized bar stress that was 0.31% less than the average recorded from the experimental data. The development length can be calculated at any desired stress level in the bar. **Figure 4.13** compares the predictions of the various models (**Table 4.1**) to that of **Eq. 4.4**. It can be observed that for a given development length, the level of stress prediction of the ACI 318-14 equation is greatly conservative. This is inherent from the fundamental difference between grouted connections and the behaviour of bars in concrete assumed in the ACI 318-14 model. The Steuck et al. (2009) model overestimated the development length requirements, even though a larger duct-to-bar diameter ratio was used. On the other hand, predictions from Brenes et al. (2006) and Matsumoto et al. (2008) underestimated the level of stress due to assumed failures which were not encountered in the present study. γ_s is given by **Eq. 4.5**:

$$\gamma_s = \frac{f_t}{605}$$
(4.5)

where f_t is the tensile strength of the used connector.

The factor γ_s accounts for variations in steel tensile strength and adjusts L_d accordingly. For example, if steel having an average tensile strength of 680 MPa was used, an embedment length of 16.32 d_b should be adopted to fracture the bar versus 12 d_b for the steel used in the present study.

4.5   SUMMARY AND CONCLUSIONS

An experimental program was conducted to explore the difference in behaviour between bars grouted in corrugated ducts versus that in concrete. Regression analysis carried out on the experimental results allowed deducing an empirical expression which takes into consideration factors influencing the bond. The results were further compared to relevant data retrieved from the open literature as well as the current ACI 318-14 equation. Moreover, the well-known BPE model was calibrated using the experimental bond stress versus slip envelopes. In light of the experimental and analytical effort presented above, the following conclusions can be drawn:

1. Under similar conditions and regardless of the level of stress in the bar, the bond of grouted connections did not fail in splitting. The failure was in the form of crushing of the grout keys between successive ribs, which is a favoured pull-through mechanism, being a form of a compression failure. Control bar-in-concrete specimens rather suffered split tensile cracks accompanied by pulling out of the bars.

2. The maximum average bond stress of grouted connections was consistently higher than that of its concrete counterpart for a given embedment length. The slip recorded after the maximum average bond stress attained was also lower, indicating a stiffer ascending branch. The softening branch of the bond stress-slip curve of grouted specimens after reaching maximum values exhibited more ductility with better frictional resistance than that for bars in concrete.

3. Varying the embedment length played a vital role in the load carrying capacity of specimens, but did not determine the failure mechanism. Strain levels in the dowel bars were higher at lower embedment lengths and comparable when the development length was 8 d_b. The full capacity of the bar was achieved at an embedment length of 12 d_b. At 6 d_b, the bars yielded but the bond failed in the strain hardening zone. At the same embedment length, the bar strain did not seem to affect the failure of grouted connections, yet it had a detrimental effect on the failure of its concrete counterpart.

4. Predictions of the calibrated BPE model yielded satisfactory agreement with the experimental results. Values of the parameter α for grouted connections indicated a consistently stiffer response as compared to that for the bar-in-concrete counterpart.

5. A design equation was obtained using regression analysis of experimental results. The equation was able to predict the behaviour at 12 d_b with favourable accuracy. This equation takes into account the compressive strength of the grout, tensile strength of the bar, and variations in the ultimate strength of the bars. The use of this equation is limited to the dimensions and mechanical properties of the specimens used in this study.

4.6   FURTHER RESEARCH

The purpose of the present study was to acquire an enhanced understanding of the characteristic behaviour of grouted connections used in precast wall applications under monotonic tensile loads. The cyclic behaviour and subsequent bond deterioration should further be explored. Results from such studies should either confirm the validity of **Eq. 4.4** or modify it to account for seismic effects. This study was conducted under the assumption that the bond of grouted connections shares the same dependencies as bars in concrete. However, it was observed that the confinement effect provided by the corrugated duct and the failure mechanisms differed substantially from that of the bar-in-concrete counterpart. A dedicated study to investigate this has been undertaken by the authors. This study should lead to the development of numerical and analytical tools that can serve for conducting a parametric investigation to examine those factors known to influence bond.

4.7   REFERENCES

Achillides, Z. & Pilakoutas, K., 2004. Bond Behavior of Fiber Reinforced Polymer Bars under Direct Pullout Conditions. *ASCE Journal of Composites for Construction*, 8(2), pp.173–181.

ACI Committee 318, 2014. Building Code Requirements for Structural Concrete and Commentary. *American Concrete Institute, Farmington Hills, MI, USA*, pp.1–519.

ACI Committee 408, 2003. Bond and Development of Straight Reinforcing Bars in Tension. *American Concrete Institute, Farmington Hills, MI, USA,*, pp.1–49.

Ashtiani, M.S., Dhakal, R.P. & Scott, A.N., 2013. Post-yield bond behaviour of deformed bars in high-strength self-compacting concrete. *Construction and Building Materials*, 44, pp.236–248.

ASTM 370, 2014. Standard Test Methods and Definitions for Mechanical Testing of Steel Products. *American Society for Testing and Materials*, 01.03, pp.1–50.

ASTM C39, 2016. Standard Test Method for Compressive Strength of Cylindrical Concrete Specimens. *American Society for Testing and Materials*, 04.02, pp.1–7.

ASTM C469/C469M-14, 2014. Standard Test Method for Static Modulus of Elasticity and Poisson's Ratio of Concrete in Compression. *American Society for Testing and Materials*, 04.02, pp.1–5.

ASTM C496/C496M, 2011. Standard Test Method for Splitting Tensile Strength of Cylindrical Concrete Specimens. *American Society for Testing and Materials*, 04.02, pp.1–5.

Baena, M. et al., 2009. Experimental study of bond behaviour between concrete and FRP bars using a pull-out test. *Composites Part B: Engineering*, 40(8), pp.784–797.

Brenes, F.J., Wood, S.L. & Kreger, M.E., 2006. Anchorage Requirements for Grouted Vertical-Duct Connectors in Precast Bent Cap Systems. In *Texas Department of Transportation Technical Report No. FHWA/TX-06-4176-1*. pp. 1–251.

Comite Euro-International Du Beton, 1993. *CEB-FIP Model Code 1990*,

Cosenza, E., Manfredi, G. & Realfonzo, R., 1997. Behavior and Modeling of Bond of FRP Rebars to Concrete. *Journal of Composites for Construction*, 1(2), pp.40–51.

Einea, A., Yamane, T. & Tadros, M.K., 1995. Grout-Filled Pipe Splices for Precast Concrete Construction. *PCI Journal*, 40(1), pp.82–93.

Einea, A., Yehia, S. & Tadros, M.K., 1999. Lap splices in confined concrete. *ACI Structural Journal*, 96(6), pp.947–955.

El-Hacha, R., El-Agroudy, H. & Rizkalla, S.H., 2006. Bond Characteristics of High-Strength Steel Reinforcement. *ACI Structural Journal*, 103(6), pp.771–782.

Eligehausen, R., Popov, E.P. & Bertero, V. V., 1982. Local bond stress-slip relationships of deformed bars under generalized excitations. In *Proceedings of the 7th European Conference on Earthquake Engineering*. Athens, Greeze, pp. 69–80.

Ganesan, N., Indira, P. V. & Sabeena, M. V., 2014. Bond stress slip response of bars embedded in hybrid fibre reinforced high performance concrete. *Construction and Building Materials*, 50, pp.108–115.

Marchand, P. et al., 2015. Bond behaviour of reinforcing bars in UHPFRC. *Materials and Structures*, 49(5), pp.1979–1995.

Massey, F.J., 1951. The Kolmogorov-Smirnov Test for Goodness of Fit. *Journal of the American Statistical Association*, 46(253), pp.68–78.

Matsumoto, E.E. et al., 2008. Development of a precast concrete system. *PCI Journal*, 53(3), pp.74–86.

Orangun, C.O., Jirsa, J.O. & Breen, J.E., 1977. A Reevaluation of Test Data on Development Length and Splices. *Journal of the American Concrete Institute*, 74(3), pp.114–122.

Raynor, D.J., Dawn, E.L. & Stanton, J.F., 2002. Bond-Slip Response of Reinforcing Bars Grouted in Ducts. *ACI Structural Journal*, 99(5), pp.568–576.

El Refai, A., Ammar, M. & Masmoudi, R., 2015. Bond Performance of Basalt Fiber-Reinforced Polymer Bars to Concrete. *ASCE Journal of Composites for Construction*, 19(3), pp.1–12.

Steuck, K.P., Eberhard, M.O. & Stanton, J.F., 2009. Anchorage of large-diameter

reinforcing bars in ducts. *ACI Structural Journal*, 106(106), pp.506–513.

Tastani, S.P. & Pantazopoulou, S.J., 2010. Direct Tension Pullout Bond Test: Experimental Results. *Journal of Structural Engineering*, 136(6), pp.731–743.

Tastani, S.P. & Pantazopoulou, S.J., 2013. Reinforcement and concrete bond: State determination along the development length. *ASCE Journal of Structural Engineering*, 139(9), pp.1567–1581.

Chapter 5

5 EXPERIMENTAL AND ANALYTICAL STUDY ON PRECAST CONCRETE DOWEL CONNECTIONS UNDER QUASI-STATIC LOADING

5.1 INTRODUCTION AND BACKGROUND

Grouted connections are composite connections often used to connect a variety of precast concrete elements. The connection is comprised of a large-diameter reinforcing bar grouted into a corrugated duct, bridging the horizontal joint between two vertically stacked walls. Grouted connections provide a straight force path extending along the height of a precast wall, reducing the risk of brittle failure. Two of the most common schemes of these connections are illustrated in **Figure 5.1,** with detail 1 being the most prevalent. It is shown that bond is the main mechanism through which grouted connections achieve composite action.

WALL PANEL

GROUT PORT

HIGH STRENGTH
NON-SHRINK GROUT

GROUT OR
CONCRETE

CORRUGATED DUCT

Ld

PRECAST SLAB

SHIM AND DRY-PACK

MECHANICAL
COUPLING DEVICE

CONTINUOUS BAR

Detail 1

SPLICING BAR

Ld

CONTINUOUS BAR

Detail 2
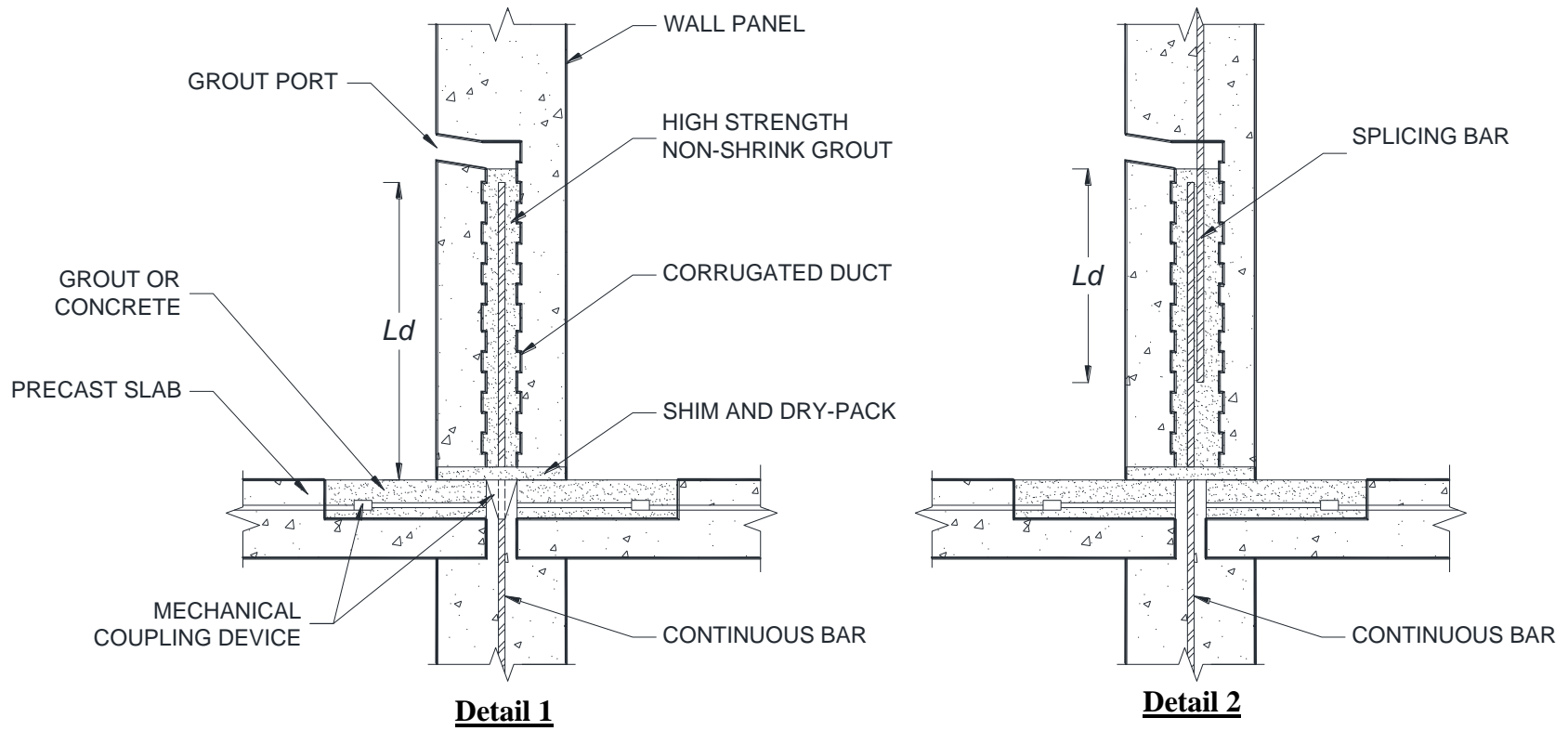
Figure 5.1: Common schemes of grouted connections used in precast walls.

Currently, grouted connections are designed in accordance with the recommended development length in tension of ACI 318-14 (Sections 25.4.2.3), which treats the connection as a bar-in-concrete scheme. A recent study questioned the efficacy of this assumption and showed that grouted connections did not suffer sudden splitting failures owing to the passive confinement effect of the duct (Elsayed & Nehdi 2017). In the absence of dedicated design provisions that reflect the composite action between the corrugated duct and the grout, designers and precast fabricators tend to over-design these connections, thus increasing field grouting operations. For example, the recommended development length of a 25-mm bar is typically 1200 mm for a concrete with a compressive strength, f_c' of 27 MPa. Such excessive grouted lengths could result in a wall panel with reduced stiffness because excessive deformations can result in spalling of the concrete along the length of the corrugated duct (Seifi et al. 2015). Despite its extensive use in precast wall structures, a dearth of information on grouted connections currently exists in the open literature, particularly under cyclic loads.

For instance, a single study was found in the open literature directly addressing this type of connection under cyclic loading. This investigation conducted by Raynor et al. (2002) studied grouted connections typically used in hybrid precast frames (small cover/diameter ratio). The specimens were subjected to a constant amplitude and variable displacement history. The bars had short embedment and the specimens were sufficiently confined. Their experimental results indicate that bond stresses due to cyclic loads are 10 to 70% less than those from monotonic loading, depending on the level of slip. It was shown that grouted connections behave differently from their bar-in-concrete counterparts. However, the reported data in this study were mostly qualitative and lacked experimental evidence on the real failure mechanisms.

Other studies on precast walls having grouted connections briefly reported on some behavioural aspects of these connections. For example, Seifi et al. (2015) tested under cyclic loading precast walls having grouted connections that use 16 mm bar and a grouted length of 37.5 d_b. The panels did not suffer premature failure and displayed favourable ductile behaviour characterized by panel sliding via yielding and elongation of the connection reinforcement. Other studies acknowledged the ductility and favourable energy

dissipation of grouted connections. However, large embedment lengths were used in such studies and no information pertaining to the bond of the connections was reported (Kang et al. 2013; Peng et al. 2015; Pang et al. 2010).

When a deformed bar is pulled/pushed under a cyclic load, adhesion is first lost, then mechanical bearing of the ribs is the primary mechanism of bond. The line of action of the bearing force resultant is approximately 30° (ACI Committee 408.2R 2012). This value strongly depends on various influential parameters, including the geometry of the lugs, confinement and the characteristics at the cement-aggregate interface. The exact value of θ is not known and remains a matter of great contention in the open literature. This concept was originally proposed by Lutz & Gergely (1967) and experimentally verified by others. For example, Cairns & Jones (1996) observed an inclination angle of 45°. Similar observations were made by Goto (1971), who observed that the initiation of cracks at the bar-concrete interface occurs at an angle of approximately 60°. More relevant experimental studies on precast concrete connections reported similar findings. For example, Steuck et al. (2009) reported conical grout break-out failures forming an angle of 45- 60° with the longitudinal axis of the bar in grouted connections. Ameli & Pantelides (2017) and Parks et al. (2016) reported similar break-outs with an angle of 45° in grouted splice sleeves.

The amount of damage accumulation is strongly dependant on the strain range of the cycles and the type and rate of loading (RILEM TC 65-MDB 1986; Shah & Chung 1986). The escalating slip due to constant amplitude cyclic loading decreases after the first few cycles. According to the Palmgren-Miner Hypothesis, the relationship between damage accumulation and number of cycles is linear at a certain load level. To further induce slip, loading should approach or exceed that in the previous cycle (Balzas 1986; ACI Committee 408.2R 2012). Transverse reinforcement can delay the occurrence of splitting failures resulting from cyclic loads. If sufficient restraining action is provided, the failure can shift from splitting to pull-out failure (Eligehausen et al. 1982b; Stavridis et al. 2013). The relationship between the anchored length of the bar and the number of cycles to pull-out is not understood quantitatively. Per the ACI Committee 408.2R (2012) guidelines, the anchored length is proportional to the total number of cycles required to achieve a pull-out failure.

Considering the current knowledge gaps and lack of data, the cyclic behaviour of grouted connections is explored in the present study through a carefully designed experimental methodology. The primary objectives are fourfold: i) devise an experimental scheme that eliminates the spurious effects known to be associated with bar bond testing; ii) explore the cyclic behaviour of grouted connections under realistic specimen and loading conditions; iii) provide quantitative evidence on the confinement of the corrugated duct and exploit this information to calibrate a frictional model; and iv) develop an empirical equation capable of predicting the capacity of the connection under a desired level of stress in the dowel and compare it with a similar model developed by the authors for grouted connections under monotonic loading (Elsayed & Nehdi 2017).

5.2   EXPERIMENTAL SETUP

In the present study, the behaviour of grouted connections under cyclic loading was explored under realistic field conditions. The novel specimen form presented in this study was designed to accurately reflect the state of stress arising in grouted connections in the critical zones of precast shear walls. A total of 16 specimens were tested. The effects of changing the embedment length and wall thickness of the duct were investigated. Two identical specimens were tested for every set of parameters to ensure reproducibility of the data. The average of results on the two specimens was used in the analysis. Details on the materials, specimens, instrumentation and loading are provided in subsequent sections.

5.2.1   Materials Testing

Tests performed on the materials were done as per corresponding ASTM standards. The concrete used in the study was manufactured and placed in a precast production facility and was subject to strict quality control protocols. The mechanical properties of the concrete and grout were assessed using ASTM C39 (2016) for compressive strength; ASTM C496/C496M (2011) for splitting tensile strength; ASTM C469/C469M-14 (2014) for modulus of elasticity. The mixture proportioning and mechanical properties of the concrete and grout are reported in **Table 5.1** and **Table 5.2**, respectively. The average compressive and tensile strengths of the concrete were 61.6 and 5.7 MPa, respectively. The grout used was a proprietary non-shrink cementitious mixture with average compressive

and tensile strengths of 39.9 and 6.3 MPa, respectively. It should be noted that the grout compressive strength was achieved from cylinders constructed based on actual field observations made by the authors from a number of precast wall site visits. An identical mix was reproduced in the lab to be reflective of actual field conditions.

Table 5.1: Concrete mixture proportions

Mixture Constituents	Per 1 m^3
Concrete	
Grey Type 30 Cement	435 kg
Sand	842 kg
14-mm round aggregate	842 kg
Water	200 L
Air	5%
Air Entraining agent/lubricant	20 ml/100 kg of cement
High Range Water Reducer	630 ml/100 kg of cement
Total	2,322 kg
Grout	
Proprietary non-shrink high-strength formulation conforming to ASTM C1107.	

Table 5.2: Mechanical properties of concrete and grout

Material	Age	Compressive Strength (MPa)	Tensile Strength (MPa)	Young's Modulus (MPa)	Poisson's Ratio
Concrete	7	53.7	5.1	26075	0.255
	28	61.6	5.7	26036	0.234
Grout	7	38.4	4.5	20712	0.229
	28	39.3	6.3	22713	0.235

All metallic materials were tested to determine their tensile capacity according to the ASTM 370 (2014). The dowel bars consisted of Grade 400, 25.4 mm diameter, No. 8 reinforcing bar with an average measured yield strength of 524.5 MPa. Duct A was constructed by winding a 72.5 mm light-gauge steel strip into the cylindrical form of the duct. The end of the strip had a lip that interlocked with a successive strip over a length of 4 mm creating a crimped seam. Duct B had a similar construction, but the strip length was 28.9 mm and the overlapping had a length of 3 mm. The cross-sectional details of both types of ducts are illustrated in **Figure 5.2**. The sleeves had variable thicknesses (**Figure 5.2**) and an average tensile strength of 225.6 MPa. All metallic materials were sourced from the same supplier and from the same heat. Further details on mechanical properties are reported in **Table 5.3**.

Table 5.3: Mechanical properties of metallic materials

Bar Type	Yield Stress (MPa)	Tensile Strength (MPa)	Ultimate Strain (%)	Failure Strain (%)
Rebar	524.50	680.18	12.30	24.44
Sleeve (A & B)	225.59	244.62	10.0	20.0

Duct **A:** Thickness 0.6 mm

Duct **B:** Thickness 0.3 mm
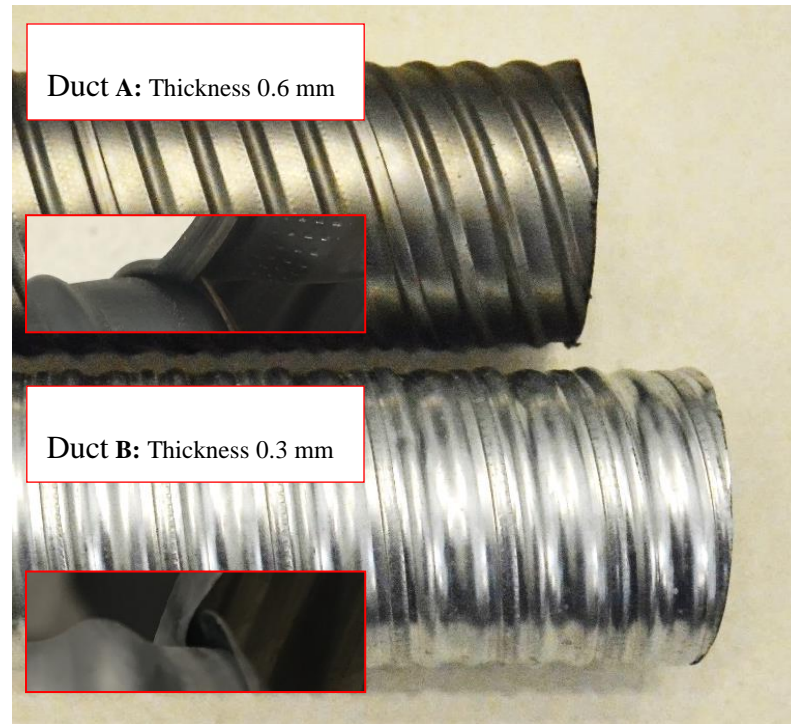
Figure 5.2: Corrugated ducts

5.2.2   Specimen Details

The test specimens were carefully designed to mimic field conditions pertaining to precast shear wall construction, as shown in **Figure 5.3**. The specimen was comprised of a reinforced concrete block that had dimensions of 254 x 254 x 406.4 mm where 254 mm is a typical width for precast shear walls. A 76.2 mm corrugated duct was placed concentrically in the middle of the specimen. To assist in the application of the load, four 16 mm threaded rods (ASTM A1035) were used to reinforce the block longitudinally. The bars were designed against breakout as per the requirements of the PCI handbook and placed 50.8 mm away from the corners of the specimen. The rods protruded 203 mm from the bottom of the specimen, while a 101-mm thick steel cradle was used to adapt the

specimen to the loading machine. Transverse reinforcement was in the form of 10 mm, closed branch, stirrups spaced 203.4 mm apart.
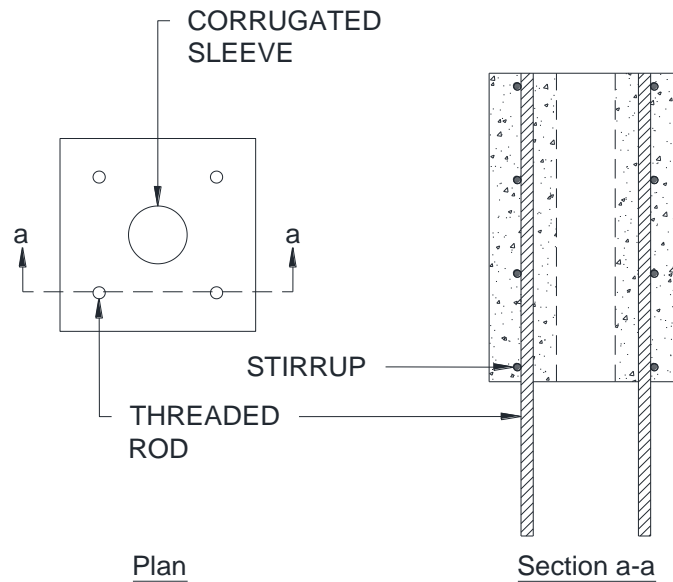
Figure 5.3: Details of the test specimen

The dowel bar used in this study was No. 8. The bars were de-bonded by wrapping it with 2-mm thick polystyrene wrap. The bonded length varied depending on the embedment length of the specimens (4, 6, 8, 10, 12, 14 and 16 d_b embedment were considered in this study). The embedment lengths were chosen such that they allow for the assessment of the elastic and inelastic bond response of the specimens. After placing of the de-bonded bars inside the duct, the non-shrink high strength grout was mixed and placed. The grout was mixed at low speed for 10 min and at high speeds for 5-min. Water (about 3.75 L) was added until a flowing consistency was achieved. Grouting was then done in the vertical position, similar to full-scale field grouting applications. Subsequently, the specimens were left to cure for 28-day at a temperature of 22 °C and relative humidity of 60%.

5.2.3   Test Setup, Instrumentation and Loading

After completion of the curing, specimens were mounted in a universal 630 kN MTS machine. This was done by adapting the specimen to the jaws of the machine via a high strength steel adaptor plate having a diameter of 280 mm and thickness of 101 mm. The

plate was used to allow the load to be distributed to the four threaded rods embedded in the specimen, as shown in **Figure 5.4**. The threaded rods were then fixed to the plate with the aid of lock washers after the plate was levelled in both directions. The use of the threaded rods to transmit the tensile force to the concrete (thus placing the grouted duct, concrete and the reinforcing bar in tension), subjected the specimen to a realistic stress state mimicking that encountered in the field. More importantly, it allowed the boundary conditions of the specimens to be free from any supplementary compressive fields (associated with classic pull-out tests) that may artificially enhance the bond of the bars.
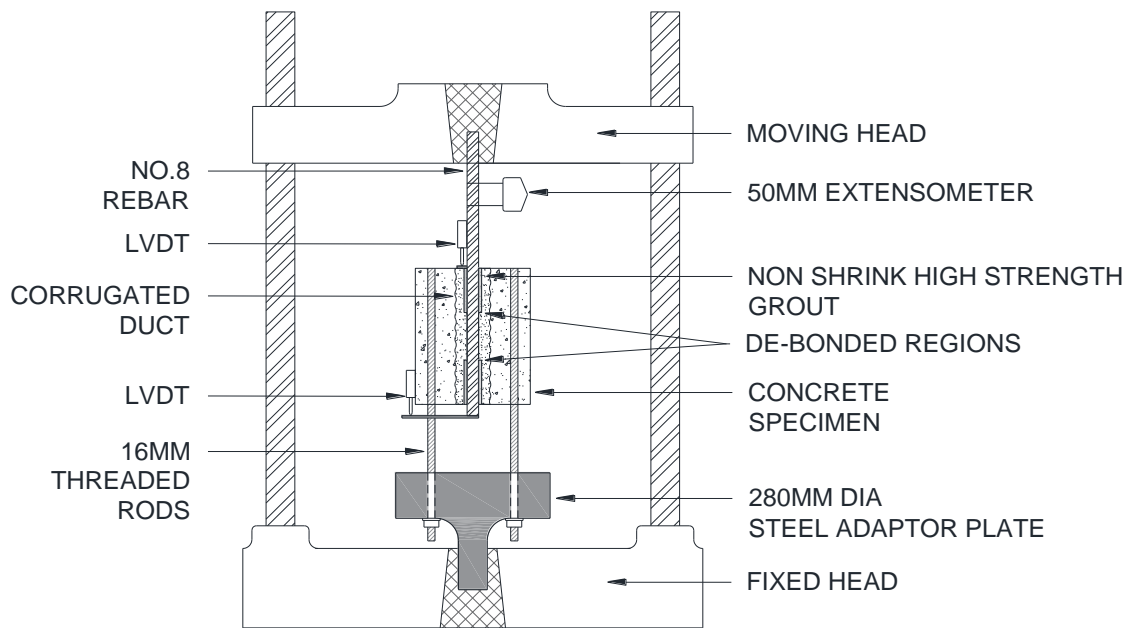
Figure 5.4: Test setup and instrumentation.

Two linear variable displacement transducers (LVDT) were used to capture the displacement of the bar at the active and passive ends. The strain in the bar was measured using an MTS extensometer with a sensitivity of 1×10^{-3} mm. Additionally, the extensometer reading was used to apply the load in strain (displacement) control. The horizontal strains in the corrugated duct were measured using two, 120-ohm, 5 mm strain gauges placed approximately 100 mm away from the active and passive ends. Readings from the strain gauges and LVDTs were recorded with an external DAQ machine with a frequency of 12 reading/second.

The load cycle adopted in the tests is shown in **Figure 5.5**. Since grouted connections are often used with a Type II mechanical coupling device capable of developing 100% the tensile capacity of the bar per the requirements of ACI Committee 318 (2014) as shown in **Figure 5.1 – Detail 1**, it is important that neither the coupler nor the composite duct fail below a required strain level. Hence, testing the connection under the same cycle, used to certify the coupling device, made sense from an integrity perspective. The threshold specifying the minimum acceptable performance of a Type II mechanical coupler is specified by the provisions of AC133-1209-R1 and allows exposing the connection to a series of low cycle excitations at critical strain values (AC133-1209-R1 2010). The cycle was modified such that no compression was applied unto the test specimen. The rationale for limiting the compression can be further understood by the consideration of **Figure 5.6**. Inherent from the nature of precast wall detailing practices, the connections are customarily placed 0.4-0.6 m away from the extreme fibre in tension or compression (away from the specially confined zone dark red zone in **Figure 5.6**). It is also customary in precast construction practices, to place a 25.4 mm layer of high strength (> 60 MPa) non-shrink dry pack grout, which is typically placed between the walls. Dependent on the location of neutral axis along the length of the wall, the connection will be subjected to limited compressive stresses (from in-plane flexure). The compressive demands on the connections are thought to be critical only if this dry pack layer has completely crushed. Even with such failure, allowing the panel to rotate so that the toe of the precast wall engages additional compression, is expected to exhaust the tensile capacity of the connection in tension. Hence, to allow the connection's behaviour to be assessed under realistic field conditions pertaining to precast shear walls, the cycles were adjusted so that no compression was applied unto the bars.
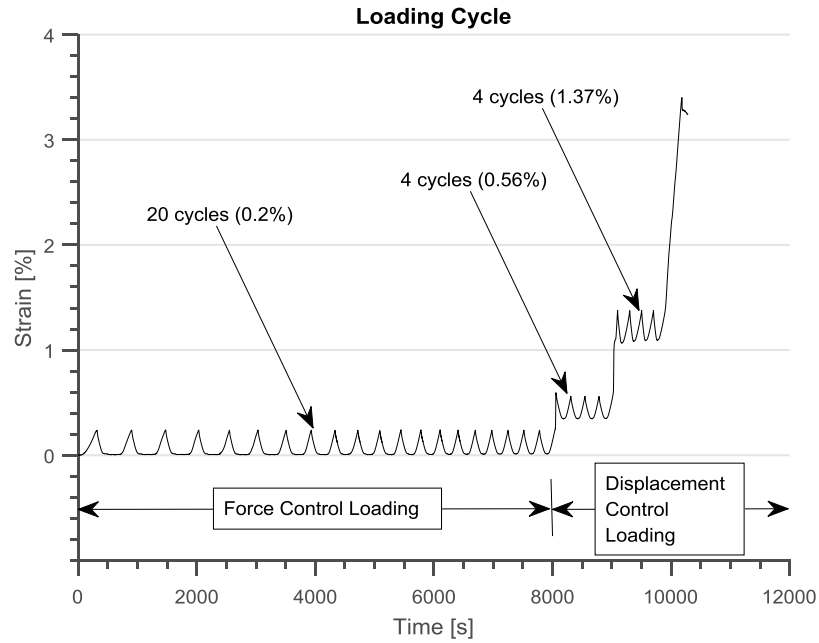
Figure 5.5: Loading cycle.
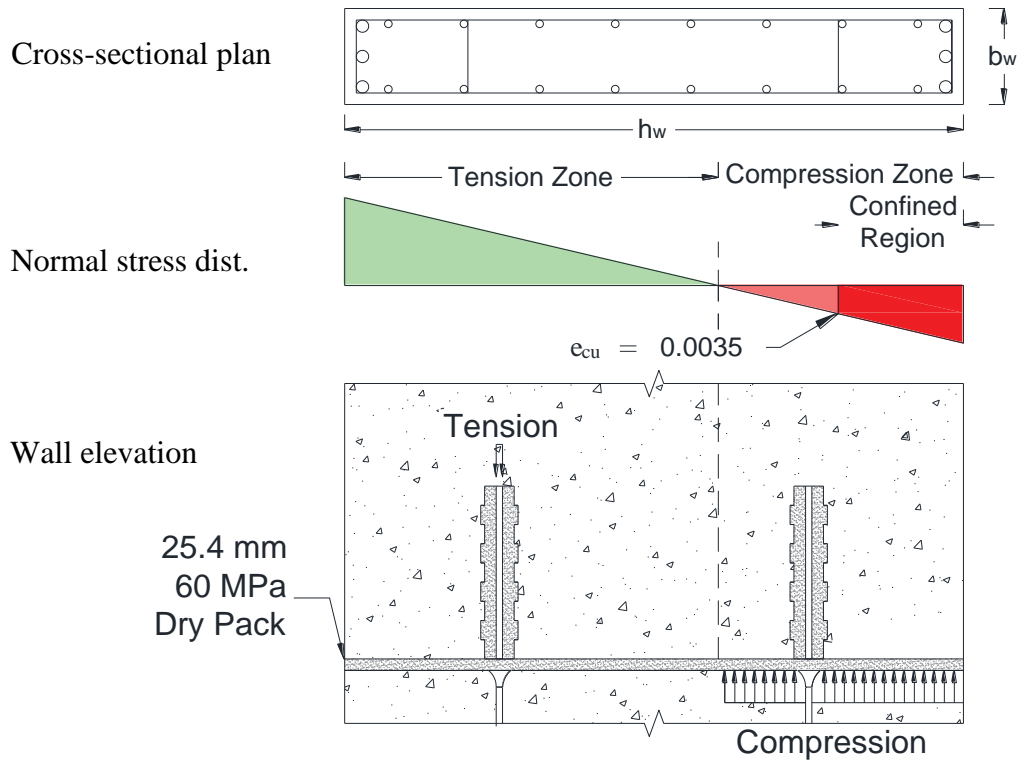
Figure 5.6: Compression in Dry Pack grout.

A total of 28 unidirectional cycles were applied to each specimen, as shown in **Figure 5.5**. The first 20 cycles were applied in load-control and reached up to 95% of the bar's yield stress. The next 8 cycles were applied under displacement-control up to strain levels of 200 and 500% of the yield strain, respectively. The bars were then pulled monotonically until failure. Low-cycle fatigue of the bars was not anticipated since: the strain cycles where below the limit of 0.85 ε_{ult}; the presence of a de-bonded region of the bar close to the loaded end, helped alleviate strain concentrations. It should be noted that the end of each cycle (**Figure 5.5**) corresponds to a zero-force condition and not to zero strain. All the cycles were applied with a rate of 0.5 mm/s. After failure, the test was halted until all instrumentation was removed, after which, the bar was pulled for the profile of the ribs to be examined.

5.3   EXPERIMENTAL RESULTS AND OBSERVATIONS

Two specimens were tested for each set of parameters to verify repeatability of the results. The average of the two measured responses was used for analysis purposes unless otherwise mentioned. A summary of the response of the tested specimens is presented in **Table 5.4**. The applied load was obtained directly from the built-in load cell of the MTS machine. The top displacement LVDT reading was corrected by subtracting the recorded elongation of the bar at each strain increment (Extensometer reading). The displacement at the unloaded end was obtained directly from the bottom LVDT (**Figure 5.4**).

Table 5.4: Test results of specimens

[1]Specimen Tag	Fail-ure	L1 (kN)	L20 (kN)	L28 (kN)	Lmax (kN)	Llast (kN)	FD1 (mm)	FD20 (mm)	FD28 (mm)	FDmax (mm)	FDlast (mm)	LD1 (mm)	LD20 (mm)	LD28 (mm)	LDmax (mm)	LDlast (mm)	f1 (MPa)	f28 (MPa)	fmax (MPa)
'C-4-D1'	P	165.0	-	-	165.0	165.0	0.3	-	-	0.3	0.3			[2] NA			325.6	-	326.0
'C-4-D2'	P	180.0	-	-	180.0	180.0	0.4	-	-	0.4	0.4	1.6	-	-	1.6	1.6	355.2	-	365.1
'C-6-D1'	P	228.1	-	`	228.1	226.4	0.4	-	-	0.4	1.0	1.0	-	-	1.0	2.0	450.2	-	450.2
'C-6-D2'	P	219.6	-	-	219.6	219.6	0.4	-	-	0.4	0.4	1.8	-	-	1.8	1.8	433.4	-	433.3
'C-8-D1'	P	228.1	222.7	-	228.1	222.7	0.0	0.6	-	0.0	0.6	0.9	1.6	-	0.9	1.6	450.2	-	451.3
'C-8-D2'	P	228.1	-	-	228.1	224.3	0.1	-	-	0.1	0.4	0.9	-	-	0.9	1.1	450.2	-	450.5
'C-10-D1'	P	228.1	227.7	243.0	303.6	303.6	0.0	0.2	0.4	1.7	1.7	0.8	0.9	2.9	6.1	6.1	450.2	479.6	599.2
'C-10-D2'	P	228.1	226.5	239.7	292.4	292.4	0.0	0.3	0.9	2.0	2.0	0.3	0.9	2.0	[2] NA		450.2	473.1	588.4
'C-12-D1'	P/SS	228.2	227.6	240.8	308.1	308.1	0.0	0.1	0.2	0.2	0.2	0.1	0.2	1.3	1.8	1.8	450.4	475.2	608.6
'C-12-D2'	P/SS	227.7	228.7	256.8	297.1	297.1	0.0	0.2	0.0	0.0	0.0	0.3	0.4	1.2	1.7	1.8	449.4	506.8	586.4
'C-14-D1'	P	228.0	228.4	-	249.0	249.0	0.0	0.9	-	1.7	1.7	1.0	1.5	-	1.6	1.6	450.0	-	492.2
'C-14-D2'	P/SS	228.2	228.6	240.6	303.9	303.9	0.1	0.2	0.4	0.2	0.2	0.3	0.4	1.4	2.0	2.0	450.4	474.8	599.8
'C-16-D1'	P/SS	228.3	228.2	248.3	296.7	296.7	0.0	0.6	1.3	1.4	1.4	0.2	0.2	1.7	2.7	2.7	450.6	490.0	585.5
'C-16-D2'	P/SS	228.3	228.0	244.3	314.1	314.1	0.1	0.2	0.2	1.1	1.1	0.3	0.4	1.3	3.6	3.6	450.6	482.2	619.8
'C-16-D3'	F	228.7	228.0	253.9	344.0	344.0	0.1	0.1	0.1	0.1	0.1	0.2	0.4	1.8	2.1	2.1	451.4	501.1	680.0
'C-16-D4'	F	227.6	228.2	240.8	339.3	339.3	0.1	0.1	0.2	0.2	0.2	0.1	0.2	1.3	1.8	1.8	449.2	475.2	670.3

Note: L1, L20, L28 = load at the peak of the 1st, 20th, and 28th cycle, respectively. FD1, FD20, FD28 and LD1, LD20, LD28 = displacement at the peak of the 1st, 20th, and 28th cycle at the free and loaded ends, respectively. P, SS and F = pull-out, duct splitting and bar fracture failures, respectively. f_1, f28, fmax = stress corresponding to 1st cycle, 20th cycle, and maximum;

[1] C refer to Cyclic load; *6, 8, 10, 12, 14, and 16* refer to the bar anchored length, respectively; **D refers** to Grade 60 rebars

[2] NA refer to equipment failure

[3] Specimen C-14-D1 first test was aborted after 24 cycles due to slippage of the Extensometer for which the test had to be repeated.

The specimen label is as follows: the first character represents the type of loading (C for cyclic). The second numeral represents the embedment length (4, 6, 8, 10, 12, 14 and 16 d_b). This was followed by a character that represents the type of bar used (D for deformed steel rebar). The subsequent numeral reflects the specimen number in its group (1 or 2). For example, C-14-D2 refers to the second deformed bar specimen with an embedment length equal to 14 times the bar diameter tested under cyclic load.

The average bond stress was used to compare the bond of different specimens. Although this does not represent an accurate depiction of the distribution of stresses along the embedment, most researchers reporting on bond often resort to this simplification. This approximation yields acceptable results in the range of 3-7 d_b (Tastani & Pantazopoulou 2010). Averaging the bond stresses over the embedment length usually gives an under-estimated figure of the local bond stresses. (Tastani & Pantazopoulou 2010) reported local bond stresses 4% to 38% higher than the average bond stress. ACI-408.2R-12 (ACI Committee 408.2R 2012) reports that local bond stresses can be 4 to 5 times the average stress. The assumption of average bond stress can be supported by three arguments: i) the ACI 318-14 equation for development length in tension, assumes uniform bond stress. Given that the local bond stresses are believed to be higher, a uniform bond stress assumption presents a conservative estimate (Orangun et al. 1977); ii) an accurate measurement of the local bond stresses cannot be determined without extensive instrumentation given the fact that bond cannot be measured directly; and iii) this assumption is encouraged by the ACI committee 408 which states that: "it is both convenient and realistic to treat bond forces as if they were uniform over the anchored, developed, or spliced length of the reinforcement" (ACI Committee 408 2003; ACI Committee 408.2R 2012). Thus, in the present study, the average bond stress was calculated via dividing the load by the surface area as show in **Eq. 5.1**:

$$U = \frac{F}{\pi \, d \, L_d} \tag{5.1}$$

Where F is the tensile load; d is the nominal bar diameter; and L_d is the bar embedment length.

5.3.1   Load vs. Displacement

The load and displacement vs. time responses for representative specimens are shown in **Figure 5.7**. Additionally, recorded values of the displacement measured after 1, 20, 28 cycles are reported in **Table 5.4**. Specimens with anchorages of 4, 6 and 8 d_b were all subject to elastic bar strains and all failed during the first 20 cycles, where the load varied between 0 and 228 kN (95% the yield stress). The overall trend for these specimens was similar in the sense that a stable progression of slip was observed as more cycles were imposed. Specimens with an embedment length of 4 d_b failed during the first cycle (monotonic envelope) with an average peak load of 172.5 kN. The increase in the load was accompanied by an increase in displacement at the loaded end, which started earlier during the loading procedure. Displacement at the unloaded end was not observed until the load peaked. The average displacement at the loaded and unloaded ends were 1.6 and 0.36 mm, respectively. At 6 d_b, 3 cycles were needed to fail the bars in pull-through mode. During the first cycle, a similar trend to their 4 d_b counter parts was observed. As the load was decreased during the descending branch of the first cycle, some irrecoverable slip was observed. The loaded end slip at the peak of the 1st, 2nd and 3rd cycles was 0.97, 1.59 and 1.61 mm, respectively. Most of the damage to the anchorage occurred during the first cycle. However, this damage stabilized during subsequent cycles and was not accompanied by apparent cracking inside the grout cylinder. Similarly, specimens with an anchored length of 8 d_b incurred damaged characterized by irrecoverable slip that progressed in an almost linear fashion. Yet, this damage was not observed until the 4th cycle, as shown in **Figure 5.7**. Comparison between the 6 d_b and 8 d_b specimens suggests that an increased anchorage length delayed the progression of slip as a longer embedment engaged additional ribs of bars. The grout flowing consistency and low elastic shrinkage characteristics are believed to be reasons that magnify this behaviour. However, this damage progression was not accompanied by a reduction in load before failure was manifested.
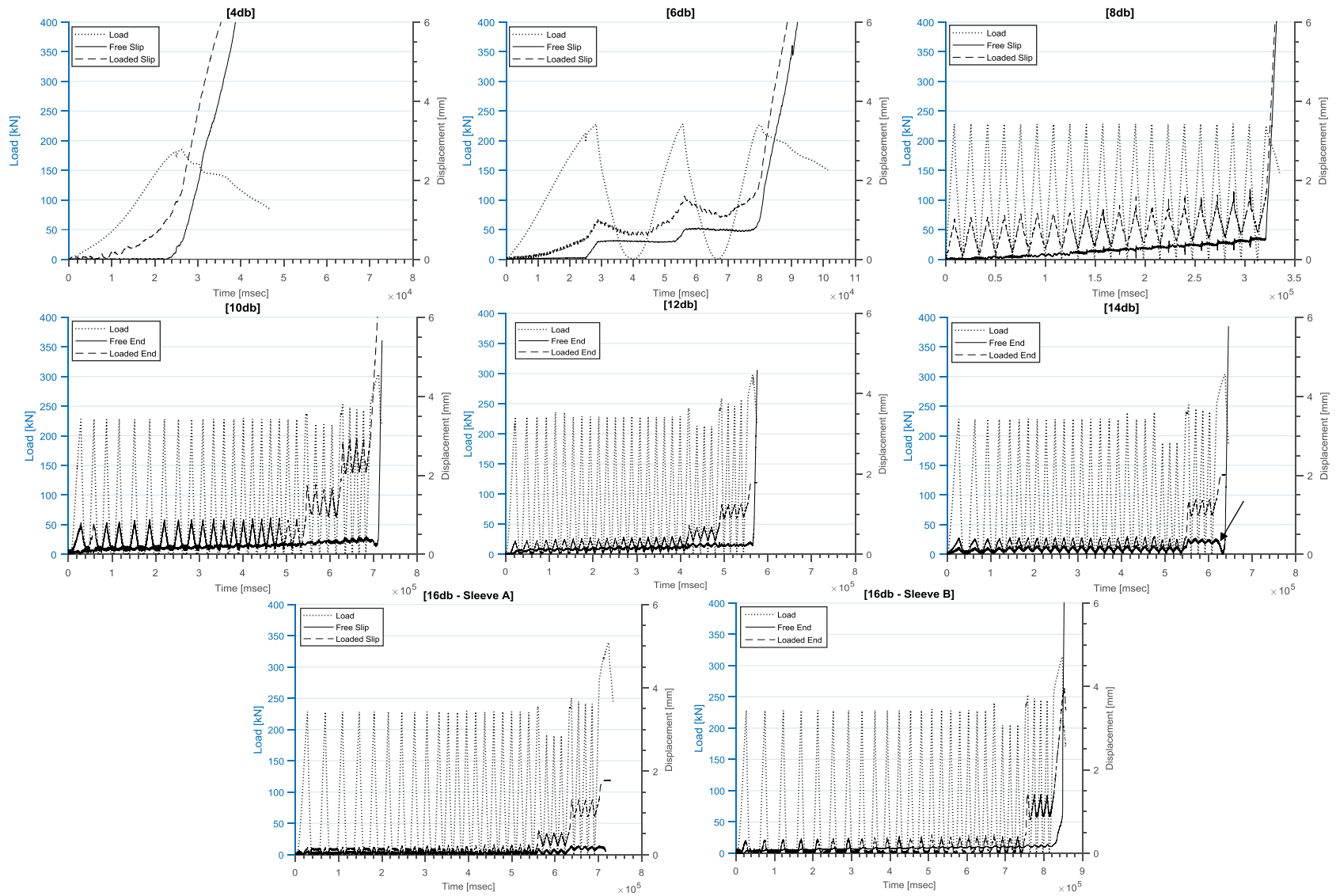
Figure 5.7: Load vs displacement responses at various embedment lengths obtained from the cyclic load tests.

The response of specimens embedded at 10, 12, 14 and 16 d_b mobilized an inelastic bar scenario (**Figure 5.7**). Examination of the response of these specimens indicates some similarities and differences compared to their elastic counterparts (4, 6, and 8 d_b). For instance, no degradation in the load carrying capacity of the specimens was observed during the test, except during the second 4 cycles of the procedure, which is due to bar yielding. Also, the progression of damage remained constant within the strain ranges of the cycles administered. The major observed difference between the response of elastic and inelastic bars was in terms of the rate of slip progression and the maximum slip domain.

At embedment of 10 d_b, the slope of the slip response exhibited stiffer response compared to its 8 d_b counterpart. This was also observed when the embedment length was 12 d_b, beyond which, the slope stiffness appeared to remain constant. All specimens embedded at 10, 12, 14 and 16 d_b equipped with a duct B failed at an average ultimate load of 302.7 ± 7.46 kN, at about 88% of the tensile strength of the bars, before duct rupture was observed. Specimens constructed with a duct A (**Figure 5.2**) displayed similar response to that of their corresponding duct B counterpart, except that they failed via bar rupture mobilizing the tensile capacity of the bar.

5.3.2　Failure Modes

The failure of representative specimens is illustrated in **Figure 5.7** and **Figure 5.8**. Specimens embedded at 4, 6, 8 and 10 d_b failed by pull-out through shearing of the grout keys between ribs. Considering these failures in light of the total number of cycles at failure gives indication to whether plasticity of the dowel bars influences the failure. Specimens with 4 d_b embedment failed via a pull-through mode at the first cycle (monotonic envelope). Specimens with 6, 8, 10 d_b embedment failed at an average number of cycles of 2.5 (95% f_y), 15 (95% f_y), 28 (500% ε_y), respectively. Similar failure could be observed at both the elastic and inelastic strains in the dowel bar. At 4, 6, 8 and 10 d_b, cracks were neither observed inside the grout cylinder near the active and passive ends, nor in the concrete blocks. At 12 d_b, no cracks were registered in the grout cylinder. Yet, large radial cracks started to from in the concrete block as the load exceeded 290 kN and approached the capacity of the specimen (300 kN), as observed in **Figure 5.8**. These cracks grew rapidly

in width, but did not propagate towards the unloaded end. This is believed to be due to the onset of splitting in the duct, which occurred along the crimped seam (**Figure 5.2**). This was confirmed when similar failures were suffered by specimens at 14 and 16 d_b, all of which failed by a mixed mode (pull-through + duct splitting), as shown in **Figure 5.9**. Rupture of the duct took place at very low slip levels and was observed only in the case of longer anchorages. From the trend of failures observed, the rupture was a result of the strain penetration, which was magnified when the last eight load cycles were applied. Once the rupture of the duct occurred, it led to extensive cracking and the formation of a plastic hinge around the location of the rupture as observed in **Figure 5.9**.
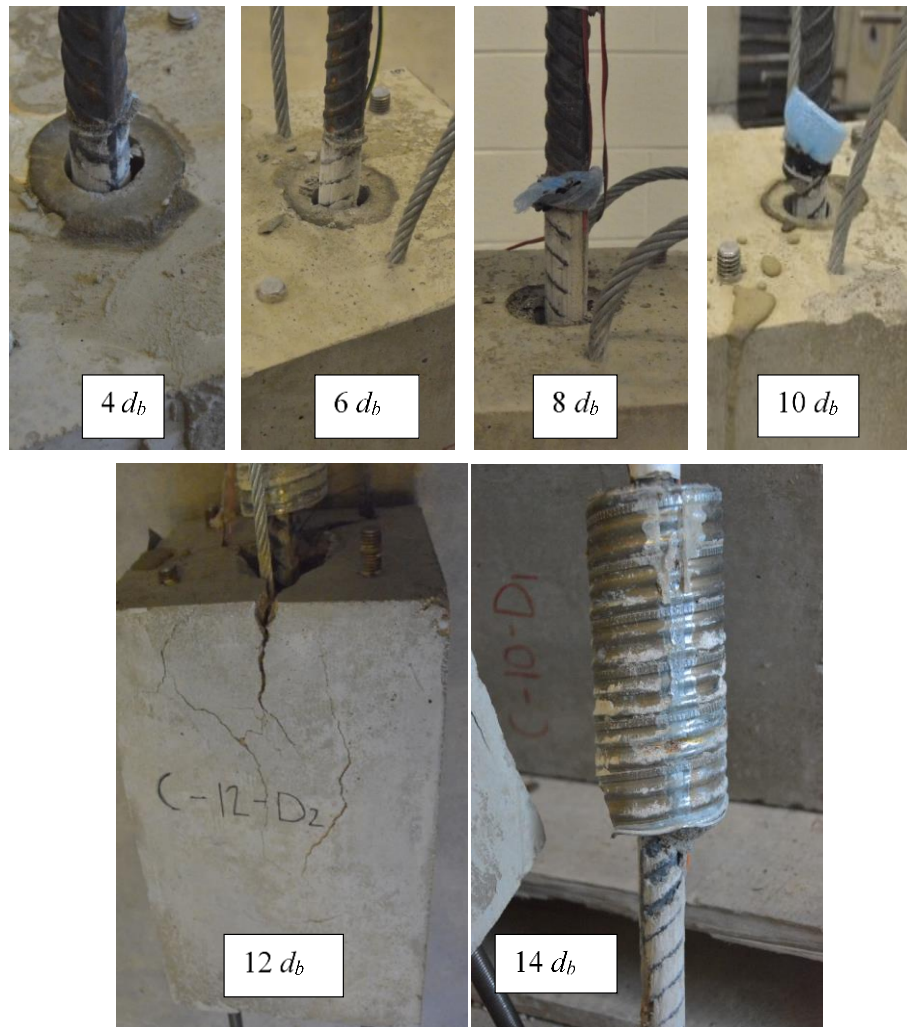
Figure 5.8: Rib profiles of failed specimens [from top left to right]: C-4-D1; C-6-D1; C-8-D2; C-10-D2; C-12-D2; C-14-D2.

his could also be captured through negative slip reading (due to rotation) at the unloaded ends (**Figure 5.7 Point A**). Examining **Figure 5.10**, the duct rupture is believed to be the result of a localized failure perpendicular to the seam due to the resultant of the tensile forces F_{res}. Two components contribute to F_{res}: a primary component resulting from the lateral expansion of the grout (F_1); and a secondary component from the direct pulling of the bar due to the composite action (F_2). The local loss in confinement can be observed in **Figure 5.8.** since partial cones appeared on the profile of the ribs where the duct rupture was characterized. Specimens equipped with duct A (C-16-D3-S_A – and C-16-D4-S_A) sustained all loading cycles and failed by fracturing of the bar at ultimate stresses corresponding to those reported in **Table 5.3**.

16 d_b (duct B)   Splitting   16 d_b (duct A)

Figure 5.9: [Left] Duct rupture (C-16-D2); [Center] Expanded grout as confinement is lost (C-16-D2); [Right] Additional confinement causing bar fracture (C-16-D4).
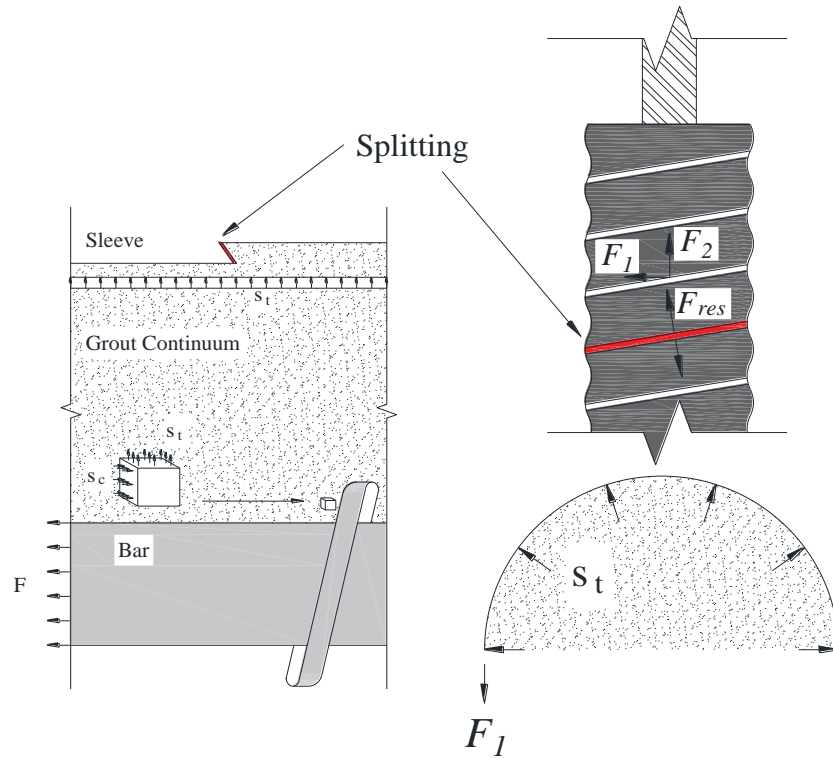
Figure 5.10: State of stress on an elementary strip of the duct.

5.3.3   Passive Confinement Effect

A typical load vs. duct strain response near the loaded end of a representative specimen is displayed in **Figure 5.11**. Duct strain values and corresponding stresses are given in **Table 5.5**. The present study can provide quantitative evidence of the confinement effect provided by the corrugated duct, which is only found in the literature in qualitative terms (Raynor et al. 2002). The values of the hoop strain in the duct can be beneficial in two ways: i) it gives the magnitude of the passive confining field providing restraint to the grout; and ii) reflects the level of damage in the grout since an increase in slip corresponds to an increase in the radial displacement of the grout near the bar. It is thus believed that an increase in the irrecoverable slip would be accompanied by a corresponding increase in the hoop tension in the duct, as can be observed in **Figure 5.11**. At the peak of the 1st and 20th cycles, the recorded duct strain was 1890 and 2480, respectively. This 31.2 % increase in hoop strain indicates grout damage. The overall trend of the specimens at different anchored lengths followed that of **Figure 5.11**, except that: i) at shorter anchored lengths, the measured peak

hoop strain was higher and decreased as the embedment length increased (**Table 5.5**); and ii) at longer embedment lengths, the increase in hoop strain (at the 20th cycle) was proportional to the increase in embedment. This was anticipated since the effect of yield penetrations increased slip at the loaded end (**Figure 5.7**). For long embedment lengths (10, 12, 14, and 16 d_b), the average duct strain at the end of the 28th cycle was approximately 50% more than that recorded at the 1st cycle. At 4 and 6 d_b anchorages, the corresponding confinement pressure generated by the duct was 20.7 and 16.6 MPa, respectively. This confirms previous findings in the literature suggesting that a confining stress equivalent to 0.25 f_c' can completely suppress splitting bond failures (Tastani & Pantazopoulou 2008). Similar observations were also made by the authors (Elsayed & Nehdi 2017) comparing grouted connections to bars in concrete prisms at 4 d_b under monotonic loads, attributing this to the duct confinement, although no measurements of the duct strains were reported.
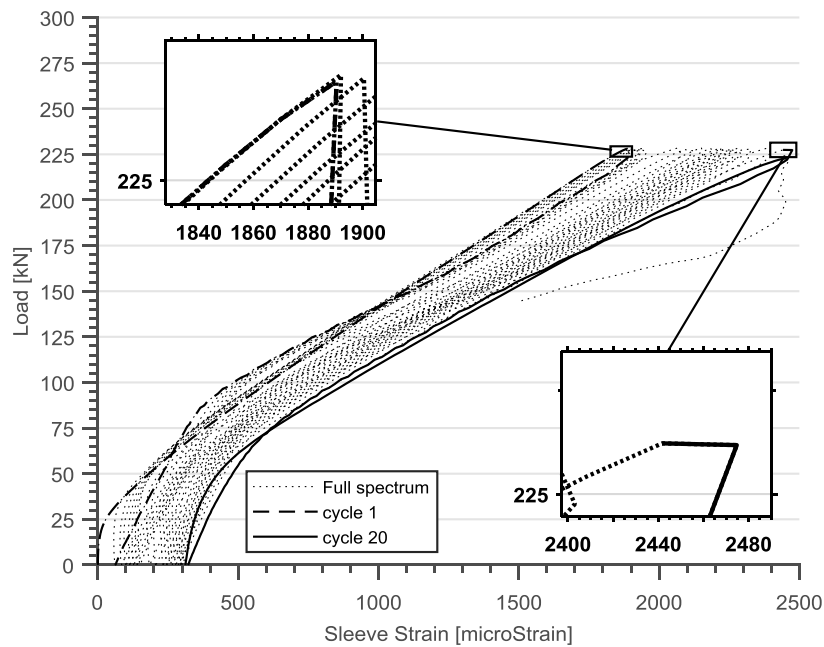
Figure 5.11: Load vs. hoop duct strain [specimen C-8-D1].

Table 5.5: Frictional model results

Specimen Tag	$\varepsilon_{s,max}$ (microStrain)	σ_{duct} (kN)	U_{model} (kN)	U_{exp} (kN)	Error (%)	R_d
'C-4-D1'	6800	19.28	22.55	20.38	-10.69	0.007
'C-4-D2'	6028	17.09	21.18	22.82	7.19	0.007
'C-6-D1'	4000	11.34	17.55	18.76	6.43	0.008
'C-6-D2'	3580	10.15	16.80	18.06	6.93	0.009
'C-8-D1'	2500	7.09	14.88	14.10	-5.47	0.012
'C-8-D2'	1910	5.41	13.82	14.08	1.81	0.010
'C-10-D1'	4227	11.98	17.96	14.98	-19.90	0.110
'C-10-D2'	2545	7.21	14.96	14.71	-1.66	0.110
'C-12-D1'	1730	4.90	10.18	12.68	19.71	0.130
'C-12-D2'	2097	5.94	10.66	12.22	12.74	0.100
'C-14-D1'	3443	9.76	12.41	8.79	-41.26	0.010
'C-14-D2'	1618	4.59	10.04	10.71	6.31	0.119
'C-16-D1'	2000	5.67	10.53	9.15	-15.13	0.100
'C-16-D2'	2294	6.50	10.92	9.68	-12.72	0.130
'C-16-D3'	1605	7.58	11.41	10.62	-7.42	1.000
'C-16-D4'	1332	6.29	10.82	10.29	-5.15	0.990

Note: $\varepsilon_{s,max}$ = peak strain in duct; σ_{duct} = peak confining stress; U_{model}= average bond strength (frictional model); U_{exp}= average bond strength from (experimental); R_d = ductility ratio

5.3.4   Ductility

When used in precast shear walls, grouted connections are designed and constructed to provide ductility to the assembly through the yielding of the bars crossing the horizontal joint. To assess this, a ductility ratio was used to compare the tested specimens and its values are given in **Table 5.5**. The ductility ratio was calculated per **Eq. 5.2** as follows:

$$R_d = \frac{\varepsilon_{max}}{\varepsilon_{ult}} \tag{5.2}$$

where ε_{max} is the peak strain developed in the bar; ε_{ult} is the coupon strain at failure (an average value of 2 coupons as given in **Table 5.3**).

Figure 5.12 exhibits the ductility ratio vs. embedment length of the tested specimens. Specimens at 4, 6, and 8 d_b embedment all failed at an average ductility ratio of 0.009 and COV 22.35%. These values were 0.115% and 3.2% when the anchored length was between 10 and 16 (duct B) d_b. The difference in ductility observed between these two groups of specimens was due to the flow of plasticity in the bars. Comparison of the specimens 10 to

16 d_b (duct B) to their 16 d_b (duct A) counterparts is possible since all such specimens endured the exact number of cycles, had similar failure modes, and failed under the same load (302.7 ± 7.46 kN). The ability of duct A in mobilizing the capacity of the bar (thus invoking a ductile failure) was directly related to the thickness of the duct, despite the corrugated duct's dis-continuity along their axial direction. Their behaviour was similar to those of cast iron splice sleeves (Haber 2013; Ameli & Pantelides 2017). Accordingly, when duct A is used, a fully ductile failure is possible between 10 and 16 d_b. This is yet to be confirmed in future work. Also, an increase in embedment by two bar diameters (from 8 to 10 d_b), increased the ductility ratio by approximately one order of magnitude, which is attributed to the non-linearity of the bond distribution between the two embedment lengths. Similar observations were reported by Bonacci (1994) considering the design of yielding anchorages, which suggests that the boundary between acceptable and nonacceptable anchorage occurs rather abruptly.
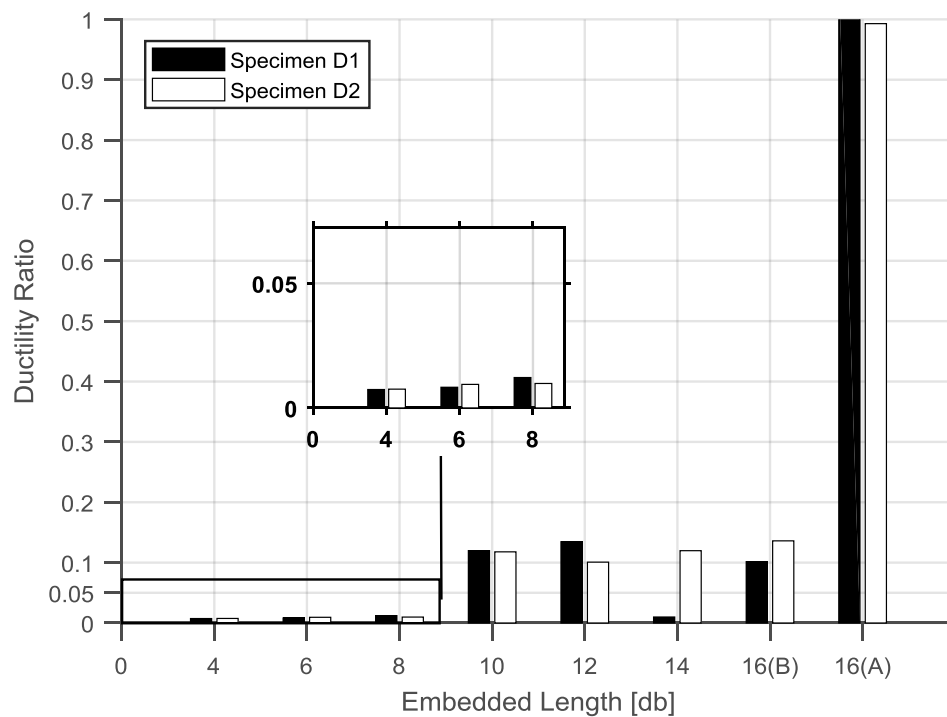
Figure 5.12: Ductility at different anchored lengths.

5.3.5   Effects of Induced Compression
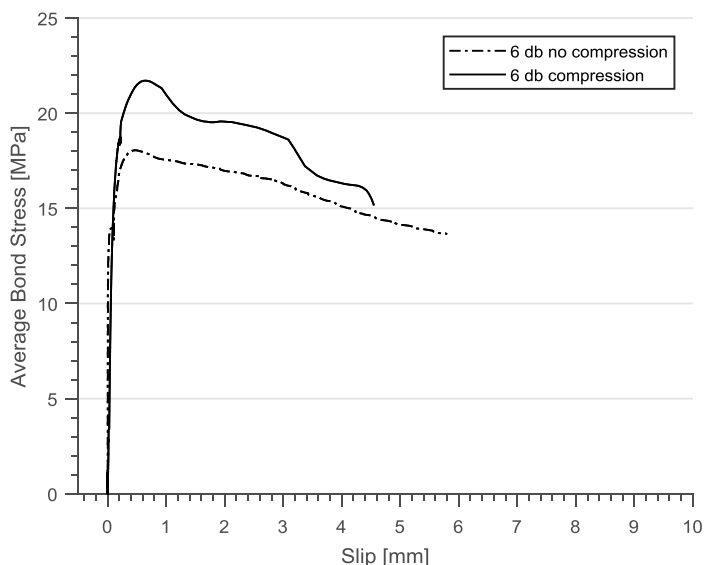
Figure 5.13: Comparison between results for 6 d_b grouted connections using the test setup shown in Figure 5.4 (no compression) and test setup shown in Figure 4.4 (compression).

To highlight the effects of the boundary conditions on the response of the tested specimen, a comparison between the results of 6 d_b specimens is made for the setup shown in **Figure 5.4** and **Figure 4.4.** The average bond stress versus free end slip is plotted in **Figure 5.13**. The maximum bond stress was 18.05 and 21.71 MPa for the non-compression and compression specimen, respectively. An increase of 20% was observed. Additionally, the slip at the onset of the bond strength was delayed for the compressed specimen as a result of the additional confinement. This observation further emphasizes the discussion on the influence of the specimen form on its bond response as mentioned in the preceding sections.

5.4   PREDICTIONS OF FRICTIONAL MODEL

One of the simplest models that describe the stress transfer in bonded regions is the frictional model described by Cairns & Jones (1996) based on a Mohr-Coulomb envelope. This model relates the average shearing stresses developed along the lateral surface of the bar (average bond stress) to two main components: i) the confining pressure with the coefficient of friction being the constant of proportionality; and ii) adhesion stresses (an

intrinsic property of the interfacial properties of the assembly). The model is given by **Eq. 5.3** as follows:

$$f_{bond} = \frac{2\mu}{\pi} f_{con} + f_{adhesion} \qquad (5.3)$$

where f_{bond} is the average bond strength; μ coefficient of friction; f_{con} is the confining stress; and $f_{adhesion}$ is the adhesion stress developed along the interface.

Before calibration of this expression, considering the equilibrium of forces along the anchored length of the bar is necessary to accurately estimate the model parameters. **Figure 5.14** shows a schematic illustration of an anchored bar of a grouted connection. The confinement stress f_{con}, is broken down into contributions from the grout cover, stirrups and duct pressure, as given by **Eq. 5.4**:

$$f_{con} = f_{sleeve} + f_{stirrup} + f_{cover} \qquad (5.4)$$

Where f_{sleeve} is the confinement pressure of the duct; $f_{stirrup}$ is the contribution to confinement from the stirrups; and f_{cover} is the hoop tension in the grout cylinder. From the equilibrium of forces (**Figure 5.14**), it follows that:

$$f_{sleeve} = \frac{2t_s E_s \varepsilon_s}{d_b} \qquad (5.5)$$

$$f_{stirrup} = \frac{0.33 A_{st} f_{st}}{d_b . s} \qquad (5.6)$$

$$f_{cover} = \frac{f_{t'} . c}{d_b} \qquad (5.7)$$

where t_s, E_s, and ε_s are the duct thickness, modulus of elasticity, and peak strain, respectively; A_{st}, f_{st}, s are the stirrup's cross-sectional area, yield stress, and spacing, respectively; $f_{t'}$ and c are the grout's tensile strength and cover thickness, respectively.
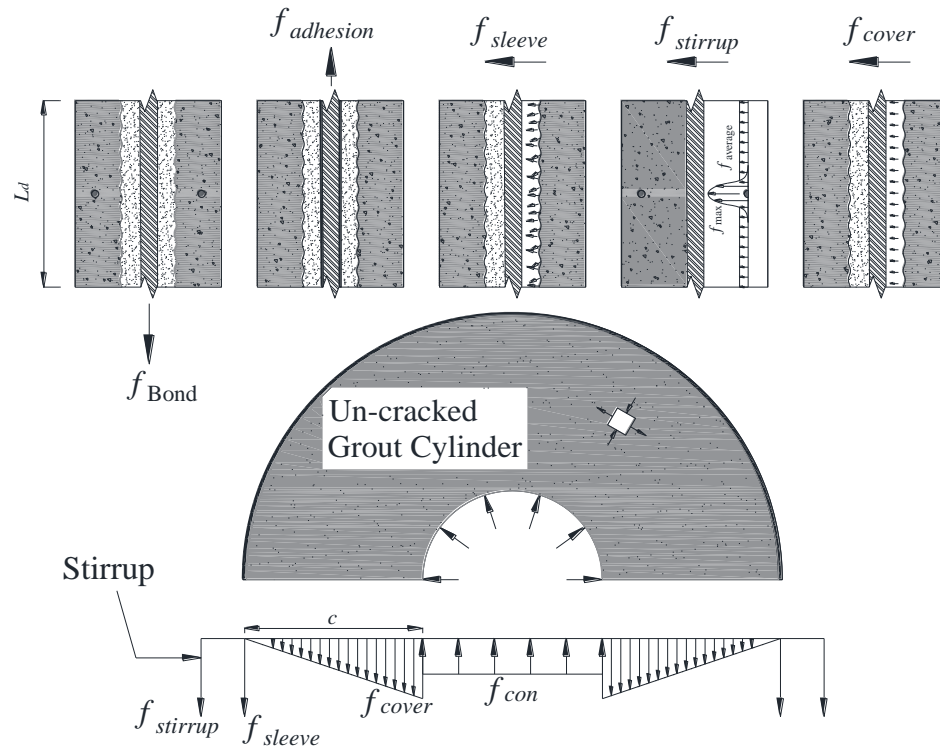
Figure 5.14: Free-body diagram of the components of the frictional model.

Values of μ are believed to be affected by the confining pressure and slip and could be estimated at 0.72 to 0.90 as reported by Malvar (1992) and Tastani & Pantazopoulou (2010). $f_{adhesion}$ is the interfacial shear stress (due to chemical interaction) and is believed to be in the range of 0.8 to 1 MPa (Malvar 1992; Tastani & Pantazopoulou 2010; Eligehausen et al. 1982a). The strain, ε_s was calculated as the peak recorded strain in the duct obtained from **Table 5.5**. The stirrup's parabolic distribution (**Figure 5.14**) was converted to a uniform compressive field equal to the third of the maximum stress averaged over the spacing of the stirrups, hence the term 0.33 in **Eq. 6**. The grout's tensile strength, $f_{t'}$ was taken from **Table 5.2** as 6.3 MPa.

The predictions of the calibrated frictional model are given in **Table 5.5**. Except for specimen C-14-D1 (check footnote [3] in **Table 5.4**), the estimations of the calibrated model are in good agreement with the experimental results up until an embedment of 8 d_b. Beyond this, non-linearity in the distribution of bond stresses became more pronounced and an averaged stress over the lateral surface of the bar tended to give crude results. This can be observed from the increase in the percentage of error reported in **Table 5.5**. Another

possible explanation of this disparity was attributed to the strain values, which are believed to be highly localized because of the complex geometry of the duct.

5.5   IMPLEMENTATION AND DESIGN

A recent study investigating the bond behaviour of grouted connections under monotonic loads proposed an empirical expression that can be used in designing the minimum embedment length of grouted connections to develop a certain stress level in the connector (Elsayed & Nehdi 2017). This proposed relationship has the following form:

$$\phi \, \gamma_s \, L_d = d_b \left(0.629 - 0.0057 \frac{f_s}{\sqrt{f_g'}} \right)^{-0.98} for \left\{ \frac{f_s}{\sqrt{f_g'}} < 100 \right. \tag{5.8}$$

where f_s is the stress in the steel connector in MPa; f_g' is the grout compressive strength in MPa; L_d is the predicted development length and γ_s is a steel stress normalization factor calculated as $\gamma_s = \frac{f_t}{605}$ where f_t tensile strength of the connector bar; ϕ is a safety factor taken as 1.2 to account for variability in the materials.

This equation was obtained by fitting the bar stresses (normalized by the square root of f_g') vs. the embedment length for ten identical specimens at five different embedment lengths. The specimens used were similar to those used in the present study. Only those specimens which failed in pull-through mode were considered. A similar approach was adopted in the present study and the experimental results were fitted with the same power regression function at 98% confidence interval. Both equations are shown in **Figure 5.15** and plotted against the experimental results. Considering the predications of **Eq. 5.8** versus the average normalized bar stress, it can be observed that when the embedment length was 4, 6 and 8 d_b, substantial differences existed between the model predictions and the experimental results due to the deterioration of the anchorage in response to the cyclic load. Moreover, the error in predictions seemed to diminish with increasing embedment length. The prediction error for the 10, 12, 14 and 16-B d_b specimens was 2.3, 0.1, 1.34, and 2.8 %, respectively. Since the design rationale for grouted connections is concerned with the prediction of a minimum embedment length which can invoke a fully ductile behaviour (i.e. tensile capacity of the

bar), **Eq. 5.8** was found to satisfy this criterion with reasonable accuracy, should the field conditions be similar to those encountered in this experimental study.

It should be noted that beyond the range of $\dfrac{f_s}{\sqrt{f_g{}'}} > 100$ (specimens 16-A), parameter γ_s should be used to adjust the embedment to an acceptable value of L_d capable of mobilizing the capacity of the bar. Based on the observations of this study, the use of **Eq. 5.8** is limited to a duct thickness of 0.6 mm.
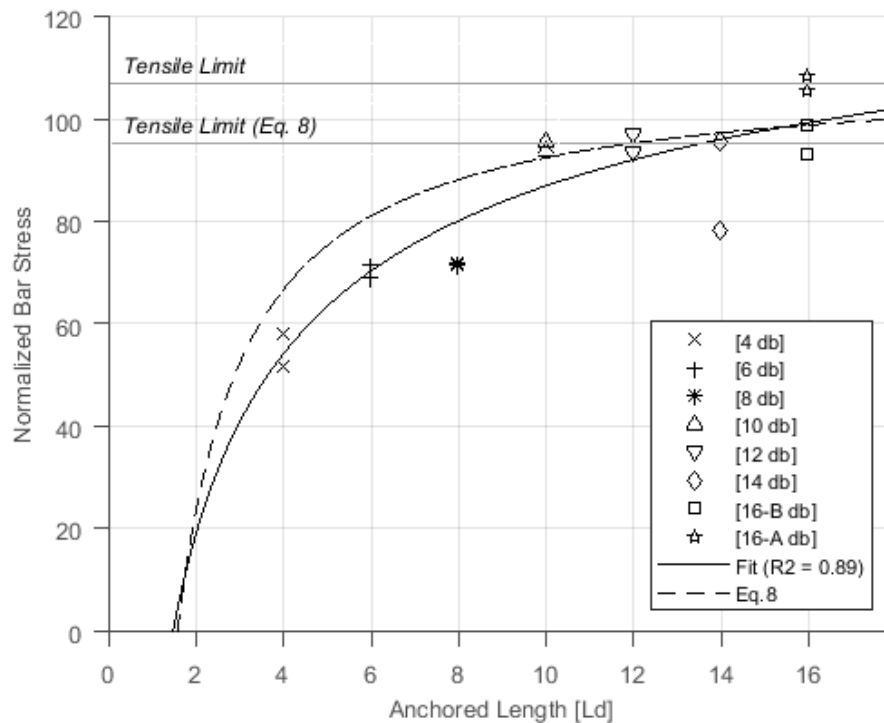
Figure 5.15: Normalized bar stress vs. embedment length.

5.6 SUMMARY AND CONCLUSIONS

This paper presents the findings of a novel experiment conducted to assess the bond behaviour of grouted connections under quasi-static unidirectional excitation. The experimental program consisted of testing 16 specimens under realistic field and loading conditions. The experimental scheme utilized was free from the common spurious effects associated with bond testing. The experimental results were used to calibrate the so-called frictional model, after estimation of the confinement stresses of the specimens. The results were then used to verify a design expression that can predict the required development

length based on a desired level of stress in the bar. Based on the experimental conditions presented above, the following conclusions can be made:

1- Under a unidirectional cyclic load, the damage deterioration observed was in the form of irrecoverable slip, which seemed to decrease substantially when the embedment length exceeded 8 d_b. Most of the damage was incurred in the first few cycles, after which constant irrecoverable slip propagated. No deterioration in the load carrying capacity of the specimens was observed at any anchored length. The load carrying capacity of the specimens at 10, 12, 14, and 16 d_b. was nearly identical and limited by the restraining effect of the duct.

2- The strain level in the bar had a detrimental effect on its slippage. Slippage decreased as the embedment increased due to the non-linearity introduced in the distribution of bond stresses.

3- The grout cylinder enclosed by the duct did not fail by splitting regardless of the anchored length of the specimens. Failure was consistently via shearing of the grout keys between the deformations of the bar. At an embedment length of 12 d_b and up to 16 d_b, the duct suffered sudden rupture along the seam close to 90% of the tensile capacity of the bar. Upon rupturing, a plastic hinge in the concrete block was formed, accompanied by severe cracking to the concrete block. Once the restraining pressure of the duct was lost, the grout dilatated and splitting of the grout cylinder was observed.

4- The ductility of the connections slightly increased with increasing embedment length up to 8 d_b. Sudden increase in ductility was observed at 10 d_b and was approximately constant up to 16 d_b. At 16 d_b, a fully ductile failure was observed when the duct thickness was increased from 0.38 to 0.60 mm.

5- The hoop strains developed in the duct near the loaded end increased with the number of load cycles imparted on the specimen. The maximum recorded hoop strain was inversely proportional to the increase in embedment up to 10 d_b, after which, approximately no increase in hoop strain was observed.

6- The experimental results were used to calibrate the so-called frictional model, which describes the transfer of stress in the anchorage. The model considers the influential

parameters contributing to the bond of grouted connections. Its predictions were satisfactorily and in general agreement with the experimental results.

7- A design equation previously proposed by the authors to determine the minimum required development length under monotonic loading was compared to the experimental findings of this study. The predictions of this equation were valid under the loading conditions of the present study (given the applicable limitations thereof). Hence, this simple and refined equation could be used to estimate the development length of grouted connections, both under monotonic and cyclic loading similar to those experienced in this study. However, before implementation, a dedicated methodology exploring other influential effects such as the bar size, grout compressive strength and concrete compressive strength should be conducted.

5.7 REFERENCES

AC133-1209-R1, 2010. *Acceptence Criteria for Mechanical Connector Systems for Steel Reinforcing Bars*,

ACI Committee 318, 2014. Building Code Requirements for Structural Concrete and Commentary. *American Concrete Institute, Farmington Hills, MI, USA*, pp.1–519.

ACI Committee 408, 2003. Bond and Development of Straight Reinforcing Bars in Tension. *American Concrete Institute, Farmington Hills, MI, USA,*, pp.1–49.

ACI Committee 408.2R, 2012. Report on Bond of Steel Reinforcing Bars Under Cyclic Loads. *American Concrete Institute, Farmington Hills, MI, USA*, p.39.

Ameli, M.J. & Pantelides, C.P., 2017. Seismic Analysis of Precast Concrete Bridge Columns Connected with Grouted Splice Sleeve Connectors. *Journal of Structural Engineering*, 143(2), p.4016176. Available at: http://ascelibrary.org/doi/10.1061/%28ASCE%29ST.1943-541X.0001678.

ASTM 370, 2014. Standard Test Methods and Definitions for Mechanical Testing of Steel Products. *American Society for Testing and Materials*, 01.03, pp.1–50.

ASTM C39, 2016. Standard Test Method for Compressive Strength of Cylindrical Concrete Specimens. *American Society for Testing and Materials*, 04.02, pp.1–7.

ASTM C469/C469M-14, 2014. Standard Test Method for Static Modulus of Elasticity and Poisson's Ratio of Concrete in Compression. *American Society for Testing and Materials*, 04.02, pp.1–5.

ASTM C496/C496M, 2011. Standard Test Method for Splitting Tensile Strength of Cylindrical Concrete Specimens. *American Society for Testing and Materials*, 04.02, pp.1–5.

Balzas, G.L., 1986. Fatigue of Bond. *ACI Materials Journal*, 88(6), pp.620–629.

Bonacci, B.J.F., 1994. Bar yield penetration in monotonically loaded anchorages. *ASCE Journal of Strucutral Engineering*, 120(3), pp.965–986.

Cairns, J. & Jones, K., 1996. An evaluation of the bond-splitting action of ribbed bars. *ACI Materials Journal*, 93(1), pp.10–19.

Eligehausen, R., Popov, E.P. & Bertero, V. V., 1982a. Local bond stress-slip relationships of deformed bars under generalized excitations. In *Proceedings of the 7th European Conference on Earthquake Engineering.* Athens, Greeze, pp. 69–80.

Eligehausen, R., Popov, E.P. & Bertero, V. V., 1982b. Local bond stress-slip relationships of deformed bars under generalized excitations. *NSF Report No. UCB/EERC-82/23*, pp.69–80.

Elsayed, M. & Nehdi, M.., 2017. Experimental and Analytical Study on Grouted Duct Connections in Precast Concrete Construction. *Materials and Structures*, 50(198), pp.1–15.

Goto, Y., 1971. Cracks Formed in Concrete Around Deformed Tension Bars. *ACI Journal Proceedings*, 68(4), pp.244–251.

Haber, Z.B., 2013. Precast Column-Footing Connections for Accelerated Bridge Construction in Seismic Zones. *PhD Thesis, University of Nevada Reno*, (June), pp.1–661.

Kang, S.-M., Kim, O.-J. & Park, H.-G., 2013. Cyclic loading test for emulative precast concrete walls with partially reduced rebar section. *Engineering Structures*, 56, pp.1645–1657.

Lutz, L.A. & Gergely, P., 1967. Mechanics of Bond and Slip of Deformed Bars in Concrete. *ACI Journal Proceedings*, 64(11), pp.711–721.

Malvar, L.J., 1992. Bond of Reinforcement Under Controlled Confinement. *ACI Materials Journal*, 89(6), pp.593–601.

Orangun, C.O., Jirsa, J.O. & Breen, J.E., 1977. A Reevaluation of Test Data on Development Length and Splices. *Journal of the American Concrete Institute*, 74(3), pp.114–122.

Pang, J.B.K., Eberhard, M.O. & Stanton, J.F., 2010. Large-Bar Connection for Precast Bridge Bents in Seismic Regions. , (18), pp.231–239.

Parks, J.E., Papulak, T. & Pantelides, C.P., 2016. Acoustic emission monitoring of grouted splice sleeve connectors and reinforced precast concrete bridge assemblies. *Construction and Building Materials*, 122, pp.537–547.

Peng, Y.-Y., Qian, J.-R. & Wang, Y.-H., 2015. Cyclic performance of precast concrete shear walls with a mortar–sleeve connection for longitudinal steel bars. *Materials and Structures*, 49(6), pp.2455–2469. Available at: http://link.springer.com/10.1617/s11527-015-0660-0.

Raynor, D.J., Dawn, E.L. & Stanton, J.F., 2002. Bond-Slip Response of Reinforcing Bars Grouted in Ducts. *ACI Structural Journal*, 99(5), pp.568–576.

RILEM TC 65-MDB, 1986. Dynamic Behaviour of Concrete Structures. *Materials and Structures*, 17(101), pp.395–400.

Seifi, P., Henry, R.S. & Ingham, J., 2015. Preliminary test results of precast concrete panels with grouted connections. In *New Zealand Society for Earthquake Engineering Technical Conference*. Rotorua, New Zealand, pp. 744–751.

Shah, S.P. & Chung, L., 1986. Effect of Cyclic Loading Rate on Response of Model Beam-Column Joints and Anchorage Bond. In *Proceedings of the 3rd U.S National Conference on Earthquake Engineering*. pp. 1529–1540.

Stavridis, A. et al., 2013. Bond Strength and Cyclic Bond Deterioration of Large-Diameter Bars. *ACI Structural Journal*, 110(4), pp.659–670.

Steuck, K.P., Eberhard, M.O. & Stanton, J.F., 2009. Anchorage of large-diameter reinforcing bars in ducts. *ACI Structural Journal*, 106(106), pp.506–513.

Tastani, S.P. & Pantazopoulou, S.J., 2008. Behavior of Corroded Bar Anchorages. *ACI Structural Journal*, 104(6), pp.756–766.

Tastani, S.P. & Pantazopoulou, S.J., 2010. Direct Tension Pullout Bond Test: Experimental Results.

Journal of Structural Engineering, 136(6), pp.731–743.

Chapter 6

6 FINITE ELEMENT MODEL OF GROUTED CONNECTIONS USING INTERFACIAL COHESIVE ELEMENTS

6.1 INTRODUCTION AND BACKGROUND

Grouted reinforcing bar connections, or simply grouted connections, are ties having a wide variety of applications in the precast construction industry. When used in the context of precast load bearing walls, these connections are attractive owing to eliminating field welding and providing a straight force path extending along the height of a precast wall. The connection is comprised of a single large-diameter reinforcing bar grouted inside a corrugated metallic sleeve using a non-shrink high strength cementitious grout with a flowing consistency. Under current guidelines of the ACI 318-14, grouted connections are treated as a bar-in-concrete and designed after the development length in tension clauses disregarding the composite action of the sleeve. Previous experimental observations indicated deviation from this treatment, attributing this to the restraining effects of the corrugated duct. Although several recently published studies have provided experimental evidence for this disparity (Steuck et al. 2009; Elsayed & Nehdi 2017; Brenes et al. 2006; Tazarv & Saiidi 2015), limited information was found in the open literature addressing the numerical treatment of grouted connections. For instance, Raynor et al. (2002) modelled the connections using a simple one-dimensional model, where the mechanical bearing of the bar was simulated using a series of bond springs. The model depicted the experimental results with reasonable accuracy; however, it did not physically consider the sleeve, nor did it take into consideration the interaction between the connection and the surrounding concrete.

Modelling the bond-slip between a reinforcing bar and the surrounding concrete is of special importance in jointed regions, where the effects of slip and strain penetration can

be detrimental to the rotational capacity of the joint. A variety of methodologies with varying degree of complexity are currently available in the literature to model such bond-slip interactions. Some authors presented a fibre-section frame element model that takes into account slippage of the bar and subsequent bond degradations (Monti & Spacone 2000; Zhao & Sritharan 2007). Cho & Pincheira (2006) used rotational springs to model the rotation of column joints due to slippage of bars in column splices and used the model to calculate the required lap splice length to sufficiently develop the bars. Others presented detailed non-linear 3D continuum models that explicitly modelled the geometry of the deformations and its bearing on the concrete keys (Salem & Maekawa 2004; Gan 2000; Li 2010). The merit of such detailed models is that they can be used to conduct investigative studies on bond interactions between reinforcing bars and concrete, provided that adequate damage parameters are included in the model. However, considering their high computational cost, modelling complete reinforced concrete structures is deemed unpractical.

In most recent efforts to model bond-slip, researchers have resorted to interfacial elements that can be defined between the reinforcing bar and the concrete. These interfacial elements have constitutive relationships through which the characteristics of the bond-slip relationship of the assembly can be implemented. Input to such interface models would be the bond-slip relationship represented in interfacial elements through equivalent stress vs. displacement of the bar in the longitudinal direction.

Several researchers have proposed interfacial elements for use in a Finite Element (FE) platform. Cox & Herrmann (1998) were amongst the earliest studies which presented an element that utilizes an elastoplastic treatment for the bond stress-displacement relationship at the bar-concrete interface. This treatment modelled the effect of the normal stress on the bond stress via a yield function, while the shear dilatation caused by the bar ribs was accounted for using a non-associated flow rule. The validation of the model was carried out using a series of pull-out tests, which highlighted the accuracy and computational efficiency of the model (Cox & Herrmann 1999). A similar model was published by Lundgren & Magnusson (2001), who proposed 3D interfacial elements with a different elastoplastic treatment to model the bond-slip behaviour in FE simulations.

The interfacial elements presented by Lowes et al. (2004) and Murcia-Delso & Shing (2015) are different from those discussed above, in the sense that they utilize a phenomenological bond-slip law in their element formulations. Such phenomenological models were based on experimental observations, similar to that developed by Eligehausen et al. (1982), where a basic bond-slip relationship was modified by parameters that account for various effects, such as strain in bar, damage to the concrete and bar spacing. This methodology is generally more efficient than the plasticity formulation discussed above. Unlike plasticity models where iterations are required to calculate stresses at the interface, phenomenological models calculate interfacial bond stresses directly for a given slip increment. The model presented by Lowes et al. (2004) relied on data from neighbouring concrete elements to calculate damage parameters and update the bond stresses for a given bar slip. This interdependency complicates the implementation of this interfacial model in a FE platform. The formulation presented by Murcia-Delso & Shing (2015) solved this problem; however, their phenomenological model was based on experimental observations made on bars embedded in well-confined concrete, though tensile cracking in the concrete block was reported. In experimental investigation conducted by the present authors on grouted connections (Elsayed & Nehdi 2017), splitting failures were not observed inside the grout cylinder.

Accordingly, to allow accurate numerical depiction of the behaviour of grouted connections for modelling applications, the present paper discuses a new interfacial formulation to model grouted connections. The model simulates the behaviour of reinforcing bars bound by grouted metallic ducts using a phenomenological bond-slip derived from a carefully conducted set of experiments, which eliminates superficial compression associated with bond testing. The interface model was implemented using cohesive element formulation in the FE analysis program LS-DYNA (DYNA) and validated using experimental data from three different studies. Discussion of the constitutive laws and validation examples are presented in the following sections.

6.2   EXPERIMENTAL PROCEDURE AND RESULTS

The test specimens used to derive the local bond stress vs slip law are depicted in **Figure 6.1.** The specimens were carefully designed to mimic full-scale field conditions pertaining

to precast concrete wall construction and to eliminate artificial compressive fields that could influence the bond. Test specimens were comprised of a reinforced concrete block that had dimensions of 254 x 254 x 406.4 mm (254 mm is a typical width in full-scale precast shear walls). A 76.2 mm corrugated duct was placed concentrically in the middle of the specimen. To assist in the application of the load, four 16-mm threaded rods (ASTM A1035) were used to reinforce the block longitudinally. Transverse reinforcement was in the form of 10 mm closed-branch stirrups spaced 203.4 mm apart. The dowel bar used in this study was No. 8. The bars were de-bonded by wrapping it in 2-mm thick polystyrene wrap. The bonded length was 4 and 6 d_b. After concentric placement of the de-bonded bars inside the duct, non-shrink high-strength grout was mixed at low speed for 10 min and at high speeds for 5 min. Water (about 3.75 L) was added until a flowing consistency was achieved. Grouting was then done in the vertical position, as per full-scale field grouting applications. Subsequently, the specimens were cured for 28-d at temperature of 22 °C and relative humidity of 60%.
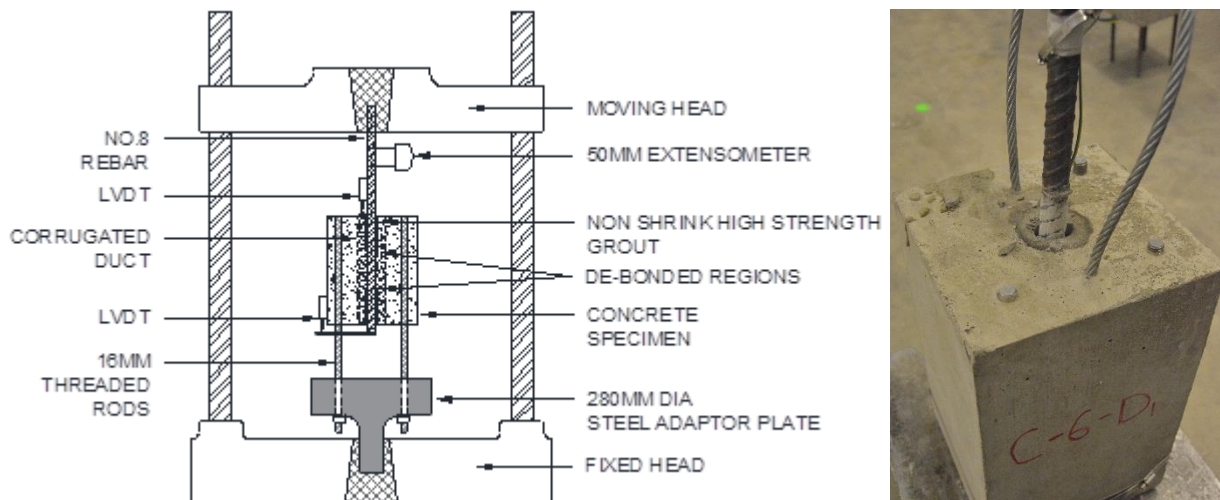
Figure 6.1: [Left to Right] Experimental setup; Failed bars by shearing of the grout keys at 6 d_b embedment.

The test results and analytical bond-slip law presented by Eligehausen et al. (1982) are portrayed in **Figure 6.2.** The local bond stresses were determined based on the classical equilibrium expression, as given in **Eq. 6.1**:

$$\tau = \frac{A}{\pi d_b} \cdot \frac{d\sigma_s}{d_x} \tag{6.1}$$

Where τ = bond stress; A = cross-sectional area of the bar, d_b = diameter of bar, σ_s = stress in bar.

The procedure for obtaining the bond stress was as follows: first, the strain distribution along the bonded length was determined knowing the strain value at the beginning (extensometer reading); amid the bonded length (strain gauge); and at the end (zero strain). Second, using information of the mechanical properties obtained from the coupons, the corresponding stress levels were determined. Third, the stress values were linearly connected assuming a linear stress distribution, which is justified given the elasticity of bar and shortness of the bonded length (Tastani & Pantazopoulou 2010; Eligehausen et al. 1982). By assuming a linear distribution of stress, the bond stresses were constant between two successive strain readings, and were calculated using the expression given in **Eq. 6.2**:

$$\tau = \frac{d_b}{2} \cdot \frac{\sigma_s}{L_d} \tag{6.2}$$

The experimental results were used to calibrate a local bond stress vs slip envelope to be used in the model development. A discussion of the constitutive relationship used in the interface model is presented in subsequent sections.
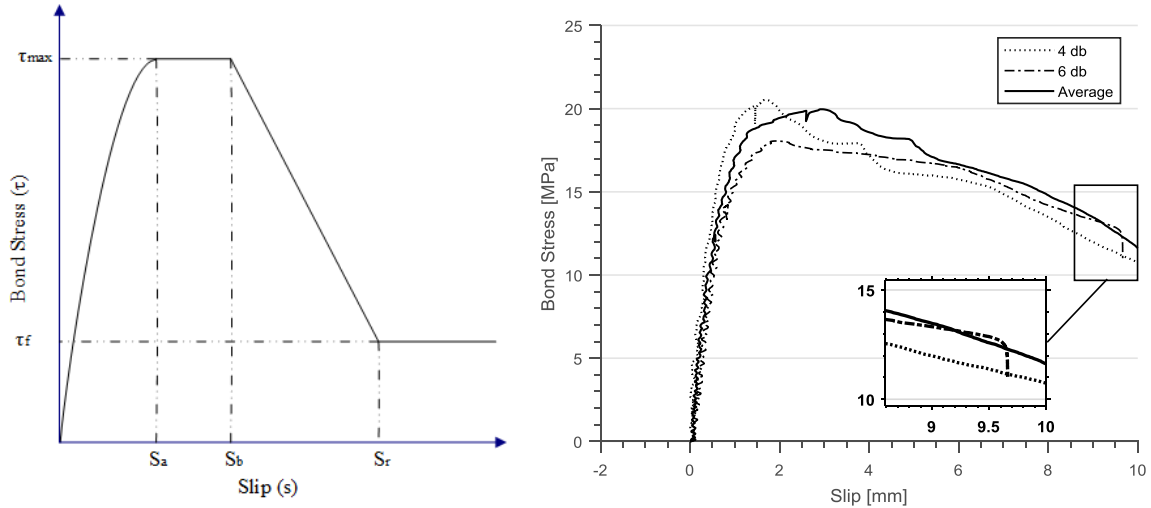
Figure 6.2: [Left] BPE bond-slip law recreated after Eligehausen et al. (1982); [Right] Experimental results.

6.3   INTERFACE MODEL

The development of the constitutive bond-slip law of interfacial elements at the bar-grout interface is described in detail below and illustrated in **Figure 6.3,** which also depicts stresses and relative displacements. The nodes of cohesive elements were tied to the nodes of their respective neighbouring elements using a tie constraint to ensure compatible displacements between respective elements. Relative displacements are comprised of three components: normal component, s_1, acting perpendicular to the longitudinal axis of the bar; a tangential component, s_2, acting along the axis of the bar; and a tangential component, s_3, acting along the transverse direction. Similarly, stresses along the interface are also defined via three components: a normal stress σ_1, and two tangential components τ_1 and τ_2 corresponding to their respective displacements.

.
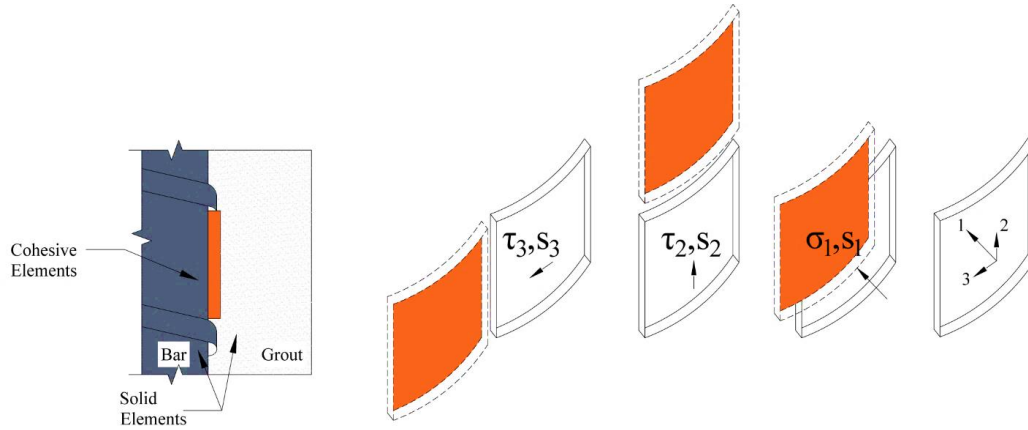
Figure 6.3: [Left] Bond modelling using interfacial elements; [Right] Interface coordinates, stresses, and relative displacements.

6.3.1   Bond-Slip Law

The bond-slip law adopted in this paper was based on the experimental results shown in **Figure 6.2**. The law was derived based on the Bertero, Popov and Eligehausen (BPE) model presented by Eligehausen et al. (1982), one of the most widely reported bond-slip models in the open literature. This model is mathematically expressed piecewise as follows:

$$\tau_2(s_2) = \begin{cases} \tau_{max}\left(\dfrac{s_2}{s_a}\right)^\alpha & s < s_a \\[2mm] \tau_{max} & s_a \leq s < s_b \\[2mm] \tau_{max} - \left(\dfrac{s_b - s_2}{s_b - s_r}\right)\left(\tau_{max} - \tau_f\right) & s_b \leq s < s_r \\[2mm] \tau_f & s_2 \geq s_r \end{cases} \tag{6.3}$$

where τ_{max} = maximum bond stress; α = curve fitting parameter reflecting the degree of confinement, s_a, s_b = are bar slips corresponding to the onset and outset of maximum plateau, respectively, to the beginning and end of the bond strength plateau; s_r = is the rib spacing; and τ_f = residual bond stresses.

Eq. 6.3 presents the basic bond-slip law, whose variables depend on four main parameters that need calibration based on experimental results, namely: τ_{max}; s_a; s_r, and τ_f. τ_{max} was found to be in the range of 18-20 MPa. The curve fitting parameter α was found to be in the range of 0.21-0.28. s_a fell in the 1.4-1.55 mm range. s_b was approximately equal to 1.2 s_a (1.86 mm). s_r was 9.75 mm. τ_f was found to be in the range of 12-13 MPa,

approximately 50-60% of τ_{max}. The values of τ_{max} and s_a (s_{max}) should be determined experimentally for each case and no accurate theoretical model could be used to predict their values. In the absence of experimental data, **Eq. 6.4** and **Eq. 6.5** can be used:

$$\tau_{max} \sim f_c'^{\,0.75} \tag{6.4}$$

$$s_{max} \sim 0.06 \, d_b \tag{6.5}$$

To account for the damage of the anchorage due to influencing factors, the effective bond stress is calculated as shown in **Eq. 6.6**:

$$\tau_2^* = m_n(s_1) \cdot m_s(\varepsilon_s) \cdot \tau_2 \tag{6.6}$$

where τ_2^* = effective bond stress; m_n = modifier to account for concrete splitting (function of s_1); m_s = modifier to account for post yielding behaviour.

m_n reflects the severity of splitting stresses in the concrete cover, which is a result of the radial compressive stresses induced unto the cover due to bar slip. This generates hoop tension, which forces the concrete to dilatate in the absence of transverse reinforcement. Consequently, regions where splitting occurs suffer from bond reduction. These failures were not observed when grouted connections were tested experimentally, irrespective of the intensity of the bond stresses developed. As such, m_n was taken equal to 1 since the corrugated duct provided a continuous compressive field restraining the grout. m_s accounts for the reduction in bearing area resulting from inelastic strains, as shown in **Figure 6.4(a)**.
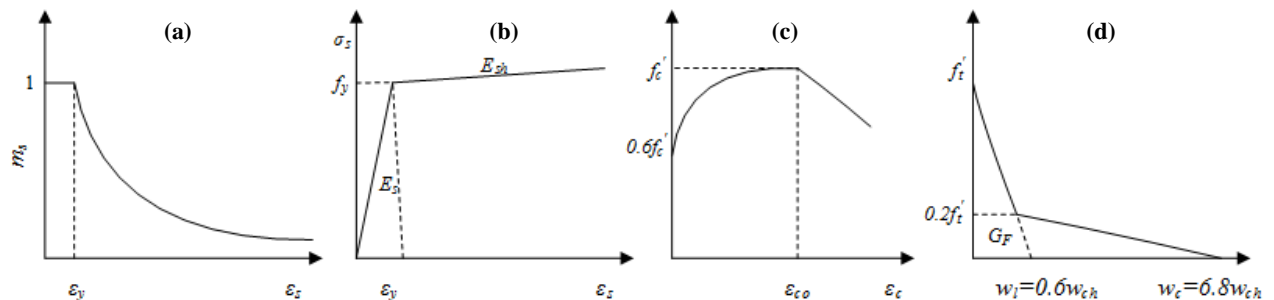
Figure 6.4: (a) modifier m_s as a function of the bar strain; (b) steel stress-strain constitutive relationship; (c) compressive hardening and softening laws; (d) tensile softening law.

Shima et al. (1987) observed bond reductions of as much as 25% at the onset of yielding, with further reductions as inelastic strains continued to accumulate. This modifier is only active when the elastic strain limit is exceeded. The value of m_s depends on whether bars have yielded when the experimental bond-slip relationship is obtained. If **Eq. 6.3** was obtained from specimens exhibiting yielding, then the subsequent reduction in the bearing area is inherently accounted for by the slip domain. For all other cases, **Eq. 6.7** mathematically expresses m_s as a function of ε_s as follows:

$$m_s(\varepsilon_s) = \begin{cases} 1 & \varepsilon_s < \varepsilon_y \\ \dfrac{\varepsilon_u - \varepsilon_s}{\varepsilon_u - \varepsilon_y} \sqrt[3]{\dfrac{\varepsilon_y}{\varepsilon_s}} & \varepsilon_y \leq \varepsilon_s < \varepsilon_u \\ 0 & \varepsilon_s \geq \varepsilon_s \end{cases} \qquad (6.7)$$

where ε_s = strain in rebar; ε_y = yield strain of the rebar at the onset of strain hardening; ε_u = ultimate strain capacity of the rebar.

6.3.2   Normal Stress

The normal stress component σ_1 is dependent on the use of an appropriate value of θ, the angle of inclination. This is imperative for proper simulation of the wedging action at the interface since it represents the fraction of bond forces on the inclined face of the ribs. The value of θ strongly depends on various influential parameters, including the geometry of the lugs and the characteristics at the cement-aggregate interface. The exact value of θ is not known and remains a matter of great contention in the open literature.

This concept was originally proposed by Lutz & Gergely (1967) and experimentally verified by others. For example, Tepfers (1979) observed the formation of wedges with a face angle of 30-40 degrees in front of the lugs of reinforcement. Similar observations were reported by Cairns & Jones (1996) who assumed an inclination angle of 45°. Goto (1971) observed that the initiation of cracks at the bar-concrete interface occurs at an angle of approximately 60°. The importance of θ lies in the proper simulation of σ_1, which controls splitting failures of the assembly. It should be noted that splitting failures of grouted connections were not observed experimentally in the open literature (Provost-Smith et al.

2017; Elsayed & Nehdi 2017; Raynor et al. 2002; Matsumoto et al. 2008; Steuck et al. 2009). As such, σ_1 was suppressed using a penalty stiffness formulation as given by **Eq. 6.8** below:

$$\sigma_1 = k_1 \cdot s_1 \tag{6.8}$$

6.3.3   Tangential Stress

The development of tangential stresses τ_3 was suppressed by restricting the rotation of the bar (tangential slip s_3 in **Figure 6.3**). This was done via a penalty stiffness formulation, k_3, as per **Eq. 6.9**:

$$\tau_3 = k_3 \cdot s_3 \tag{6.9}$$

6.4   IMPLEMENTATION

The bond-slip law discussed above forms the basis of the constitutive relationship of cohesive elements used to model the interface between the reinforcement and the concrete, as shown in **Figure 6.5**. The interfacial cohesive element was implemented in a user defined subroutine in the commercial finite element package LS-DYNA. The analysis was run using the default explicit non-linear solver, which is based on a modified central difference time integration scheme. The grout, concrete, and steel reinforcement were modelled using fully integrated selectively reduced 8-noded brick elements utilizing element formulation the ELFORM_2. The bond elements were modelled applying solid hexahedron elements utilizing element formulation the ELFORM_19, which uses a traction-separation law. Encastre boundary conditions were imposed on the extremities of the modelled concrete block. The load was assigned to a predefined nodal group close to the tip of the bar to ensure uniform stress application unto the bar and avoid stress localization at specific nodes. The loading was applied using boundary prescribed motion until failure was observed. An overview of the material constitutive laws as well as a discussion of mesh sensitivity is presented below.
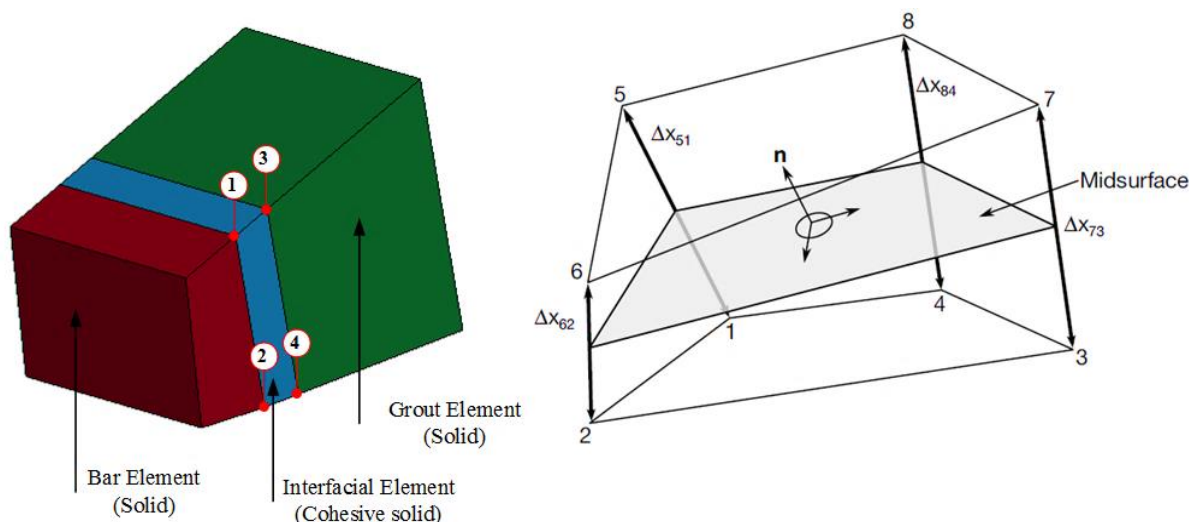
Figure 6.5: [Left] Cohesive elements at bar-grout interface; [Right] Tractions at mid-surface of cohesive solid elements (Livermore Software Technology Corporation 2016).

6.4.1 Materials Constitutive Laws

6.4.1.1 Steel Reinforcement

Steel reinforcement was modelled using a strain-independent elastoplastic model with kinematic hardening as shown in **Figure 6.4(b)**. The model employs simple failure criteria, based on the effective failure strain defined, which enables element erosion. The mechanical properties of the steel reinforcement were obtained experimentally as per ASTM 370 guidelines. The average measured yield stress and corresponding yield strain were 418 MPa and 0.20, respectively. The ultimate tensile stress and strain were 603 MPa and 16-18%, respectively.

6.4.1.2 Concrete and Grout

The concrete and grout constitutive compressive and tensile laws were defined using an elastoplastic material model developed by Grassl et al. (2013) as illustrated in **Figure 6.4(c) and (d).** This model combines constitutive laws for compressive and tensile behaviours with associated damage parameters. The plasticity rule employed was based on the Menetrey & Willam (1995) failure surface, whereas the fracture rule was based on the classical smeared crack approach. The compressive stress-strain relationship was described by three branches. A linear ascending branch from 0 to the critical stress f_{co}, whose values

are widely reported to be in the range of $0.6 - 0.8\ f_c{}'$ (Lubliner et al. 1989). The compressive hardening rule (**Figure 6.4(c)**) can be approximated after the Hognestad (Hognestad 1951) approach and the compressive stress is given by **Eq. 6.10**:

$$\sigma_c =\ f_c{}'\left(\frac{2\varepsilon}{\varepsilon_{co}} - \left(\frac{\varepsilon}{\varepsilon_{co}}\right)^2\right) \tag{6.10}$$

Where $f_c{}'$ = uniaxial unconfined compressive strength; ε_{co} = compressive strain at the onset of hardening expressed as $1.71\frac{f_c{}'}{E_c}$.

The exponential tensile softening law was idealized using a bi-linear function relating tensile stresses to the crack opening displacement width w_c, as shown in **Figure 6.4(d)**. The crack opening at the partial (w_l) and complete (w_c) release of stress is a function of w_{ch}, which is defined as the fracture energy of concrete G_F normalized by the tensile strength f_t. G_F should be obtained experimentally by means of notched beam tests. When such tests are not available, **Eq. 6.11** can be used after the statistical approach provided by Bažant & Becq-Giraudon (2002):

$$G_F =\ 2.5\ \alpha_0 \left(\frac{f_c{}'}{0.051}\right)^{0.46}\left(1 + \frac{d_a}{11.27}\right)^{0.22}\left(\frac{w}{c}\right)^{-0.30} \tag{6.11}$$

Where d_a = nominal maximum aggregate size; $\frac{w}{c}$ = water-to-cement ratio; α_0 = aggregate sensitive parameter dependent on the surface characteristics, taken as 1 for river aggregates and 1.11-1.44 for crushed aggregates.

6.4.1.3   Cohesive Elements

The cohesive elements used in the analysis are exhibited in **Figure 6.5**. The element follows the formulation proposed by Tvergaard & Hutchinson (1992). Traction stresses are calculated on the mid-surface of the element, which is defined as the mid-points between the nodal pairs 1-5, 2-6, 3-7, and 4-8. These tractions are functions of the differences of displacements between nodal pairs interpolated to the integration points. Tractions had three components, two of which are in the plane of the mid-surface (s_2 and s_3), and the

third represents the normal component (s_1). The model includes three general irreversible mixed-mode interaction formulations, reflecting fracture modes in the normal directions (mode I) and the tangential directions (mode II), as shown in

Figure 6.6. The interaction between fracture modes I and II is taken into consideration through a dimensionless separation parameter λ, which is given by **Eq. 6.12**:

$$\lambda = \sqrt{\left(\frac{s_2}{\delta_{II}^F}\right)^2 + \left(\frac{s_3}{\delta_{II}^F}\right)^2 + \left(\frac{s_1}{\delta_I^F}\right)^2} \tag{6.12}$$

Where δ_{II}^F and δ_I^F = are the maximum (failure) separation in the tangential and normal directions, respectively calculated per **Eq. 6.13** and **Eq. 6.14**, respectively**:**

$$\delta_I^F = \frac{G_I^c}{A^\circ \times T} \tag{6.13}$$

$$\delta_{II}^F = \frac{G_{II}^c}{A^\circ \times S} \tag{6.14}$$

Where G_I^c and G_{II}^c = are the fracture toughness in the tangential and normal directions, respectively; A° = the area under the normalized bond-slip curve; T and S = are the peak traction stresses in the normal and tangential directions, respectively. The fracture toughness G_{II}^c and the normalized area A° were calculated using **Eq. 6.15** and **6.16**, respectively:

$$G = \int_0^S \tau(s) \, ds \tag{6.15}$$

$$A^\circ = \int_0^\omega \tau(\omega) \, d\omega \tag{6.16}$$

Where ω = is the normalized separation parameter (for example $\frac{s_2}{\delta_{II}^F}$ for separation in direction 2).

It is important to highlight that, although the separation parameter λ is calculated based on the interaction between the three modes of failure, s_1 and s_3 were suppressed using a penalty

stiffness formulation as mentioned in Sections 6.3.1 and 6.3.2. This is based on experimental observations on grouted connections tested under monotonic loads (Elsayed & Nehdi 2017). The failure criterion is initiated when the dimensionless separation parameter λ reaches a critical value of 1. Upon failure, the tangential (τ_2 and τ_3) and normal (τ_1) components of the traction acting on the interface are calculated based on **Eq. 6.17**, expressed in matrix notation as follows:

$$\begin{bmatrix} \tau_1 \\ \tau_2 \\ \tau_3 \end{bmatrix} = \frac{\tau(\lambda)}{\lambda} \begin{bmatrix} \dfrac{\delta_I^F}{(\delta_{II}^F)^2} & 0 & 0 \\ 0 & \dfrac{\delta_I^F}{(\delta_{II}^F)^2} & 0 \\ 0 & 0 & \dfrac{1}{\delta_I^F} \end{bmatrix} \begin{bmatrix} s_1 \\ s_2 \\ s_3 \end{bmatrix} \tag{6.17}$$
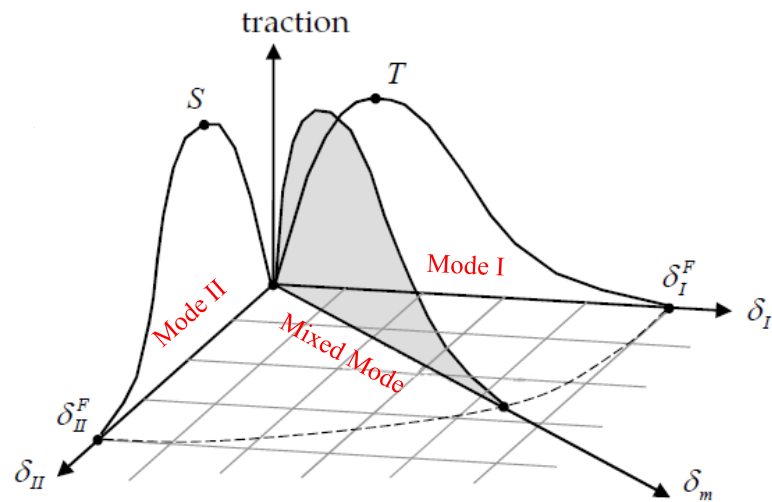
Figure 6.6: Mixed mode interactions (Livermore Software Technology Corporation 2016).

6.5   MODEL VALIDATION

The preceding sections described the constitutive laws of an interface model describing the bond behaviour of grouted connections. The accuracy of the model in depicting the behaviour of grouted connections was verified by comparing model calculations to experimental findings in the open literature. Due to the scant studies on grouted connections, model results could only be compared to the results of three relevant studies.

The purpose of the verification was not merely to appraise the accuracy of the model under various elastic and plastic bar conditions. As mentioned earlier, one of the features of the proposed model is that it requires a simple calibration process by changing three attributes of the supposed bond-slip law (**Figure 6.2**), namely: τ_{max}; s_{max}; and s_r. The properties of the concrete and steel along with the input parameters used in the analyses are reported in **Table 6.1**.

Table 6.1: Material parameters for concrete, steel and grout; and bond-slip model calibration parameters; model validation.

Study	L_d (d_b)	Material Parameters							Model Calibration Parameters			Model Validation			
		Steel			Concrete		Grout		$^{(1)}\tau_{max}$ (MPa)	s_{max} (mm)	s_r (mm)	Relative Error (%)	V	RMSE	MAPE (%)
		d_b (mm)	f_y (MPa)	f_u (MPa)	f_c' (MPa)	f_t (MPa)	f_c' (MPa)	f_t (MPa)							
Elsayed and Nehdi (2017)	6.0											18.36	0.82	26.02	13.93
	8.0	25.4	418.8	601.2	61.6	6.1	39.3	6.3	20.7	1.6	9.8	22.13	0.78	44.92	17.80
	12.0											-	-	-	-
Zhou et al.(2017)	3.9	25.4	400.0	635.0	44.8	4.0	34.5	3.5	14.7	4.2	12.0	19.47	0.81	12.18	8.79
	7.8											20.68	0.79	41.98	10.12
Steuck et al.(2009)	8.0	32.2	421.2	700.0	42.8	3.9	57.0	4.5	18.1	3.8	17.5	23.23	0.77	49.83	13.47

Calculated as $0.6\sqrt{f_c'}$ (Coronado & Lopez 2006)

Note: RMSE refers to the Root Mean Square Error; and MAPE refers to Mean Absolute Percentage Error

$^{(1)}$ *Calculated as the average bond stresses at 4 and 6 d_b*

6.5.1   Validation Metric

The validation metric described by Oberkampf & Trucano (2002) was used as a basis for validation in the present study to provide a quantitative estimate of the relative error between the numerical and experimental results. This validation metric, V, is given by **Eq. 6.18** as follows:

$$V = 1 - \frac{1}{s_{end} - s_0} \int_{s_0}^{s_{end}} \left| tanh \frac{N(s) - E(s)}{E(s)} \right| ds \qquad (6.18)$$

 Where s_0 and s_{end} are the initial and final slip, respectively; $E(s)$ and $N(s)$ are the experimental and numerical domains, respectively. Some key features of **Eq. 6.18** can be identified. First, it normalizes the difference between the numerical and experimental results, thus allowing the relative error to be computed. Second, the error is calculated over individual points on the slip domain measuring the relative error at every point in the distribution. Third, when the difference between the domains is zero, the validation metric is equal to unity, which presents a match between the experimental and numerical results. Finally, as the summation of the relative error becomes large, the validation metric converges to zero. The values of the calculated validation metrics are given in **Table 6.1**. Additionally, the Root Mean Square Error (RMSE) and Mean Absolute Percentage Error (MAPE) were calculated for the distribution, values of which are reported in **Table 6.1**. The RMSE and the MAPE were calculated to provide a comparison between the error estimation of the metric discussed in **Eq. 6.18** and more conventional error measures reported in the literature. As observed from the error values reported in **Table 6.1**, the validation metric tends to provide an overstated impression of the relative error.

6.5.2   Validation Examples

6.5.2.1   Elsayed and Nehdi (2017)

Finite element models of three monotonic pull-out tests conducted by Elsayed & Nehdi (2017) were analysed. The specimens consisted of concrete rectangular prisms having a cross-section of 208 x 208 x 406.4 mm, where the grouted ducts were placed concentrically.

The specimens were constructed using No. 8 bars with a measured yield stress and strain of 418 MPa and 0.2%, respectively. The average 28-day compressive strength of the concrete and grout were 50.6 and 40 MPa, respectively. The three specimens had embedded lengths of 6, 8 and 12 d_b. The specimens were carefully selected to highlight several key features. First, an embedded length of 6 d_b was chosen for a direct comparison of the bond-slip model since it represents a close rendering of the local envelope of the anchorage. At such embedment length, the difference between the observed slip at the loaded and free ends is nominal, hence the common assumption of uniform bond stress used in bond studies. Second, an embedded length of 8 d_b, represents a departure from the uniform slip assumption as moderate non-linearity is perceived. Third, an embedded length of 12 d_b represents a highly non-linear distribution as the effective bond stresses peak closer to the loaded end and attenuate towards the un-loaded end. This non-linearity introduces redundant lengths along the bar, whose ribs engage as the bond towards the loaded end experiences plastification. The choice of the embedment lengths analysed was also based on the different failure modes experienced by the specimens.

The model components, meshes, boundary conditions and loading are shown in **Figure 6.7(a)**. The force vs free end slip results of the different analyses are displayed in **Figure 6.8**. The purpose of this analysis was to appraise convergence to the experimental solution, as well as highlight the computational efficiency of the model. The convergence criteria were both quantitative and qualitative based on evaluation of the predicted response and the relative error calculated from **Eq. 18** (max 25%). Four mesh sizes were considered, namely 6.5x7; 6x4; 3x2; and 1x2 mm, results of which are displayed in **Figure 6.8** for 6 d_b embedment length. It can be observed that the convergence rate dramatically increased when the mesh size was decreased from 6.5x7 mm to 6x4 mm. The rate of convergence had a slight increase as the mesh size was reduced until a mesh size of 3x2 mm, below which no significant improvements were observed. Good agreement between the curves was observed when the mesh size was 3x2 mm. The computational effort shown in Figure 8(a), was calculated as the time required to complete the analysis on a standard single core processor of a desktop computer. For instance, the computational time increased by 54% when the mesh was refined from 6.5x7 (V ~ 0.23) to 6x4 (V ~ 0.68) mm. A slight increase in computational time by 15.4% was observed when the mesh size was refined from 6x4 to

3x2 (V ~ 0.82) mm, but was justifiable given the significant improvements in the load versus slip response, as observed from **Figure 6.8(a)**. The time required to complete the analysis for the 1x2 mm mesh size increased by 5 orders of magnitude than its 6.5x7 counterpart. Overall, the model exhibited computational efficiency even when the mesh size decreased.

It is noteworthy that due to the presence of some induced compression at the boundary of the specimens, the ascending branch was characterised by a stiffer response. This was further verified by comparison of the confinement parameter α, which was in the range of 0.16-0.19. The bond-slip law presented in **Eq. 6.3**, was based on an α value of 0.21-0.28. As anticipated, the analysis at 6 d_b yielded a close rendering of the bar pull-out behaviour. At 8 d_b, the FE results showed similar overall trend to the experimental results, characterized by an ascending plateau and descending branches of the envelope. The transition between the ascending branch and plateau observed in the experimental results exhibits a smoother higher order curve, apparently a result of the actual nonlinearity in the distribution of slip. It is believed that the continuous confining field provided by the corrugated duct helped magnify this behaviour. This observation is further supported by the plastification of bond elements towards the loaded end as the loading continues as depicted in **Figure 6.7(b)**. These modes cannot be predicted by the bond-slip model because of the lower order function assigned to the ascending branch (**Eq. 6.3**), hence the disparity between the numerical and experimental envelopes. The analysis at 12 d_b resulted in a bar fracture, which was also observed in experimental results, at a nearly identical load level corresponding to the tensile capacity of the bar (~600 MPa). The numerical model could simulate the failure observed in the grout cylinder manifested by the exhaustion and deletion of the cohesive bond elements, as shown in **Figure 6.7(c)**. The relative error and validation metric described above were calculated and reported in **Table 6.1**. It can be observed that the model results were in good agreement with the experimental observations from the study.
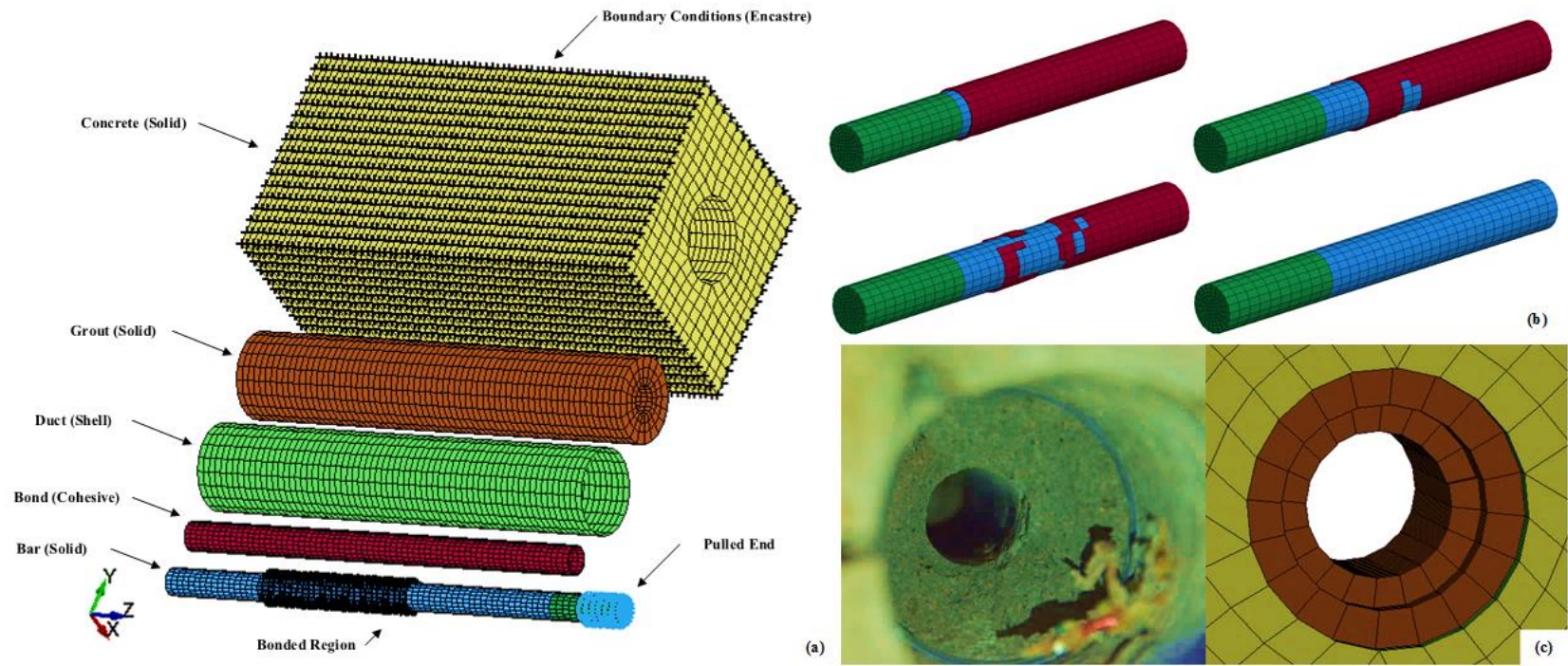
Figure 6.7: FE model parts, elements and boundary conditions Elsayed & Nehdi (2017); (b) bond plastification progression; and (c) interfacial element deletion to simulate shearing of the grout keys.
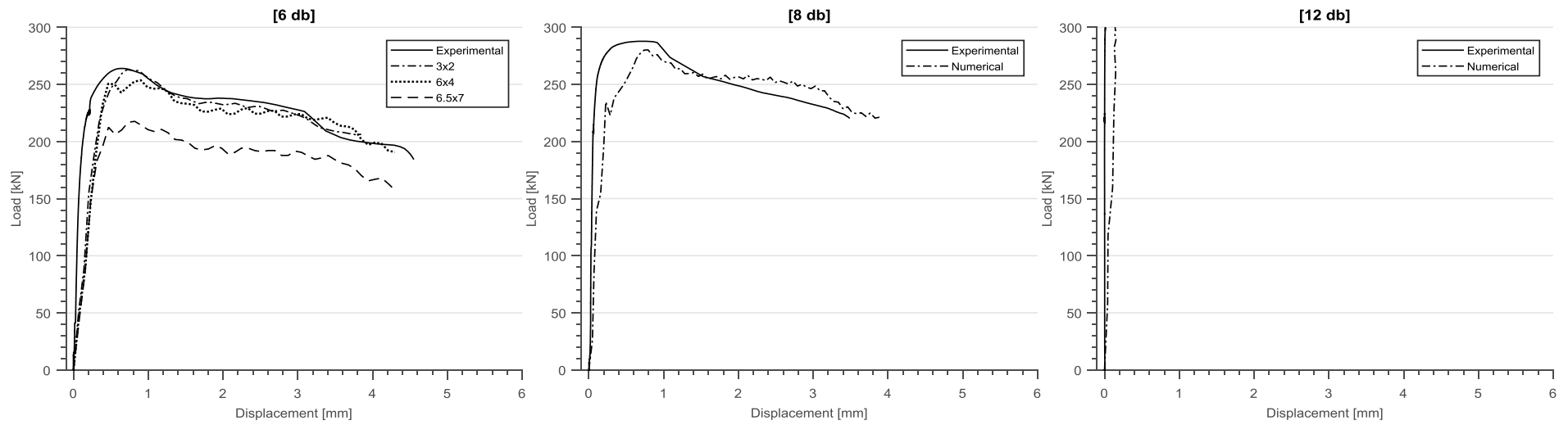
Figure 6.8: [Left to Right] FE analysis of bond slip tests by Elsayed & Nehdi (2017): load vs free end slip response at 6, 8 and 12 d_b, respectively.

6.5.2.2   Zhou *et al.* (2017)

The bond-slip model was implemented in a FE analysis to model the specimens presented in Zhou et al. (2017). In their study, a series of monotonic pull-out tests were performed on grouted connections to explore the bond-slip response and anchorage of stainless energy dissipating bars in segmental bridge columns. The specimen was in the form of a concrete beam with embedded corrugated ducts. The concrete beams were 810 x 240 x 900 mm (*L.W.H*). The tests were performed on imperial No. 8 (25.4 mm) and No. 11 (36 mm) bars. The average 28-d compressive strength of the concrete and grout was 44 and 57.2 MPa, respectively.
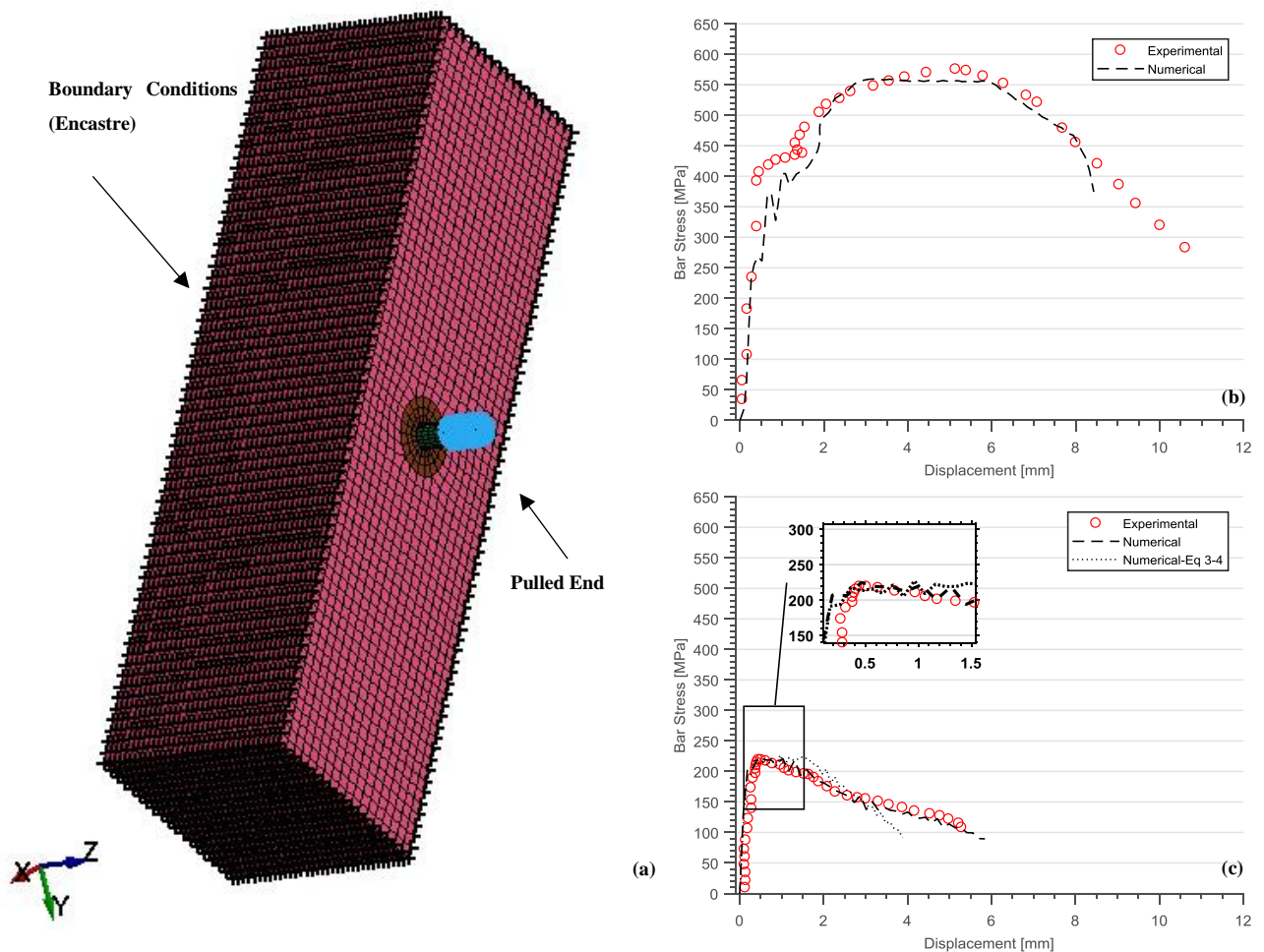
Figure 6.9: FE analysis of anchorage tests by Zhou et al. (2017): (a) model showing boundary conditions and pulled end; (b and c) bar stress vs loaded end displacements at 3.94 and 7.87 d_b, respectively.

The FE model of the tests is shown in **Figure 6.9(a)**. The results of the analyses for two No. 8 bars embedded at 7.87 and 3.94 d_b are illustrated in **Figure 6.9(b)** and **(c)**, respectively. The selected specimens were chosen so that they allow the verification of the model predictions under elastic and plastic bar conditions. **Figure 6.9(b)** shows the specimens with an embedment length of 7.87 d_b, where the bars have yielded at a stress corresponding to ~400 MPa. The yielding of the bars was accompanied by additional slip, which is evident from the sudden dropping of the load curve at ~400 MPa. The overall trend of the numerical curve at 400 MPa shows post-yield increase in slip. The small differences between the experimental and numerical envelopes observed in the post-yield region is attributed to the absence of a yield plateau in the assumed steel model. Overall, the model predictions are in good agreement with the experimental results in the ascending, plateau, and descending branches of the curve (based on the assumed model). **Figure 6.9(c)** shows the bar stress vs displacements at the loaded end when the bars were embedded at 3.94 d_b. Acceptable correlation was observed between the model predictions and corresponding experimental results as reflected by the error calculated (19 - 20%) in **Table 6.1**. Considering the relative error as calculated from **Eq. 6.18**., it should be noted that the specific results were extracted by digitization of experimental curves. Since most of the results were super-imposed on single figures, the accuracy of the digitization was decreased. Also, the MAPE was in the range of 8-10%, which reflects good agreement with experimental results, further highlighting the stringency of the used validation metric. Additional analysis was conducted using a hypothetical bond-slip law based on **Eq. 6.4-Eq. 6.5.** The model captured the trend of the experimental curve in terms of initial stiffness and plateau regions. Some discrepancies were observed in the descending branch. This is due to the assumption of residual bond stress of 50% of τ_{max}. While this is a crude approximation of a rather complex phenomenon, the results are deemed sufficiently acceptable if no experimental results can be utilized to calibrate the model.

6.5.2.3 Steuck *et al.* (2009)

The model components of FE analysis of the pull-out test of Steuck et al. (2009) is shown in **Figure 6.10(a)**. The experimental results presented in this study were acquired primarily on large diameter reinforcing bars embedded in grouted connections. The bar used in the

test was No. 10 (32.3 mm). The specimen was comprised of a 915-mm concrete specimen in-which a central corrugated duct was placed. The average 28-d compressive strength of the concrete and grout was 42.8 and 57 MPa, respectively. The bar stress vs loaded end slip is shown in **Figure 6.10**. The model reproduces well the ascending branch of the experimental results until the bar stress approaches 525 MPa. As stated earlier, the model cannot accurately depict the transition between the ascending and plateau branches, although close agreement was observed when the maximum bar stresses between both envelopes were compared (585 MPa). It is interesting to highlight that the artefacts of yielding were not experimentally observed in this study. This was also not observed in Elsayed & Nehdi (2017). The effects of bar yielding on reducing the local bond stresses of an anchorage acts via two main mechanisms. First, at the onset of yielding, additional slip is invoked by the large strains and subsequent deformations of the bars. Second, the plastic strain accumulation brings about a reduction in the cross-sectional area of the bar, which disengages the ribs close to the loaded end. At approximately 0.2 mm/mm of strain, the ribs are completely disengaged. While the reasons for the absence of these observations from the experimental results are not obvious, it could be attributed to the intimate interfacial characteristics of grouted connections due to the flowing consistency of the grout. The relative error between the experimental and numerical results was 23%. As mentioned earlier, this metric tends to provide stringent error values (for instance compared to MAPE of 13.47). However, as can be observed from **Table 6.1**, good correlation exists highlighting the efficacy of the model in depicting the behaviour of grouted connections.
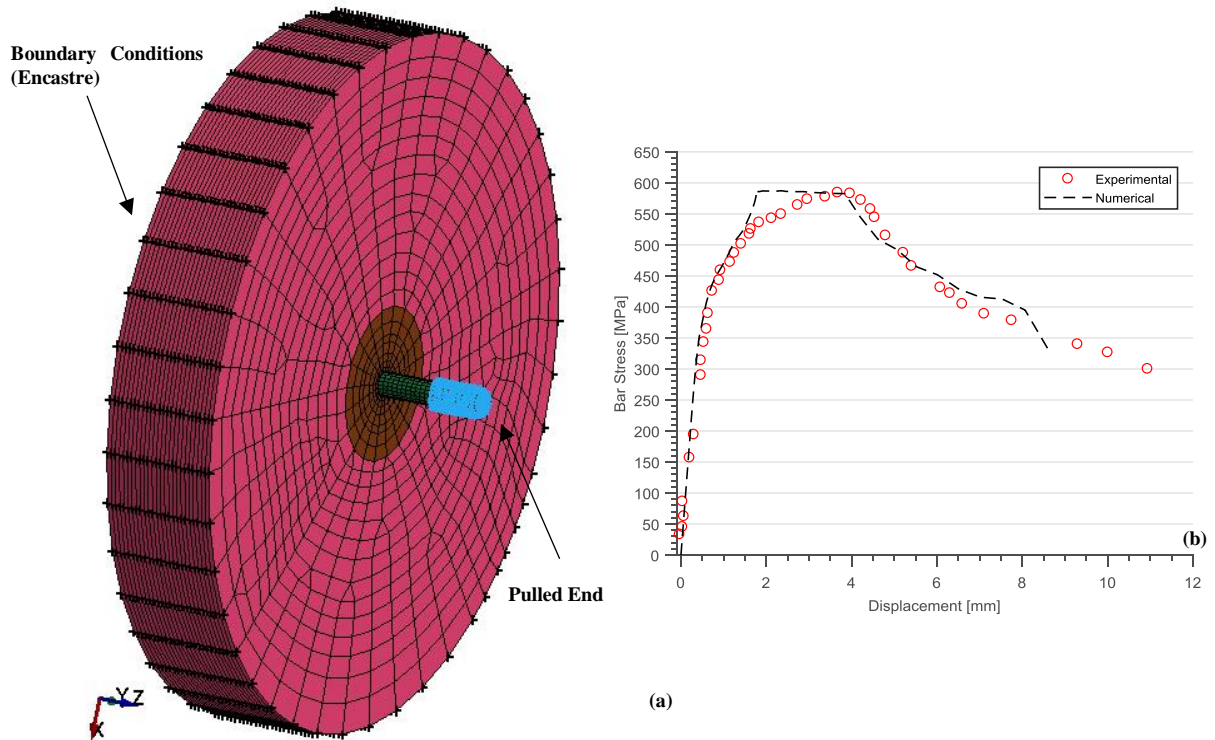
Figure 6.10: FE analysis of anchorage tests by Steuck et al. (2009): (a) model showing boundary conditions and pulled end; and (b) bar stress vs loaded end slip at 7.68 d_b .

6.6   FURTHER RESEARCH

The present study proposed an interfacial model of grouted connections under monotonic loads. However, an accurate relationship between monotonic and cyclic loading has yet to be established and requires further investigation. The extension of the presented bond slip model to include deterioration due to cyclic loads is yet to be implemented. Before the model can be used to model complete precast wall structures, full-scale experimental testing of grouted wall panels should be explored to provide a basis for calibration.

6.7   CONCLUSIONS

This paper discusses the development and calibration of an interfacial model suitable for use in FE platforms for capturing the behaviour of grouted connections used in precast concrete construction. The model utilizes a phenomenological bond-slip model to predict the bond slip behaviour of grouted anchorages. This was achieved by removing geometric non-linearities associated with modelling bar lugs and replacing it with interfacial cohesive

elements. This endowed the simulation with superior computational efficiency while yielding acceptable results. The proposed model is easy to calibrate and would allow numerical simulation of precast concrete wall assemblies.

To confirm the ability of the model to capture the bond-slip behaviour in finite element analyses, the model was validated using several experimental tests retrieved from the open literature, including bond-slip and bar anchorage tests with different embedment lengths. The comparison between the numerical and experimental results showed that the model is able to reproduce the bond-slip behaviour of bars embedded in grouted connections with reasonable accuracy and has the ability to effectively capture bond failures.

6.8   REFERENCES

Bažant, Z.P. & Becq-Giraudon, E., 2002. Statistical prediction of fracture parameters of concrete and implications for choice of testing standard. *Cement and Concrete Research*, 32(4), pp.529–556.

Brenes, F.J., Wood, S.L. & Kreger, M.E., 2006. Anchorage Requirements for Grouted Vertical-Duct Connectors in Precast Bent Cap Systems. In *Texas Department of Transportation Technical Report No. FHWA/TX-06-4176-1*. pp. 1–251.

Cairns, J. & Jones, K., 1996. An evaluation of the bond-splitting action of ribbed bars. *ACI Materials Journal*, 93(1), pp.10–19.

Cho, J.-Y. & Pincheira, J.A., 2006. Inelastic Analysis of Reinforced Concrete Columns with Short Lap Splices Subjected to Reversed Cyclic Loads. *ACI Structural Journal*, 103(2), pp.280–290.

Coronado, C.A. & Lopez, M.M., 2006. Sensitivity analysis of reinforced concrete beams strengthened with FRP laminates. *Cement and Concrete Composites*, 28(1), pp.102–114.

Cox, J. V. & Herrmann, L.R., 1998. Development of a plasticity bond model for steel reinforcement. *Mechanics of Cohesive-Frictional Materials*, 3(2), pp.155–180.

Cox, J. V. & Herrmann, L.R., 1999. Validation of a plasticity bond model for steel reinforcement. *Mechanics of Cohesive-frictional Materials*, 4(4), pp.361–389.

Eligehausen, R., Popov, E.P. & Bertero, V. V., 1982. Local bond stress-slip relationships of deformed bars under generalized excitations. *NSF Report No. UCB/EERC-82/23*, pp.69–80.

Elsayed, M. & Nehdi, M.., 2017. Experimental and Analytical Study on Grouted Duct Connections in Precast Concrete Construction. *Materials and Structures*, 50(198), pp.1–15.

Gan, Y., 2000. Bond stress and slip modeling in nonlinear finite element analysis of reinforced concrete structures. *M.Sc Thesis, University of Toronto*, pp.1–251.

Goto, Y., 1971. Cracks Formed in Concrete Around Deformed Tension Bars. *ACI Journal Proceedings*, 68(4), pp.244–251.

Grassl, P. et al., 2013. CDPM2: A damage-plasticity approach to modelling the failure of concrete. *International Journal of Solids and Structures*, 50, pp.3805–3816.

Hognestad, E., 1951. A Study of Combined Bending and Axial Load in Reinforced Concrete Members. *Bulletin Series No. 399*, p.128. Available at: http://hdl.handle.net/2142/4360.

Li, J., 2010. An investigation of behavior and modeling of bond for reinforced concrete. *PhD Thesis, University of Washington*, pp.1–304.

Livermore Software Technology Corporation, 2016. *LS-DYNA Keyword User's Manual Volume I*,

Lowes, L.N., Moehle, J.P. & Govindjee, S., 2004. Concrete-Steel Bond Model for Use in Finite Element Modeling of Reinforced Concrete Structures. *ACI Journal*, 101(S50), pp.501–511.

Lubliner, J. et al., 1989. A plastic-damage model for concrete. *International Journal of*

Solids and Structures, 25(3), pp.299–326.

Lundgren, K. & Magnusson, J., 2001. Three-Dimensional Modeling of Anchorage Zones in Reinforced Concrete. *Journal of Engineering Mechanics*, 127(7), pp.693–699.

Lutz, L.A. & Gergely, P., 1967. Mechanics of Bond and Slip of Deformed Bars in Concrete. *ACI Journal Proceedings*, 64(11), pp.711–721.

Matsumoto, E.E. et al., 2008. Development of a precast concrete system. *PCI Journal*, 53(3), pp.74–86.

Menetrey, P. & Willam, K.J., 1995. Triaxial Failure Criterion for Concrete and its Generalization. *ACI Structural Journal*, 92(3), pp.311–318.

Monti, G. & Spacone, E., 2000. Reinforced Concrete Fiber Beam Element with Bond-Slip. *Journal of Structural Engineering*, 126(6), pp.654–661.

Murcia-Delso, J. & Shing, P.B., 2015. Bond-Slip Model for Detailed Finite-Element Analysis of Reinforced Concrete Structures. *Journal of Structural Engineering*, 141(4), pp.1–10.

Oberkampf, W.L. & Trucano, T.G., 2002. Verification and validation in computational fluid dynamics. *Progress in Aerospace Sciences*, 38(3), pp.209–272.

Provost-Smith, D.J., Elsayed, M. & Nehdi, M.L., 2017. Effect of early-age subfreezing temperature on grouted dowel precast concrete wall connections. *Construction and Building Materials*, 140, pp.385–394.

Raynor, D.J., Dawn, E.L. & Stanton, J.F., 2002. Bond-Slip Response of Reinforcing Bars Grouted in Ducts. *ACI Structural Journal*, 99(5), pp.568–576.

Salem, H.M. & Maekawa, K., 2004. Pre- and Postyield Finite Element Method Simulation of Bond of Ribbed Reinforcing Bars. *Journal of Structural Engineering*, 130(4), pp.671–680.

Shima, H., Chou, L.-L. & Okamura, H., 1987. Bond Characteristics in Post-Yield Range

of Deformed Bars. *Proc. JSCE*, 6(387), pp.113–124.

Steuck, K.P., Eberhard, M.O. & Stanton, J.F., 2009. Anchorage of large-diameter reinforcing bars in ducts. *ACI Structural Journal*, 106(106), pp.506–513.

Tastani, S.P. & Pantazopoulou, S.J., 2010. Direct Tension Pullout Bond Test: Experimental Results. *Journal of Structural Engineering*, 136(6), pp.731–743.

Tazarv, M. & Saiidi, M.S., 2015. UHPC-filled duct connections for accelerated bridge construction of RC columns in high seismic zones. *Engineering Structures*, 99(6), pp.413–422. Available at: http://dx.doi.org/10.1080/15732479.2016.1188969.

Tepfers, R., 1979. Cracking of concrete cover along anchored deformed reinforcing bars. *Magazine of Concrete Research*, 31(106), pp.3–12.

Tvergaard, V. & Hutchinson, J.W., 1992. The Relation Between Crack Growth Resistance and Fracture Process Parameters In Elastic-Plastic Solids. *J. Mech. Phys. Solidr*, 40(6), pp.1377–1397.

Zhao, J. & Sritharan, S., 2007. Modelling of strain penetration effects in fibre-based analysis of reinforced concrete structures. *ACI Structural Journal*, 104(2), pp.133–141.

Zhou, Y., Ou, Y.-C. & Lee, G.C., 2017. Bond-slip responses of stainless reinforcing bars in grouted ducts. *Engineering Structures*, 141(June), pp.651–665.

Chapter 7

7 SUMMARY, CONCLUSIONS AND RECOMMENDATIONS

This chapter provides: i) A summary of the scope and major objectives of each chapter; and ii) Areas requiring future research.

7.1 SUMMARY AND CONCLUSIONS

This study was aimed at exploring the behaviour of emulative grouted connections used in precast wall construction under various changing parameters and loading procedures to determine the possible limit states of these connections.

Chapter 3 provided an exploratory study on the bond behaviour of grouted connections. Grouted connection specimens designed to mimic actual field conditions were tested under monotonically increasing tensile loads. Another objective of the study was to determine the adequacy of using FRP bars in connections intended for light architectural panels. The testing procedure utilized strategies to reduce the influence of the boundary conditions on the bond behaviour of the specimens. The main tested parameters were the embedment length, bar strain levels, bar geometry, and the corrugated duct. A total of 22 specimens were tested to failure. Results indicate that grouted connections behave quite differently from the bar-in-concrete model assumed in design codes, primarily due to the confinement mechanism of the duct, which provides restraint to lateral expansion of the grout. Varying the embedment length seemed to affect both the bond stress and slip, but did not influence the failure mechanism of the connections. The experimental results were used to calibrate two well-known bond-slip analytical treatments, whose predictions were in good agreement with experimental results. The experimental and analytical findings provide an enhanced understanding on the behaviour of such connections, highlighting the need for revisions in future relevant design code provisions.

In the study presented in **Chapter 4**, a series of experimental and analytical approaches have been adopted to investigate how grouted connections compare to bars embedded concrete. A total of 24 grouted connection specimens were compared to their bar-in-concrete counterparts. The main objective was to critically examine the underlying premises and efficacy of using the ACI 318-14 equation to design grouted connections and propose alternative empirical expressions more reflective of the unique nature of the connections. Results from the experimental and analytical procedures showed that grouted connections behaved markedly different from bars in concrete. Under similar conditions and regardless of the level of stress in the bar, the bond of grouted connections did not fail in splitting. The maximum bond strength recorded was consistently higher than that of the bar-in-concrete specimens, and the ascending branch of the envelope was stiffer. Based on the experimental findings, a design equation was developed using regression analysis of experimental results. The equation was able to predict the behaviour at 12 d_b with favourable accuracy.

Chapter 5 presented the findings of a novel experimental program which provided important information on the behaviour of grouted connections under cyclic loads. An extensive survey of literature has shown that the performance of this type of connection under cyclic excitation is yet to be explored. In the present study, 16 full-scale grouted connection specimens mimicking actual field conditions were tested to failure under quasi-static loading. Experimental findings revealed that, regardless of the strain level, grouted connections failed by grout shearing between the lugs of the bar. For all dowel embedment lengths, the load capacity of connections depended primarily on the connection seams of the duct, and not on the hoop strain level developed in it. The maximum recorded hoop strain measured on the duct was inversely proportional to the increase in embedment up to 10 d_b, after which, approximately no increase in hoop strain was observed. The experimental results were used to calibrate the frictional model, which describes the transfer of stress in the anchorage. The model considers the influential parameters contributing to the bond of grouted connections. Its predictions were satisfactorily and in general agreement with experimental results.

In **Chapter 6** of this dissertation, the development and calibration of an interfacial model suitable for use in finite element platforms, which can capture the behaviour of grouted connections used in precast concrete construction, were presented. The model adopts a phenomenological bond-slip law to predict the load versus slip response of the grouted bars and considers tensile yielding of the reinforcement. The local bond-slip law used was extracted from a set of experiments carefully designed to eliminate the spurious effects often associated with bond testing. By removing the geometric non-linearities associated with modelling bar lugs and replacing it with interfacial cohesive elements, the model allowed the simulation of grouted connections with superior computational efficiency, while yielding acceptable results. The model was validated using experimental results on grouted connections retrieved from the open literature. Good agreement between the experimental and numerical results was observed, highlighting the accuracy of the model in depicting interfacial stresses of the assembly. The model requires simple calibration and is computationally very efficient. It also accurately simulates the failure behavior of bars embedded in grouted connections.

It is believed that the substantial advancement in understanding the behaviour of grouted connections, both in terms of experimental procedures and numerical modelling, achieved in this dissertation, should open the door for the development of new design provisions in relevant design codes worldwide. Going beyond the current inaccurate bar-in-concrete oversimplification used for designing such connections to the more realistic experimental testing and numerical modelling of these widely used connections, should advance the agenda of the precast concrete industry in creating more resilient civil infrastructure.

7.2 RECOMMENDATIONS FOR FUTURE RESEARCH

The undertaking of the multi-phased experimental and numerical studies presented above, have revealed critical areas requiring future research:

1) This research was conducted under the assumption that the bond of grouted connections shares the same dependencies as bars in concrete ($\sqrt{f_c'}$). However, it was observed that the confinement effect provided by the corrugated duct and the failure mechanisms differed substantially from that of the bar-in-concrete

counterpart. A dedicated study to investigate this is yet to be undertaken by the authors. Results from this study would affect the way this type of bonded anchorages are perceived. It will also result in design equations more reflective of the nature of the connections.

2) There is a wealth of information on the behaviour of emulative precast walls in the literature. Most of these walls had connections designed according to the ACI 318-14 provisions. Based on the findings of this dissertation, much lower embedment lengths are required to mobilize ductile failures. A full-scale comparison between the ductility and performance of these types of walls is required to confirm the observations of this study.

3) As discussed in preceding sections, emulative connections are either achieved using grouted connections or by grouted sleeves. Mechanical coupling devices are expensive and have unfavourable tolerances. If the grouted duct can be reinforced in such a way that their walls are able to transmit tensile stresses, the duct will act as a mechanical coupler. Such a device should be tested, and the results be used to certify couplers against prequalifying requirements specified in ACI 318-14. The development of this type of duct could see field implementations owing to its competitive cost and superior performance.

4) The behaviour of grouted connections using specially engineered grouts is yet to be explored. During cold weather grouting, substantial heating costs are involved to ensure that temperature is above the freezing point and enable the hydration reactions of cement. Specially engineered materials like inorganic polymers, chemically bonded ceramics, and acid-alkali cements can provide an alternative to conventional binders, though more research is needed on their mixture optimization, and mechanical and durability aspects. The use of such materials could address industry specific needs, such as cold-weather grouting and applications where rapid setting of binders is usually sought.

5) The present study proposed an interfacial model of grouted connections under monotonic loads. The extension of the presented bond slip model to include deterioration due to cyclic loads is yet to be investigated.

Curriculum Vitae

NAME

M O H A M E D   G A M A L   E L S A Y E D

ACADEMIC QUALIFICATIONS

SEP. 2014 TO PRESENT	University of Western Ontario PhD in Civil Engineering	Canada
SEP. 2007 TO DEC. 2009	UAEU M.Sc. in Civil Engineering	UAE
SEP. 2000 TO JUN. 2005	AAST B.Sc. in Construction and Building Engineering	Egypt

PROFESSIONAL QUALIFICATIONS

- Professional Engineer: Association of Professional Engineers and Geoscientists of Alberta, APEGA (April. 2014): License number 122598.
- Professional Engineer (Structural): Michigan Department of Licensing, LARA (May 2017): License number 6201065841.
- Project Management Professional PMP; Project Management Institute PMI (2008). License number: 1281993.

PUBLICATIONS

Peer-Reviewed Journals:

1. **M. Elsayed**, M.L. Nehdi, and F. Ghrib, "Experimental and Analytical Study on Precast Concrete Dowel Connections under Quasi-Static Loading", In Press, *Construction and Building Materials*. Jan. 2018. **(Impact Factor: 3.7)**
2. **M. Elsayed**, M.L. Nehdi and D.J. Provost-Smith, "Experimental investigation of grouted bar-in-conduit connections under direct tensile load", under peer review, *Journal of Construction and Building Materials*, Jul 2017. **(Impact Factor: 3.7)**
3. **M. Elsayed** and M.L. Nehdi, "Experimental and analytical study on grouted duct connections in precast concrete construction", published, *Journal of Materials and Structures*. May 2017. **(Impact Factor: 2.6),** https://doi.org/10.1617/s11527-017-1056-0
4. D.J. Provost-Smith, **M. Elsayed**, and M.L. Nehdi, "Early-age exposure of grouted precast concrete wall connections to subfreezing curing temperatures", published, *Journal of Construction and Building Materials*, Vol. 140, pp. 385-394. Feb 2017. **(Impact Factor: 3.7)**
5. D.J. Provost-Smith, **M. Elsayed**, and M.L. Nehdi, "Investigation of grouted dowel connections for precast wall construction", under peer review, *ACI Structural Journal*, American Concrete Institute, Oct 2016. **(Impact Factor: 1.2)**

6. **El Sayed, M**; El Maaddawy, T. "Analytical model for prediction of load capacity of RC columns confined with CFRP under uniaxial and biaxial eccentric loading", *Materials and Structures*, Vol. 44, No. 1, pp. 299-311, <u>Jan. 2011</u>. **(Impact Factor: 2.6)**
7. El Maaddawy, T; **El Sayed, M**., Abdel-Magid Beckry "The effects of cross-sectional shape and loading condition on performance of reinforced concrete members confined with carbon fiber-reinforced polymers", *Materials and Design*, Vol. 31, No. 5, pp. 330-341, <u>May 2010</u>**. (Impact Factor: 4.4)**

Conference Proceedings:

1. **M. Elsayed**, D.J. Provost-Smith, and M.L. Nehdi "Bond Behavior of Grouted Connections under Monotonic Tensile Loads" Canadian Society of Civil Engineering Annual Conference, London, ON, Canada, 1-4 June 2016.
2. D.J. Provost-Smith, **M. Elsayed**, and M.L. Nehdi **"**Investigation of Grouted Precast Concrete Wall Connections at Sub-Freezing Condition" Canadian Society of Civil Engineering Annual Conference, London, ON, Canada, 1-4 June 2016.
3. J. Liu, S. Das, **M El Sayed**, G. Sturrgeon "Effect of Height-to-Thickness Ratio on Compressive Strength of Hollow Concrete Prisms", 12th Canadian Masonry Symposium, 2-5 June 2013, Vancouver, BC. Canada.
4. El Maaddawy, T., **El-Sayed, M.** "Load Capacity of Bi-axially Loaded Reinforced Concrete Columns Confined with FRP", 1st Middle East Conference on Smart Monitoring, Assessment and Rehabilitation of Civil Structures, 8-10 February 2011, Dubai, UAE.
5. El Maaddawy, T., **El-Sayed, M.**, Abdel-Magid B. "Effect of Section Shape and Load Eccentricity on Performance of RC Columns Wrapped with FRP", 13th International Conference on Structural Faults & Repair, 15-17 June 2010, Edinburgh, Scotland.

SCHOLARSHIPS AND AWARDS
- **Award**: Teaching Assistant of the year (2016)
- **Scholarship:** Queen Elizabeth Graduate Scholarship
- **Scholarship:** Natural Science and Engineering Council (NSERC): Awarded the prestigious Canada Graduate Scholarship (Awarded to approximately 200 of the top doctoral students in all disciplines of science and engineering across the nation)
- **Scholarship:** Ontario Graduate Scholarship